UNIVERSITY OF TRENTO
Department of Physics

THESIS SUBMITTED TO THE
DOCTORAL SCHOOL IN PHYSICS – XXXI CYCLE
BY

CARMELO MORDINI

FOR THE DEGREE OF
DOCTOR OF PHILOSOPHY – DOTTORE DI RICERCA

Measurement of the density profile of quantized vortices and of the equation of state in a 3D interacting Bose gas

SUPERVISOR: GABRIELE FERRARI

CO-SUPERVISOR: GIACOMO LAMPORESI

REFEREES: JAN ARLT AND GIACOMO ROATI

June 2019

Carmelo Mordini

Measurement of the density profile of quantized vortices and of the equation of state in a 3D interacting Bose gas

Ph.D. Thesis in Physics

University of Trento
June 2019

PhD Supervisor:
Gabriele Ferrari

PhD Co-supervisor:
Giacomo Lamporesi

Referees:
Jan Arlt
Giacomo Roati

To all the people who made me
have fun.

Contents

Introduction

The phenomenon of of Bose–Einstein condensation is one of the most studied topics in condensed matter physics. The theoretical and experimental effort of the scientific community has brought, over more than twenty years of research, to a deep understanding of the physics underlying condensed systems. However, a number of fundamental aspects of the topic are still under active research. During the course of my PhD I was involved in two projects of fundamental BEC physics: a study of the structure of quantized vortices, with direct comparison to theoretical predictions, and a measurement of the equation of state of a condensed Bose gas, highlighting the influence of particle interactions on the thermodynamics of the BEC transition. This thesis presents the work that I have done on each of these subjects.

Quantized vortices have been studied since the discovery of superfluidity in ^{4}He, and they are a typical characteristics of superfluid systems, contributing to their unique physical properties. The physics of quantum vortices depends strictly on the absence of viscosity in the fluid, for which particle interactions play a key role. There are numerous studies on the physics of isolated vortices, their interactions, and the mechanisms leading to their formation. Ultracold atomic BEC are a versatile experimental platform, thanks to the high degree of control over the parameters of the system which allowed for the development of a variety of techniques to create and observe quantized vortices. Despite all of this work, a direct and quantitative observation of the shape and density structure of quantized vortices in bulk superfluids was still missing, which was the aim of our work. Again, ultracold atoms are a good candidate for this research, thanks to the accurate predictions of the Gross–Pitaevskii theory.

The observation of vortices is made problematic by their small size, and by the difficulty of controlling the orientation of the nodal line for a precise determination of their shape. In our experiment a cigar-shaped geometry favors the formation of short and straight vortices, thanks to the tight radial confinement, and constrains their orientation on a plane. The size of the system is still big enough with respect to the width of the defect, so that the vortex behaves as isolated in a 3D bulk superfluid. The observation is made possible by time-of-flight techniques, since the vortex expands together with the condensate after releasing the system from its trapping potential. Comparing the observations with the expansion dynamics predicted by the Gross–Pitaevskii theory, we achieved a first quantitative measurement of the spatial structure of a quantized vortex.

Another key aspect of condensed systems, in which particle interactions play a major role, is in the thermodynamics of the BEC transition. Condensation does not require interactions, as it is driven only by the quantum statistics of particles, but their presence dramatically changes the thermodynamic properties of the gas. As the interaction energy grows with the particle density, their role is dominant at low temperatures in atomic gases in the BEC phase. The striking difference between an ideal and an interacting gas at zero temperature is immediately revealed in the shape that the sample assumes in a harmonic trap: a Thomas–Fermi profile is routinely observed in experiments, where an

ideal gas would have a much narrower Gaussian distribution.

What is less easy to observe is the way interactions affect the phase transition at finite temperature, which is revealed by the equation of state (EoS) of the system. The Hartree–Fock theory, which is the mean-field approach to the thermodynamics of interacting systems, predicts changes in the pressure and in the chemical potential of the gas that are in stark contrast with the textbook ideal model. In particular, the chemical potential is predicted to be non-zero in the BEC phase, and non-monotonic as a function of temperature with a peak at the transition point, due to the different exchange energy terms in the condensate and thermal fractions which coexist below the critical point.

What makes this feature interesting is that it has been theoretically predicted and observed in other, completely different kinds of superfluids. It has been measured in ^{4}He, where the EoS can be calculated starting from experimental measurements of the specific heat across the lambda transition. It has been directly observed in unitary Fermi gases, confirming the prediction of the universal thermodynamics of such systems with infinite interactions. This linked sequence of observations in superfluid systems of different nature brings to the conjecture that the presence of a peak in the chemical potential is a signature of the phase transition to a superfluid phase, independent of the physical nature of the superfluid. At the moment there is no theoretical proof for such a general statement. This makes it interesting to search for the presence of the peak in the EoS of a weakly interacting Bose gas, where it is predicted by the Hartree–Fock theory but still without any experimental observation. The measurement of this equation of state is precisely the goal of my research project.

Most of the experimental work on the thermodynamics of homogeneous systems results from observations in inhomogeneous samples, interpreted by means of the local density approximation. To apply this scheme, we need to measure the density distribution of a trapped atomic sample, which is difficult in a Bose gas because of the high density of the condensate. We solved this problem employing the partial-transfer absorption imaging technique (PTAI), which we used to image high-density regions of the BEC. Since the dynamic range of the density in a BEC is wider than the one accessible with a single image, I developed a high-dynamic-range reconstruction method to obtain a complete image of the trapped condensate from a sequence of PTAI shots, each one giving data in a different density range. With the combination of the two methods, we were able to measure the EoS of an interacting bosonic gas in a range of temperatures across the phase transition. The observations agree with the prediction of the Hartree–Fock theory, and confirm the presence of the superfluid peak in the chemical potential at $T = T_c$.

Thesis summary

The first chapter of this manuscript is a short, self-contained introduction to the theory of the subjects under study. I will first introduce the Gross–Pitaevskii equation (GPE), which describes dilute Bose–Einstein condensates of interacting particles at zero temperature. The properties of superfluid system are expressed in the GP theory by the connection between the wavefunction and the velocity field of the quantum fluid, which naturally leads to the presence of quantized vortices as particular solutions of the GPE. The resulting wavefunction describes the core structure of the vortex and its dependency on the shape and the density of the system, as well as its dynamics during a free expansion, and will be compared to the measurements detailed in Chap. 4. I will then turn to the finite-temperature case and review the thermodynamics of homogeneous and trapped condensed systems, deriving the equations expressing the pressure

and the chemical potential as functions of density and temperature. I will refer to this theory for the interpretation of the measurements that will be presented in Chap. 5. I will then introduce the local density approximation, and how it can be used to retrieve information on a homogeneous system from density measurements in a trapped sample. I will finally introduce the topic of universality in the thermodynamics of a system, and discuss the extent to which these two concepts apply to the case of an atomic Bose gas.

The second chapter is a technical description of the experimental setup in the Trento ultracold atoms laboratory, describing the tools that allow us to produce condensates of ^{23}Na atoms: the vacuum apparatus, the laser system, the electronics control, the high-power electrical setup needed to produce the magnetic trap. I will also describe the basic steps of our experimental routine to cool atoms down to condensation.

In the third chapter I will review the basis of absorption imaging, describing our imaging setup and the measurements for its calibration. These steps were crucial for the EoS project, as they are necessary for a precise determination of the absolute density distribution in the trapped sample.

The fourth chapter is dedicated to the vortex visibility project. I will describe the numerical solutions to the GPE leading to theoretical predictions for the shape of the vortex line and its time evolution during a free expansion. Then I will describe the measurements and the analysis procedure, which I developed and applied to both the simulation results and the experimental data, compare the two and discuss the results.

The final chapter describes my work on the EoS project. I will introduce the PTAI technique, describe our implementation and calibration, and the image reconstruction algorithm. Then I will present our results for the pressure and density profiles along the trap axis. I will discuss the method we used to extract the global thermodynamic parameters from such profiles. I will show the results for the EoS $p(n, T)$ and $\mu(n, T)$, where we observed the peak across the transition. Finally, I will discuss both the technical limitations in our experiment and the conditions for the validity of the LDA, which is at the basis of our result.

Chapter 1

Theoretical background

The concept of Bose–Einstein condensation (BEC) was first theorized in 1924 in a seminal work by S. N. Bose about the quantum statistics of indistinguishable particles applied to photons [1], and successively extended by A. Einstein to massive particles [2]. BEC predicts that in a gas of bosons, at sufficiently low energy, particles accumulate in the lowest-energy single-particle quantum state of the system with a macroscopic occupation. The transition can be described by the appearance of a complex *order parameter*, also called the condensate wavefunction, which represents the density distribution of condensed particles in the BEC phase and vanishes above the transition.

The discovery of superfluid ^{4}He [3, 4] brought the phenomenon to attention, as it developed the intuition that superfluidity could be a manifestation of BEC. The connection between condensation and superfluidity continued to be developed, with experiments on superfluid helium and superconducting metals playing a central role. Later on, the research on BEC was enriched by experiments on ultracold atomic gases, with the achievement of condensation of ^{87}Rb atoms in the group led by Cornell and Wieman [5] and of ^{23}Na in the Ketterle group [6] in 1995. This was made possible by the great development in experimental techniques of atomic physics for manipulating, trapping and cooling atoms [7–9]. Nowadays BEC can be observed routinely in laboratories, thanks to the scientific and technological effort that continued to the present day. Ultracold atomic gases represent a flexible experimental platform, where it is possible to study degenerate samples of many bosonic and fermionic species, manipulate them almost arbitrarily with the use of magnetic and optical fields, and study the fundamental and thermodynamic properties of these macroscopic quantum systems.

Being driven only by the quantum statistics of the constituting particles, BEC is the only known phase transition taking place also in the absence of interactions, making it

a cornerstone of quantum statistical mechanics. Particle interactions have however an important role in the physics of Bose gases, as they are necessary for the phenomenon of superfluidity and as they change the thermodynamics of the gas in a non-trivial way.

In this chapter, I will review some basic theory about interacting Bose–Einstein condensates, introducing superfluidity at zero temperature and showing how this leads to the presence of quantized vortices. I will describe the properties of these objects, that we observed in the measurements detailed in Chap. 4. Then I will review the thermodynamics of condensed systems and put the basis for the measurement of the equation of state that will be presented in Chap. 5.

1.1 BEC at zero temperature

1.1.1 The Gross–Pitaevskii equation

The physics of a condensate of interacting particles at zero temperature is captured by the Gross–Pitaevskii (GP) equation, independently derived by L. P. Pitaevskii [10] and E. P. Gross [11] in 1961 from a generalization of Bogoliubov's theory for weakly interacting bosons to inhomogeneous systems [12, 13]. To describe it, we start from the hamiltonian of a system of particles with mass m confined by a potential V_{ext}, written in second quantization as

$$H = \int d^3r\, \hat{\psi}^\dagger \left(-\frac{\hbar^2}{2m}\nabla^2 + V_{ext} \right) \hat{\psi} + \frac{g}{2}\hat{\psi}^\dagger\hat{\psi}^\dagger\hat{\psi}\hat{\psi}\,. \tag{1.1}$$

The quantum field operator $\hat{\psi}(r)$ describes the particle distribution in space, and the coupling constant g expresses the strength of two-body interactions. This simple form for the interaction term is valid only under the condition that the gas is *dilute*, that is when the mean interparticle distance is much greater than the range of the true two-body interaction potential. At low temperatures we can relate the coupling constant to the two-body s-wave scattering length a as $g = 4\pi\hbar^2 a/m$, and write the diluteness condition in terms of the gas parameter $na^3 \ll 1$, where n is the density of particles in the system.

At zero temperature, the macroscopic occupation of the condensed state makes the relative fluctuations in the number of particles in the condensate vanishingly small, hiding the quantum nature of the system. This allows us to replace the field operator with the classical function $\psi(r)$, the condensate wavefunction. Its squared modulus represents the particle density, $n = |\psi|^2$, while the gradient of the phase is related to the velocity field of the quantum fluid.

The total energy of the system is expressed by the energy functional

$$E = \int \left(\frac{\hbar^2}{2m}|\vec{\nabla}\psi|^2 + V_{ext}|\psi|^2 + \frac{g}{2}|\psi|^4 \right) d^3r\,, \tag{1.2}$$

which can be calculated as the average value of the hamiltonian in Eq. 1.1, once one identifies ψ with the quantum average $\langle\hat{\psi}\rangle$ and neglects all correlation terms in averaging the product of two or more field operators. This substitution marks the GP theory as a mean-field theory, where at the lowest order the (quantum, in this case) fluctuations in the order parameter are neglected. Using a stationary action principle, the equation of motion for the condensate wavefunction is derived as $i\hbar\partial_t\psi = \delta E/\delta\psi^*$, leading to the

GP equation

$$i\hbar\frac{\partial\psi}{\partial t} = \left[-\frac{\hbar^2}{2m}\nabla^2 + V_{ext}(r) + g|\psi|^2\right]\psi\,. \tag{1.3}$$

The GP theory provides extremely accurate predictions when compared to condensates of ultracold atomic gases [14]. In such systems the diluteness condition is completely fulfilled: considering alkali atoms for a simple estimate, the peak densities available in experimental samples are of order 10^{20} atoms/m^3 while the scattering length for contact interaction is typically of order 1 nm, making the gas parameter $na^3 \sim 10^{-7}$.

The ground state of the condensate can be found as the stationary solution of Eq. 1.3 with the lowest energy. Substituting $\psi(r,t) = \psi(r)e^{-i\mu t/\hbar}$ we obtain

$$\left[-\frac{\hbar^2}{2m}\nabla^2 + V_{ext}(r) + g|\psi|^2\right]\psi = \mu\psi \tag{1.4}$$

which is also called the *stationary* GP equation. The quantity μ is the chemical potential of the many-body system, and it is related to the total number of atoms N by the normalization of the wavefunction

$$\int |\psi|^2\, d^3r = N\,. \tag{1.5}$$

Even if cold atomic gases satisfy the dilute gas condition, the effects of atomic interactions are relevant and can actually dominate the physics of a trapped system. We will discuss the case of a harmonically trapped gas, where the external potential is given by

$$V_{ext} = \frac{1}{2}m\left(\omega_x^2x^2 + \omega_y^2y^2 + \omega_z^2z^2\right)\,, \tag{1.6}$$

where ω_j are the trap frequencies. This is the most natural choice to compare with experiments, as typical experimental samples are trapped in (magnetic or optical) potentials that, in the volume occupied by the atoms, are harmonic to a very good approximation. This form of the potential sets an energy scale of $\hbar\omega_{ho}$, where we define $\omega_{ho} = (\omega_x\omega_y\omega_z)^{1/3}$ as the harmonic oscillator trap frequency, and a length scale $a_{ho} = \sqrt{\hbar/m\omega_{ho}}$ called the harmonic oscillator length.

The strength of mean-field interactions in the BEC is governed by the parameter Na/a_{ho}, which in typical trapped gases can reach values of 10^3 when the number of atoms is sufficiently high (order of 10^6). In this conditions the kinetic energy term in Eq. 1.4, also called *quantum pressure* after the hydrodynamical formulation of the GPE, can be neglected, giving the analytic solution for the BEC ground state density

$$n_{TF}(r) = |\psi(r)|^2 = \frac{\mu - V_{ext}(r)}{g} \tag{1.7}$$

known as Thomas-Fermi (TF) approximation. The chemical potential can be calculated from the total atom number using Eq. 1.5 as

$$\mu = \frac{\hbar\omega_{ho}}{2}\left(15\frac{Na}{a_{ho}}\right)^{2/5}\,. \tag{1.8}$$

The condensate has the shape of an inverted parabola, modeled by the trap potential. The peak density is $n_0 = \mu/g$ and the extension of the condensate is determined by the Thomas-Fermi radii $R_j = \sqrt{2\mu/m\omega_j}$, allowing to rewrite Eq. 1.7 as

$$n_{TF}(x,y,z) = n_0\left(1 - \frac{x^2}{R_x^2} - \frac{y^2}{R_y^2} - \frac{z^2}{R_z^2}\right)\,. \tag{1.9}$$

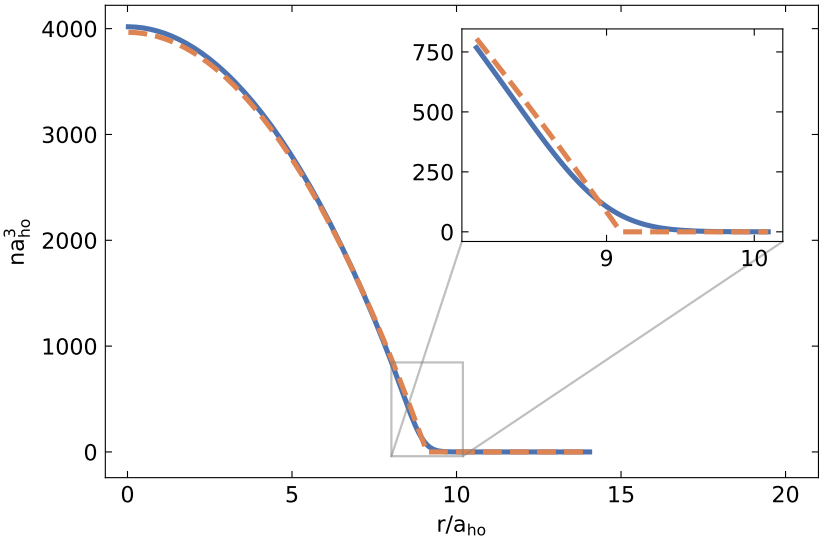

Figure 1.1: Comparison between the radial density profile calculated from the GPE (solid line) for a ^{23}Na condensate with 5×10^6 atoms in a spherical trap of frequency 40 Hz and the TF profile with the same number of atoms (dashed line). The radial coordinate and the density are normalized to the harmonic oscillator length a_{ho}. Inset: zoom of the surface region of the condensate, highlighting the difference in the density profile due to quantum pressure.

Fig. 1.1 compares the density distribution predicted by the GPE for a condensate of 5×10^6 atoms in a spherical trap of frequencies $\omega_{x,y,z} = 2\pi \times 40$ Hz with its TF approximation. The small differences at the edge of the condensate and in the peak density are due respectively to the quantum pressure contribution, which becomes non-negligible at the edges of the distribution, where the density is low, and to the difference in the chemical potential as computed by the GPE or using Eq. 1.8 (< 2%), as both distributions are normalized to the same number of atoms.

1.1.2 Superfluidity and vortex lines

Particle interactions affect the way a condensed gas exchanges energy with surrounding media through its elementary excitations. Bogolyubov's theory in a homogeneous BEC of density n at zero temperature shows that excitations of the condensate at wavevector k follow a phonon-like dispersion relation, linear at low k [12]. The low-energy modes of the BEC are wave-like collective oscillations called *phonons*, propagating with the sound velocity $c = gn/m$. Following the criterion formulated by Landau [15], the above property makes the weakly interacting Bose gas a superfluid, a fluid of particles able to flow with no viscosity or internal friction. This is in stark contrast with the case of the ideal Bose gas with no interactions ($g = 0$), where the excitation spectrum is instead quadratic in k, proper of non-interacting free particles, and the system doesn't show superfluidity.

One of the most characterizing properties of a superfluid system is its behavior under rotation, as a superfluid cannot rotate like a normal liquid: the absence of shear viscosity is actually a necessary condition for the presence of irrotational vortices. A vortex, a configuration of fluid rotating around a *nodal line*, is defined as irrotational when the vorticity $\vec{\omega} = \vec{\nabla} \times \vec{v}$, the curl of the velocity field, vanishes everywhere except than on the vortex line, where it is concentrated. The modulus of the velocity is inversely proportional to the distance r from the rotation axis, increasing indefinitely close to the

core. Such a configuration cannot be realized in normal fluids, where viscosity quickly dissipates the kinetic energy in the high-velocity core region, up to the creation of a region with diffused vorticity and a rigid rotational field where $|\vec{v}| \propto r$, as modeled by solutions to the classical fluid equations such as the Rankine or the Lamb–Oseen vortex model [16].

A vortex in a BEC is described by a solution of the stationary GP equation where all particles circulate with the same angular momentum $\hbar$ around a line at zero density. The velocity field is related to the phase ϕ of the wavefunction as

$$\vec{v} = \frac{\hbar}{m}\vec{\nabla}\phi\,, \tag{1.10}$$

which makes the flow irrotational since $\vec{\nabla} \times (\vec{\nabla}\phi) = 0$ identically. The circulation of the velocity $\Gamma = \oint \vec{v} \cdot d\vec{l}$ is constant for every contour enclosing the nodal line (and zero otherwise) and has the value

$$\Gamma = \frac{\hbar}{m}\oint d\vec{l}\cdot\vec{\nabla}\phi = \frac{\hbar}{m}\Delta\phi = 2\pi s\frac{\hbar}{m}\,, \tag{1.11}$$

where $\Delta\phi = 2\pi s$ is the variation of the phase around the contour, which must be an integer multiple of 2π for the wavefunction to be single-valued. This condition defines the vortex as quantized, as the angular momentum of the system, related to the circulation Γ, can assume only discrete values.

Looking for a symmetric solution within the above conditions, the wavefunction takes the form $\psi(r,\theta) = e^{is\theta}|\psi(r)|$, where s is an integer, in cylindrical coordinates around the vortex line. Substituting it in Eq. 1.4 with $V_{ext} = 0$ one obtains

$$-\frac{\hbar^2}{2m}\frac{1}{r}\frac{d}{dr}r\frac{d|\psi|}{dr} + \frac{\hbar^2 s^2}{2mr^2}|\psi| + g|\psi|^3 - \mu|\psi| = 0\,. \tag{1.12}$$

The solution, plotted in Fig. 1.2 for $s = 1$, shows that the wavefunction goes to zero at the vortex core as $r^{|s|}$, and recovers its bulk value $\sqrt{n} = \sqrt{\mu/g}$ within a distance $\xi = \hbar/\sqrt{2mgn}$ defined as *healing length*, determined by the balance between mean-field interactions and the kinetic energy due to rotation. In a ^{23}Na condensate with a typical density of 10^{20} atoms/m^3 the healing length has the value 0.3 µm, while in superfluid ^{4}He it is of the same order as the atom size because of the much stronger interactions.

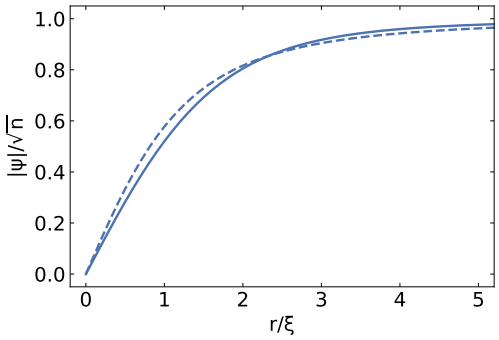

Figure 1.2: Solid line: numerical solution to Eq. 1.12 for a vortex with $s = 1$, normalized to the bulk value $\sqrt{n}$ and plotted vs. the rescaled coordinate $x = r/\xi$. The dashed line is the variational approximation $x/\sqrt{2+x^2}$ [17, chap. 9.2].

Considering a finite cylindrical volume of radius R and length L, the energy cost associated to the presence of the vortex can be calculated by the difference between the total energy of the vortex state and the one of a uniform system within the same volume. Both are calculated evaluating Eq. 1.2 for the corresponding wavefunctions. The result obtained is [10]

$$E_v = L\pi n\frac{\hbar^2}{m}\ln\left(1.464\frac{R}{\xi}\right)\,, \tag{1.13}$$

highlighting the important property that the energy of a vortex is proportional to the length of its nodal line.

A free vortex is an excited state of a static system, but it appears instead as the lowest energy configuration in the case of a rotating superfluid. For a system rotating with angular speed Ω the energy in a co-rotating reference frame is $E' = E - \Omega L$, where E is the same as in Eq. 1.2 and L is the total angular momentum carried by the wavefunction. For sufficiently high Ω a solution with nonzero angular momentum becomes energetically favorable, and a vortex is formed around the rotation axis. As the rotation speed increases more vortices appear, forming a regularly spaced array that distributes the angular momentum through the system.

Harmonically trapped BECs support vortex states as well. The geometry of the confinement plays an important role for the nature and stability of the defects, which we discuss in the case of a cylindrically symmetric trap where $\omega_y = \omega_z = \omega_\perp$ and $\omega_x = \lambda\omega_\perp$.

For $\lambda > 1$ the condensate has an oblate shape. As the energy of a vortex scales with the length of its nodal line, the preferred orientation is along the tightly confined direction x. In such a geometry vortices behave as point-like defects in two dimensions rather than as filaments in a 3D fluid. When the chemical potential μ is lower than the transverse confinement energy $\hbar\omega_x$, the system enters in an effective 2D regime. The energy cost of a vortex is now microscopic, because its length is always small compared to the system's size, and this allows for vortices to be thermally excited. This is a fundamental difference with respect to the 3D case, and it is at the basis of a phase transition known as Berezinskii–Kosterlitz–Thouless (BKT) transition [18, 19]: despite the reduced dimensionality prevents the creation of long-range order and the formation of a true Bose condensate [20], below a critical temperature T_{BKT} the system has a superfluid phase, characterized by the presence of bound pairs of vortices with opposite circulation.

For λ close to 1, spherical BECs host vortices as in a bulk homogeneous superfluid. The physics of vortices in such quantum systems share a number of properties with its classical counterpart. Without a preferred direction for the orientation, vortex filaments can easily bend [21–23], allowing for the creation of vortex tangles and the development of turbulence [24, 25].

In a cigar-shape geometry, for $\lambda < 1$, the condensate can support topological defects with different structures on the radial plane yz. The nature of the most stable defect, the one with the minimum energy, is determined by the dimensionality parameter $\gamma = \mu/\hbar\omega_\perp$ [26]. For $\gamma < 1$ the system is in a quasi-1D regime where the stable nonlinear excitations are dark solitons, characterized by a density depletion in the radial plane and by a phase jump of π across the defect. At higher values of γ the most stable structure is known as solitonic vortex (SV) [27, 28] which shares the characteristics both of a vortex and a soliton: the phase structure resembles the one of a vortex, with phase circulation around a zero-density nodal line that, to minimize its energy, is aligned in a random direction on the radial plane. Because of the anisotropic confinement, the phase gradient is higher close to the plane containing the vortex line, which reduces the density in that region. Looking from far away from the radial plane the SV resembles a 1D soliton, with a planar density depletion and an overall π phase jump. Fig. 1.3 shows the result of GPE simulations of a cigar-shaped condensate in 2D hosting the two different kinds of solitonic defects, comparing their density and phase profile.

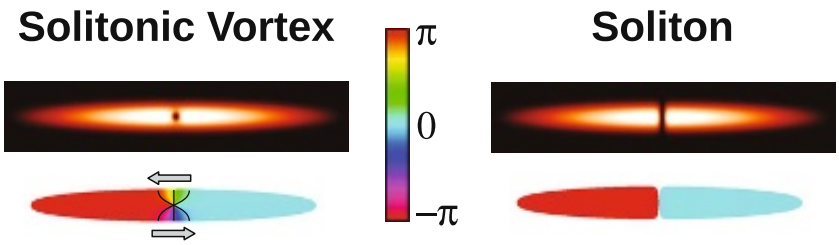

Figure 1.3: 2D GPE simulations showing the density (top) and phase (bottom) distribution of an elongated BEC hosting different kinds of defects. Left: the SV case, where the vortex core is accompanied by a weaker density depletion on the $y = 0$ line, where the phase gradient is stronger. Right: the dark soliton case, where the $y = 0$ line at zero density marks a π phase jump. Figure adapted from [28].

1.1.3 Free expansion of a vortex line

A sudden switch-off of the trapping potential induces a fast expansion of the condensate. The resulting decrease of the atomic density quenches the strength of mean-field interactions, with effects on both the expansion dynamics and on the shape of nonlinear defects such as solitons and vortex lines.

When the TF approximation is valid, the expansion dynamics can be described by simple scaling laws [**Castin1966**]. In a cigar-shaped elongated trap ($\lambda \ll 1$) the TF radii scale in time according to

$$\begin{aligned} R_\perp(\tau) &= R_\perp(0)\sqrt{1+\tau^2}\,, \\ R_x(\tau) &= R_x(0)\left[1+\lambda^2\left(\tau\arctan\tau - \ln\sqrt{1+\tau^2}\right)\right]\,, \end{aligned} \tag{1.14}$$

where $R_\perp = R_{y,z}$ is the radius on the radial plane yz, and $\tau = \omega_\perp t$. The expansion is much faster in the radial directions, which are the tightly confined ones. A known consequence of this is that the sample inverts its aspect ratio during the expansion, which is a hallmark of the presence of a Bose–Einstein condensate.

A simple model for the evolution of the core structure is obtained assuming that the vortex is a hollow cylinder of radius $r_v = c\xi$, with c a constant number expected to be of order 1. The decrease of the density divides the expansion dynamics in two different regimes, which are distinguished by the role of mean-field interaction energy. At early times, where the density is still high, the expansion is mainly driven by mean-field energy. In this regime the size of the core can be expected to follow adiabatically the dependency of the healing length on the instantaneous peak density n_0, whose scaling in time can be derived from conservation of the total number of atoms $N \propto n_0 R_\perp^2 R_x$ during the expansion. At lowest order in λ we neglect the slow axial expansion and find that the peak density scales as

$$n_0 \sim \frac{R_\perp^2(0)}{R_\perp^2(\tau)} = \frac{1}{1+\tau^2}\,, \tag{1.15}$$

so that the vortex core radius expands as $\sqrt{1+\tau^2}$. At later times instead, when the gas becomes more dilute, atomic interactions can be neglected and the expansion becomes ballistic. Both TF radii increase linearly in τ and the size of the vortex is expected to scale proportional to that of the condensate. For a BEC in a spherical trap with frequency ω the crossover from mean-field to ballistic regime happens at around $\tau_{dec} \sim \sqrt{2\mu/\hbar\omega}$ [29].

The free expansion increases the optical visibility of the vortex, due to the different scaling laws with which the condensate radii and the vortex core expand. The profile obtained by imaging the condensate along the x direction is proportional to the *column density*

$$n_{TF}^{col}(y) = n_{TF}^{col}(0)\left(1 - \frac{y^2}{R_\perp^2}\right)^{3/2}, \tag{1.16}$$

where $n_{TF}^{col}(0) = 4n_0R_x/3$, obtained integrating Eq. 1.9 along x and considering a slice on the plane $z = 0$.

A straight vortex line oriented along z will produce a dip in the column density, as it depletes a narrow region of the sample. The dip is expected to be small, as the transverse extension of the vortex is much smaller than the size of the BEC, and maximum for a vortex located in the center of the condensate. We compute the same quantity $n_v^{col}(y)$ for the density distribution containing a cylindrical vortex located at $x = y = 0$, and define the rescaled visibility of the vortex line as $\delta n_v(y) = (n_v^{col}(y) - n_{TF}^{col}(y))/n_{TF}^{col}(0)$, which reads

$$\delta n_v(y) = -\frac{3}{2}\frac{\sqrt{r_v^2 - y^2}}{R_x}\left(1 - \frac{y^2}{R_\perp^2}\right)\left[1 - \frac{R_\perp^2}{3R_x^2}\frac{r_v^2 - y^2}{R_\perp^2 - y^2}\right] \tag{1.17}$$

for $y < r_v$, and zero otherwise. Defining the rescaled vortex radius $\tilde{r}_v = r_v/R_\perp$, which is constant during the expansion, and the rescaled coordinate $\tilde{y} = y/R_\perp$, we explicit the time dependency of the vortex visibility as

$$\delta n_v(\tilde{y}, \tau) = -\frac{3\lambda}{2}\tilde{r}_v\sqrt{1+\tau^2}(1-\tilde{y}^2)\left(1 - \frac{\tilde{y}^2}{\tilde{r}_v^2}\right)^{1/2} \tag{1.18}$$

where we dropped the last term in square brackets in Eq. 1.17 which is $\mathcal{O}(\lambda^2)$.

1.1.4 Production and observation of vortices

Quantized vortices have been extensively studied in superfluid helium systems [30], with seminal experiments which used rotating buckets to introduce vortices in the superfluid. The extremely small width of the nodal line precluded a direct observation, so vortices were revealed either indirectly by their effects on sound propagation [31] or employing tracer particles like electrons [32], solid hydrogen [33] and He_2 excimers [34].

In ultracold atomic gases, vortices are produced and observed with different techniques [35]. There are numerous method that exploit the mechanical action of a time-varying potential on the gas, which is reminiscent of the rotating bucket method used with ^{4}He. A stirring laser beam [36, 37], a rotating elliptic magnetic potential [38], or a combination of the two [39] were used to put the condensate in rotation at high speed, observing vortices nucleate at the edge of the sample, where the density is low and their energy cost is reduced, and migrate towards the center forming a triangular lattice. Vortex lattices have been arranged in different regularly spaced geometries by stirring the BEC with a rotating optical lattice [40]. By sweeping an optical obstacle through the superfluid, it is possible to deterministically create a few vortices, or vortex-antivortex pairs, and manipulate the vortices by pinning them to the optical potential [41]. A sweeping laser beam was also used to demonstrate the creation of Von Karman's vortex streets shedding past the obstacle [42].

Vortices can be injected in a superfluid by directly engineering the phase of the system's wavefunction. In a two-component BEC, vortices were created by manipulating the coherent coupling between two atomic states with a rotating potential [43], exploiting

the presence of the non-rotating condensate in the other component to measure the circulating phase of the vortex with an interferometric imaging. The same technique was later used to create dark solitons which, being unstable in the given geometry, were seen to decay into vortex rings [44]. A two-beam Raman coupling was used to transfer angular momentum to a single-component BEC from a Laguerre–Gauss laser beam [45].

Vortices can naturally arise as phase defects while crossing the BEC transition, in a phenomenon common to second-order phase transitions known as the Kibble–Zurek mechanism [46, 47]. The spontaneous formation of vortices after fast temperature quenches resulting from the relaxation of a random pattern of independent phase domains was observed both in 3D [48, 49] and 2D systems [50]. The phase relaxation dynamics was explored in a controlled way by merging independently created condensates, both in small number [51, 52] or releasing a big number of them from the sites of an optical lattice [53]. The dynamics of the cooling process has been theoretically studied using finite-temperature GPE models [54], describing the chaotic nature of the process and the resulting turbulent post-quench dynamics. This leads to the survival of a random number of defects after relaxation, that can be experimentally observed and counted, measuring the power law scaling of their average number with the quench time [49, 55].

The direct in-situ observation of vortices is made difficult by the small size of the defect, often lower or comparable to the resolution of the imaging system. Although achieved in-situ by the use of high-numerical-aperture optics and dark-field imaging methods [56], the vast majority of the observations relies on time-of-flight (TOF) imaging, where the condensate is released from the trap and let expand for a suitable time before being imaged. The vortex core expands together with the background density [29, 57] which allows for optical detection. This method was used in nearly all of the above cited works to obtain single snapshots of vortical configurations, and allowed also to investigate the shape of a single vortex in different geometries. In the quasi-2D case the density distribution develops characteristic ring structures due to interference between the vortex velocity field and the one of the surrounding fluid [58]. In the 3D cigar-shaped geometry the nonlinear phase gradient of the SV gives rise to a characteristic S-shaped twist in the density depletion, that is observed when the nodal line is parallel to the imaging direction [23], while imaging along the axis of the sample reveals that the core structure in the bulk has approximately the same shape as in a homogeneous condensate. One of my PhD projects was related to this topic, as detailed in Chap. 4, where I performed measurements of the structure of the vortex core after expansion and quantitatively compared them to the predictions of the GPE [59].

The investigation of vortex dynamics requires instead a non-destructive imaging method. A compromise between the need of TOF expansion and the possibility of repeated imaging is found with the use of output coupling methods [60–62]. A small fraction of atoms is transferred to a non-trapped state and imaged after expansion, obtaining a snapshot of the density distribution of the system at the time of the extraction without interrupting the in-situ dynamics. Such a method has been used to observe the dynamics of isolated vortices [61, 63, 64] and to observe vortex-vortex interactions [65].

1.2 Thermodynamics of finite-temperature BEC

In the textbook model of an ideal Bos gas, condensation is determined by a single parameter, the phase space density (PSD) $\mathcal{D} = n\lambda_T^3$, depending on the ratio between the interparticle distance and the thermal de Broglie wavelength $\lambda_T = (2\pi\hbar^2/mk_BT)^{1/2}$ associated to the temperature T. The PSD expresses the degree of degeneracy in the

system, as condensation starts when it reaches a critical value of order 1. This picture is valid also in the case of an interacting gas. Anticipating a result given by mean-field theory, interaction effects grow proportionally to the density, so that they are expected to be important only once the system enters the condensed phase, and to affect the condition for condensation only in a minimal way. For the same reason the geometry of the confinement becomes important, changing the spatial distribution of condensed and thermal atoms, such that the uniform and the harmonically trapped case now show significant differences.

Effects of particle interactions can be revealed by the equation of state of the system. An equation of state (EoS) is a relation holding between three thermodynamic variables, which summarizes the thermodynamic properties of the system. There is not a unique expression for it since, given a particular form of the EoS relating three variables of choice, analogous relations for any other triplet of variables can be obtained using Maxwell's relations. The EoS carries information about the presence of phase transitions in the system, which are accompanied by discontinuities in the derivatives of the free energy [66] and show up as singular points in the EoS profile.

In superfluid systems such as the interacting Bose gas, the phononic contribution to the free energy gives rise to a peculiar non-monotonic behavior of the chemical potential with temperature [67]: close to $T = 0$ the chemical potential must be increasing, as the slope $\partial\mu/\partial T$ can be related to the sound velocity, which is positive for all the known kinds of superfluids. In the opposite regime of high temperatures μ is negative and decreasing, going in the limit of a non-interacting Boltzmann gas. This implies that the chemical potential has a peak (at least one) as a function of temperature, and theoretical models for different kinds of superfluid systems predict the peak to be right at the normal-to-superfluid phase transition temperature. This observation leads to speculate that such a feature is general to the superfluid transition, even thought there is still no rigorous theoretical proof for this claim, and makes it worth of further experimental investigation.

In the following sections, I will introduce the theory for the thermodynamics of an interacting Bose gas, show how it predicts the EoS for the chemical potential, and I will review the experimental observation of its features in many superfluid systems other than the Bose gas.

1.2.1 Hartree–Fock theory

The simplest theory accounting for interactions in the thermodynamics of a bosonic gas is the Hartree–Fock (HF) theory. In this framework, the particles constituting the many-body system are distributed among statistically independent single-particle states, whose occupation numbers enter in the definition of the energy and have to be computed self-consistently.

We start from Eq. 1.1 for the many-body hamiltonian H. We can decompose the quantum field operator $\hat{\psi}$ in the form

$$\hat{\psi}(r) = \sum_i \varphi_i(r) a_i \tag{1.19}$$

where φ_i are wavefunctions for single-particle states, normalized to unity, and a_i ($a_i^\dagger$) are the corresponding annihilation (creation) operators. The HF prescription is to evaluate the total energy $E = \langle H \rangle$ retaining the product of at most two particle operators, with

the following substitutions:

$$\begin{aligned}
&\langle a_i^\dagger a_j \rangle = n_i \delta_{ij} \,, \\
&\langle a_i^\dagger a_j^\dagger a_k a_l \rangle = n_i n_j (\delta_{ik}\delta_{jl} + \delta_{il}\delta_{jk}) \quad \text{for } i \neq j \,, \\
&\langle a_i^\dagger a_i^\dagger a_i a_i \rangle = n_i (n_i - 1) \,.
\end{aligned} \tag{1.20}$$

The energy obtained in this way describes a gas of independent bosonic particles at equilibrium in a self-consistent potential, determined both by the external potential and by mutual interactions. The particle occupation numbers n_i are determined by minimizing the grand canonical potential $\Omega = E - TS - \mu N$, where the number of atoms $N = \sum_i n_i$ and the entropy

$$S = k_B \sum_i \left[(1 + n_i) \ln(1 + n_i) - n_i \ln n_i \right] \tag{1.21}$$

are fixed respectively by the chemical potential μ and by the temperature T.

The minimization leads to the result

$$n_i = \frac{1}{e^{(\epsilon_i - \mu)/k_B T} - 1} \tag{1.22}$$

proper of Bose–Einstein statistics, where ϵ_i are the energies of the single-particle levels, determined by

$$\epsilon_i = \frac{\delta E}{\delta n_i} \,. \tag{1.23}$$

Homogeneous systems

For a homogeneous system of bosons with $V_{ext} = 0$ confined in a volume V, the natural choice for the single-particle wavefunctions is that of plane waves $\varphi_k = e^{ikr}/\sqrt{V}$, labeled by the wavevector k. Substituting it in Eq. 1.19 and using the prescription 1.20, the energy of the system is

$$E = \sum_k \frac{\hbar^2 k^2}{2m} n_k + g n^2 V \,, \tag{1.24}$$

where we substituted the particle density $n = \sum_k n_k / V$. The single-particle energies

$$\epsilon_k = \frac{\partial E}{\partial n_k} = \frac{\hbar^2 k^2}{2m} + 2gn \tag{1.25}$$

show that the system can be thought as composed by non-interacting particles whose energy is shifted by the mean-field contribution $2gn$. The density can be explicitly calculated by replacing the sum over wavevectors by an integral,

$$\frac{1}{V} \sum_k n_k \to \int \frac{d^3 k}{(2\pi)^3} n_k \,, \tag{1.26}$$

obtaining

$$n = \frac{1}{\lambda_T^3} g_{3/2} \left(e^{(\mu - 2gn)/k_B T} \right) \,, \tag{1.27}$$

where $g_\nu(z)$ is the polylogarithm function with index ν [68]. The replacement of a discrete sum over the levels with an integral becomes exact in the thermodynamic limit,

where $V \to \infty$ keeping the density n constant, and it is allowed since none of the states φ_k is macroscopically occupied.

Eq. 1.27 fixes a relation between the chemical potential and the PSD of the system. By decreasing the temperature at fixed density (or either introducing particles at fixed temperature) the PSD must increase, hence μ will increase accordingly. Bose–Einstein condensation starts at the point where μ reaches the energy of the lowest-lying single-particle state, which is the one at $k = 0$ with $\epsilon_0 = 2gn$. This defines a critical temperature T_c where $n\lambda_{T_c}^3 = \zeta(3/2)$, or

$$T_c = \frac{2\pi\hbar^2}{mk_B}\left(\frac{n}{\zeta(3/2)}\right)^{2/3}, \tag{1.28}$$

where we used the fact that, for $z = 1$, the polylogarithm functions assume the values of the Riemann zeta function, $g_\nu(1) = \zeta(\nu)$.

For temperatures below T_c a macroscopic number of atoms occupies the lowest-energy state. Its contribution to the occupation of the system has to be separated from the other states, substituting Eq. 1.19 with

$$\hat{\psi}(r) = \sqrt{n_0} + \sum_{k\neq 0} \frac{e^{ikr}}{\sqrt{V}} a_k \tag{1.29}$$

and replacing each occurrence of $a_{j=0}$ in Eq. 1.20 with $\sqrt{n_0}$, where n_0 is the density of condensed atoms. The total energy now has the form

$$E = \sum_{k\neq 0} \frac{\hbar^2 k^2}{2m} n_k + V\left(\frac{1}{2}gn_0^2 + 2gn_T n_0 + gn_T^2\right) \tag{1.30}$$

where $n_T = \sum_{k\neq 0} n_k/V$ is the density of the thermal component. The chemical potential is identified with the lowest energy level ϵ_0, so that

$$\mu = \frac{\partial E}{\partial n_0} = gn_0 + 2gn_T\,, \tag{1.31a}$$

$$\epsilon_k = \frac{\partial E}{\partial n_k} = \frac{\hbar^2 k^2}{2m} + 2g(n_0 + n_T)\,, \tag{1.31b}$$

and the density of the thermal fraction can be calculated using again Eq. 1.26. The thermal and the condensate density are to be determined self-consistently from the coupled equations

$$n = n_0 + n_T\,, \tag{1.32a}$$

$$n_0 = \mu/g - 2n_T\,, \tag{1.32b}$$

$$n_T = \frac{1}{\lambda_T^3} g_{3/2}\left(e^{(\mu-2gn)/k_BT}\right). \tag{1.32c}$$

The solutions to Eq. 1.27 and to Eq. 1.32 constitute the equation of state (EoS) for the bosonic gas, defining the relation $\mu(n, T)$ respectively in the normal and in the condensed phase. The result is plotted in Fig. 1.4b: from $\mu = gn$ at zero temperature, the chemical potential peaks at the value $\mu = 2gn$ at the transition point (where $n_0 = 0$), and then falls down to negative values in the normal phase.

The equation for the pressure can be found from the relation $\Omega = -pV$ holding for the grand canonical potential, leading to

$$p = gn^2 - \frac{1}{2}gn_0^2 + \frac{k_BT}{\lambda_T^3} g_{5/2}\left(e^{(\mu-2gn)/k_BT}\right), \tag{1.33}$$

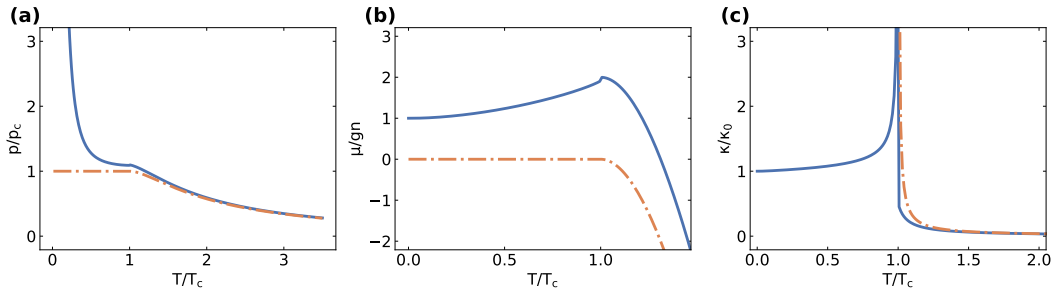

Figure 1.4: Equation of state for three thermodynamic variables at fixed density, as a function of the reduced temperature T/T_c. (a) Pressure p normalized to the value in the condensed phase for an ideal gas at the same temperature $p_c = k_B T\zeta(5/2)/\lambda_T^3$. (b) Chemical potential μ normalized to the zero-temperature value gn. (c) Compressibility κ normalized to the zero-temperature value $\kappa_0 = 1/gn^2$. The solid lines are for an interacting ^{23}Na gas with density 10^{20} atoms/m^3. The dashed lines are for an ideal Bose gas with the same density.

which depends on the density even in the condensed phase due to mean-field interactions.

The isothermal compressibility

$$\kappa = \frac{1}{n}\left.\frac{\partial n}{\partial p}\right|_T \tag{1.34}$$

has the finite value $1/gn^2$ at $T = 0$, and diverges at the transition. These results have to be compared with the ideal gas case (Fig. 1.4), where in the BEC phase the pressure does not depend on the density, the chemical potential is fixed to the value $\mu = 0$ and the compressibility, still diverging at T_c, is always infinite.

Trapped gases

The Hartree–Fock approximation applies also to systems confined by an external potential V_{ext}. When a condesate is present, the proper form for the field operator 1.19 is

$$\hat{\psi}(r) = \psi_0(r) + \sum_{i\neq 0} \varphi_i(r) a_i \tag{1.35}$$

which leads to the expression for the total energy

$$E = \int d^3r \left[\frac{\hbar^2}{2m}|\vec{\nabla}\psi_0|^2 + \sum_{i\neq 0}\frac{\hbar^2}{2m} n_i |\vec{\nabla}\varphi_i|^2 + V_{ext}(n_0 + n_T) + \frac{1}{2}gn_0^2 + 2gn_T n_0 + gn_T^2\right] . \tag{1.36}$$

Here ψ_0 is the condensate wavefunction, and the densities are determined by

$$\begin{aligned} n_0(r) &= |\psi_0(r)|^2 \\ n_T(r) &= \sum_{i\neq 0} n_i |\varphi_i(r)|^2 \end{aligned} \tag{1.37}$$

respectively for the condensed and the thermal fraction.

Eq. 1.22 holds for the occupation numbers n_i also in this case. The wavefunctions ψ_0 and φ_i are to be determined together with their energies $\epsilon_0 = \mu$ and ϵ_i from the

variational equation

$$\frac{\delta E}{\delta \varphi_i^*} = n_i \epsilon_i \varphi_i \,, \tag{1.38}$$

which stems together with Eq. 1.23 from the minimization of the grand-canonical potential Ω. This leads to the system of nonlinear Schrödinger equations for the wavefunctions [69]

$$\left[-\frac{\hbar^2}{2m}\nabla^2 + V_{ext}(r) + g(|\psi_0|^2 + 2n_T) \right] \psi_0 = \mu \psi_0 \,, \tag{1.39a}$$

$$\left[-\frac{\hbar^2}{2m}\nabla^2 + V_{ext}(r) + 2g(|\psi_0|^2 + n_T) \right] \varphi_i = \epsilon_i \varphi_i \,, \tag{1.39b}$$

which are the analogous of Eq. 1.31 in the trapped system. The normalization of ψ_0 is determined by the constraint

$$N = \int (|\psi_0|^2 + n_T)\, d^3 r \tag{1.40}$$

for the total number of particles. At $T = 0$, all occupation numbers for $i > 0$ vanish, leaving $n_T = 0$. Eq. 1.39a coincides with the stationary GPE (Eq. 1.4), which now can be interpreted as the HF equation for the ground state.

The density of the thermal component can be calculated in a semiclassical approximation: when the length scale of the spatial variations in the potential is bigger than the wavelength of typical excitations, the wavefunctions for the excited states can be approximated by plane waves, $\varphi(r) \sim e^{ikr}$, which is equivalent to solving Eq. 1.39b within the WKB approximation [17, 69]. This leads to the semiclassical expression for the single-particle energies

$$\epsilon(k, r) = \frac{\hbar^2 k^2}{2m} + V_{ext}(r) + 2gn(r) \,, \tag{1.41}$$

which can be substituted in the k-integral in Eq. 1.27 to obtain

$$n_T(r) = \frac{1}{\lambda_T^3} g_{3/2}\left(e^{(\mu - V_{ext}(r) - 2gn(r))/k_B T} \right) . \tag{1.42}$$

The substitution is exact for $V_{ext} = 0$, where we find back the results of Eq. 1.31 for the uniform system, with a homogeneous condensate density and excited states in the form of plane waves. The semiclassical approximation is more precise at high temperatures, where the occupation of high-energy modes is bigger. In particular, it is valid for temperatures above the transition, hence it can be used to compute the mean-field corrections to the critical temperature for a trapped gas [70].

A mean-field treatment of the interactions given by the Hartree–Fock theory already captures most of the relevant aspects of the thermodynamics, and it has been tested against more complicated self-consistent schemes such as the Popov approximation [70], as well as against exact Monte Carlo calculations [71]. In the case of weakly-interacting homogeneous gas, it is possible to give a universal description of the phase transition accounting for the role of thermal fluctuations [72], which confirms the peak value of $\mu = 2gn$ at the transition even beyond mean-field theory.

1.2.2 Local density approximation

Equations 1.39a, 1.42 and 1.40 altogether predict the density distribution of a finite-temperature Bose gas in the external potential V_{ext}. An alternative approach for the description of trapped systems, based on the knowledge of the EoS of homogeneous matter, relies on the local density approximation (LDA).

When the potential V_{ext} varies smoothly in space, the gas occupying a small volume at position r can be thought as a homogeneous system in thermal and chemical equilibrium with the surrounding ones. The global chemical potential μ_0 that determines the flux of particles between the small volumes, hence the density distribution, has two contributions: one coming from the external potential, and another one coming from the chemical potential $\mu(n,T)$ of the local homogeneous ensamble of particles at density n. The condition for the density distribution is then given by

$$\mu_0 = \mu[n(r),T] + V_{ext}(r)\,. \tag{1.43}$$

The density distribution in the generic potential V_{ext} can then be calculated from the EoS $n(\mu,T)$ for the same homogeneous system with the substitution $\mu \to \mu_0 - V_{ext}$. If applied to the interacting gas at $T=0$, where $\mu = gn$, one finds the TF approximation 1.7 for the trapped condensate. Substituting it in Eq. 1.27 we recover the semiclassical result 1.42 for the distribution of the thermal component.

This opens an alternative approach for the study of the EoS of homogeneous quantum systems, which can be experimentally obtained from the measurement of the density profile $n(r)$ in a trapped sample, of the trapping potential V_{ext}, and of the global thermodynamic quantities μ_0 and T.

Following this route, T. L. Ho and Q. Zhou demonstrated a method to measure the pressure EoS $p(\mu,T)$ from in-situ images of harmonically trapped gases [73, 74]. We apply the Gibbs–Duhem relation

$$dp = nd\mu + sdT\,, \tag{1.44}$$

where s denotes the entropy density, to relate the pressure gradient to the trapping potential within LDA. As nearby points are in thermal equilibrium, their temperature is the same, so that $dT=0$, while according Eq. 1.43, $d\mu = d(\mu_0 - V_{ext}) = -dV_{ext}$.

The value of the pressure $p(x)$ at a point $(x, y=0, z=0)$ along the axis of a trapped cloud can be found integrating Eq. 1.44 at fixed temperature. In the same point the chemical potential takes the value $\mu(x) = \mu_0 - V_{ext}(x,0,0)$. Integrating from infinite distance, where $\mu = -\infty$ and $p=0$, to the point x, we obtain

$$p(x) = \int_{-\infty}^{\mu(x)} n(\mu)d\mu = \int_{V_{ext}(x)}^{+\infty} n(\mu_0 - V_{ext})dV_{ext}\,. \tag{1.45}$$

For a harmonic trapping potential (Eq. 1.6), at fixed x,

$$dV_{ext}(x,y,z) = m(\omega_y^2\, ydy + \omega_z^2\, zdz) = m\frac{\omega_y\omega_z}{2\pi}\, dydz\,, \tag{1.46}$$

so we can integrate Eq. 1.45 over the yz plane and find

$$p = \frac{m\omega_y\omega_z}{2\pi}\int n\, dydz = \frac{m\omega_y\omega_z}{2\pi} n_1\,, \tag{1.47}$$

relating the pressure along the trap axis with the doubly-integrated density $n_1 = \int n\, dydz$.

The Gibbs–Duhem equation also allows to compute the 3D density along the trap axis as $n = (\partial p/\partial \mu)_T$. The change in the potential along x at fixed $y = z = 0$ is $dV_{ext} = m\omega_x^2\, x dx$, so differentiating the pressure along x leads to

$$n = \frac{dp}{d\mu} = -\frac{1}{2\pi x}\frac{\omega_y\omega_z}{\omega_x^2}\frac{dn_1}{dx}\,. \tag{1.48}$$

Once the density profile is known, the isothermal compressibility can be computed using again Eq. 1.44. Substituting in Eq. 1.34, we obtain

$$\kappa = \frac{1}{n^2}\frac{dn}{d\mu} = -\frac{1}{mn^2\omega_x^2 x}\frac{dn}{dx}\,. \tag{1.49}$$

The power of the above described method is that it allows to measure the 3D density of the sample. This is a rather unusual observable in 3D systems to have access to, as all imaging methods can only measure the column density, integrated along the line of sight. Although restricted only to the trap axis, this is sufficient to determine the complete homogeneous EoS in the LDA scheme. For non harmonic potentials the principle of the method remains the same: a precise measurement of the trapping potential allows to obtain the axial pressure and density after proper modifications of Eq. 1.46.

The LDA corresponds to neglecting gradient terms in the equation determining the density profile. As density gradients are associated with kinetic energy, a condition for the validity is that the kinetic energy is negligible with respect to the other energy scales in the system.

For a trapped condensate at zero temperature the LDA coincides with the TF approximation for the density profile, which differs significantly from the exact GPE solution only at the edges, where the gradient in the potential is stronger. We can use an energy scaling argument to estimate the thickness of the surface region where the approximation fails [75, 76]. Considering a spherical trap of frequency ω, the TF wavefunction scales as $\psi \sim \sqrt{R-r}$ close to the condensate boundary, where R is the TF radius. The kinetic energy per particle can be estimated as

$$\frac{\hbar^2}{2m}\frac{|d\psi/dr|^2}{|\psi|^2} \sim \frac{\hbar^2}{2m(R-r)^2}\,. \tag{1.50}$$

This has to be compared with the interaction energy per particle, scaling as the local chemical potential

$$\mu - \frac{1}{2}m\omega^2 r^2 \sim F(R-r)\,, \tag{1.51}$$

where $F = m\omega^2 R$ is the trapping force acting on the particles at the edge of the condensate. The TF approximation breaks in the region for $R - r \lesssim \delta$ where the kinetic energy dominates, with

$$\delta = \left(\frac{\hbar^2}{2mF}\right)^{1/3} = \frac{R}{2}\left(\frac{\hbar\omega}{\mu}\right)^{2/3}\,. \tag{1.52}$$

1.2.3 Measurement of the EoS in superfluid systems

The experimental research on the thermodynamics of superfluid ^{4}He focused on its properties at the phase transition, signaled by the characteristic peak in the specific heat at the transition temperature $T_\lambda = 2.1\,\mathrm{K}$, the so-called lambda point [77, chap. 8]. The peak feature in the chemical potential has been indirectly measured in superfluid ^{4}He.

Data from specific heat measurements allow to model the thermodynamic free energy of the fluid [78], from which it is possible to extract the EoS for $\mu(T)$ [67], showing a non-monotonic behavior due to the contribution of rotonic excitations in the system.

In ultracold atomic gases, the possibility to directly access the density and momentum distributions of the sample in experimental images is the principal tool for studying the thermodynamics of such systems.

The theory of the harmonically trapped interacting Bose gas, subject of immediate comparison with experimental results, has been developed with a focus on trap-averaged parameters [14, 79–82] and to the effect of atomic interactions on the global thermodynamic features of the sample, such as the mean-field shift of the critical temperature [83–85] and the divergence in the condensate number fluctuations at the transition [86].

With the recent realization of flat-potential optical traps [87] it became possible to obtain homogeneous Bose–Einstein condensates, and to confirm the mean-field theory predictions on the momentum distribution, interaction energy, and TOF dynamics [88].

Adopting the viewpoint of LDA, the homogeneous gas thermodynamics has been measured on trapped samples of many different quantum fluids. In 2D Bose gases, it has been observed the universal scaling of the thermodynamic quantities across the BKT transition [89–91]. In unitary Fermi gases, realized in ultracold atoms tuning the scattering length to infinity with the use of Feschbach resonances, it was possible to explore the BEC–BCS phase transition taking place in such systems [92], and to measure the EoS of the fluid at unitarity [93–96], confirming the presence of the peak in the chemical potential at the onset of the superfluid transition [97].

The LDA approach has been applied also in the case of 3D weakly interacting Bose gases, exploring the EoS in the form $p(\mu, T)$. The sharp rise in the pressure profile due to the mean-field repulsion, enhanced by the presence of the condensate, has been observed at the transition point [98]. In the regime of low temperature and strong interactions instead, it was possible to measure the Lee–Huang–Yang correction to the pressure arising from the contribution of quantum fluctuations [99]. At present, there are no experimental observations of the peak in the chemical potential at the transition.

1.2.4 Universality

Starting from general principles, any equation of state relating three thermodynamic variables of choice will also depend on the microscopic parameters in the system's hamiltonian. In the case of a dilute gas this includes the coupling constant g, which completely specifies atomic interactions, the mass of the particles, as well as fundamental constants like $\hbar$.

We can sort out the number of relevant parameters using dimensional analysis, choosing a set of dimensionally independent variables to rescale all the other quantities in the problem. In special regimes such as at zero temperature or at infinite interactions, some parameters must be directly dropped out of the equation, because the corresponding dimensional scale cannot be compared any more with the remaining ones. A universal regime is reached when such simplifications leave the equation of state dependent on one single parameter, such as even very different physical systems will behave the same after proper rescaling of the relevant variables [100].

Scanning through the density distribution of a trapped sample in the LDA measurement, we are moving on the EoS surface along a line at constant temperature. In a system showing universal thermodynamics this is sufficient to explore the complete equation of state, as varying any thermodynamic coordinate will correspond to scanning

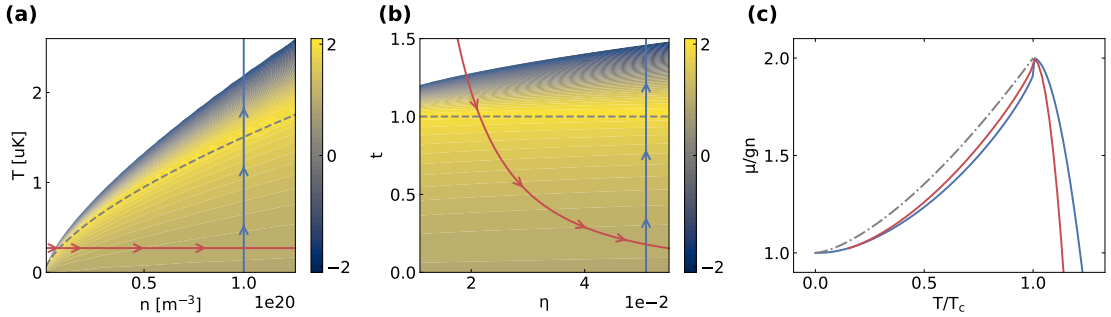

Figure 1.5: (a) 2D plot of the function $\mu(n,T)/gn$. The colormap is limited for clarity to values $|\mu| \leq 2$, and μ is monotonically decreasing in the non-colored area. The dashed line marks the BEC transition, where $T = T_c(n)$. The blue and red lines with arrows are respectively paths at constant density (10^{20} atoms/m^3) and constant temperature (270 nK). (b) Same as (a), replotted as a function of (η, t). The BEC line is at $t = 1$, and the blue and red paths are transformed to the new coordinates. (c) The μ vs. t curve along the blue and red paths, in corresponding colors. The dot-dashed line is the simplified form $1 + t^{3/2}$, independent of η.

through the single dimensionless parameter the EoS depends on.

Let's focus the discussion on the chemical potential, where the above considerations bring to the expression $\mu = \mu(n, T, g, \hbar, m)$. We take out the dependency on the density, which also sets the temperature scale $T_c \propto \hbar^2 n^{2/3}/m$ identified with the critical temperature, and rewrite the chemical potential in the form

$$\frac{\mu}{gn} = f\left(\frac{T}{T_c}, \frac{gn}{k_B T_c}\right) = f(t, \eta) \tag{1.53}$$

as a function of the coordinates $t = T/T_c$ and $\eta = gn/k_B T_c \propto an^{1/3}$.

In the weakly interacting Bose gas, without other general considerations we must conclude that the system does not have a universal thermodynamics. Using the Hartree–Fock theory we derive a model for the equation of state, and find that there is a regime of "weak universality" where the above expression can be approximated as independent of η in a suitable range of density and temperatures.

From Eqs. 1.32 we can write $\mu/gn = 1 + n_T/n$ in the condensed phase. In a regime of intermediate temperatures where the BEC fraction is not too high, we can set $(\mu - 2gn)/k_B T \ll 1$ and expand the polylogarithm $g_{5/2}(z)$ in Eq. 1.32b around $z \lesssim 1$. Keeping terms up to the first correction in η leads to

$$\frac{\mu}{gn} = 1 + t^{3/2} - \frac{2\sqrt{\pi}}{\zeta(3/2)} t \sqrt{\eta(1 - t^{3/2})} + \mathcal{O}(\eta)\,. \tag{1.54}$$

The expansion is valid in the region $\eta \ll t < 1$, which ensures the above condition $\mu - 2gn \ll k_B T$ and physically corresponds to the regime of temperatures $\mu \lesssim T \lesssim T_c$. At a density $n = 10^{20}$ atoms/m^3 we have $\eta = 0.05$ and the above expression differs from the true HF result by less than 3%. The distance of the HF result from the universal curve $1 + t^{3/2}$ is ≤ 0.1 in all the range $t < 1$.

This estimates the error we are making by comparing the LDA method, which is a measure at fixed temperature, to the theory curve at fixed density shown in Fig. 1.4b. In Fig. 1.5 we plot the chemical potential respectively as a function of (n, T) (a) and of (η, t) (b), and show how an iso-density and isothermal line look like in both coordinate spaces, for values of $T = 270$ nK and $n = 10^{20}$ atoms/m^3 that are reasonable for our experiment. We plot in (c) the chemical potential profile we get along each of the two paths. Figs.

(b-c) show how moving along the LDA path at fixed T we are simultaneously varying both t and η, and that the weak dependency of Eq. 1.54 on η makes the two μ profiles differ for less than 2%, allowing to neglect the non-universal dependency on the density in the condensed phase.

Chapter 2

Production of Bose–Einstein condensates

2.1 Experimental setup

The production of Bose–Einstein condensates is a rich topic in experimental physics. Since the first attempts to cool down and manipulate atoms [7] to the first realization of a BEC [5, 6], the technological progress in atomic physics of the last decades allowed for the development of more and more advanced experiments. This not only deepened our knowledge about fundamental physics, but also led to important advances in research fields such as metrology [101] or to the beginning of new ones like quantum information [102].

Yet, the basic ingredients of an atomic physics experiment remained the same, although evolved and refined through the years: vacuum technology, production of coherent laser light, control of radio-frequency (RF) and microwave radiation and static electric and magnetic fields. All of this requires an automated control of the hardware and precise timing of the experimental sequence.

In this chapter I will describe our experimental setup [103], detailing the upgrades implemented during the course of my PhD.

2.1.1 Vacuum system and atomic source

The vacuum apparatus, sketched in Fig. 2.1a, is built with AISI 316 stainless steel and is divided in two sections: a high-vacuum chamber (HV) at a pressure of 10^{-7} mbar, hosting the atomic source, and a ultra-high-vacuum (UHV) chamber with pressure down

to 10^{-10} mbar hosting the science cell. An ion pump VARIAN STARCELL with nominal pumping speed of $55\,\mathrm{L\,s^{-1}}$ and a secondary titanium sublimation pump (VARIAN TSP) are attached to each of the two parts. The two sides are connected by a differential pumping channel of diameter 2 mm and length 22.8 mm.

In our experiment the atomic species of choice is ^{23}Na, whose level structure is shown in Fig. 2.2 [104]. The atomic source, hosted in the HV section, consists of a transversely loaded two-dimensional magneto-optical trap (2D MOT) with a push beam. This design, first developed for a lithium experiment [105], allows to realize a high-flux atomic source with compact hardware.

^{23}Na atoms evaporate from a crucible placed 10 cm below the 2D MOT and heated up to 240 °C. Hot atoms coming out of the oven are captured by the 2D MOT, which is made out of a pair of retro-reflected circularly polarized beams and a set of four stacks of neodymium bar magnets (ECLIPSE N750-RB) used to generate the required quadrupole magnetic field. A resonant push beam aligned along the axial unconfined direction pushes the cooled atoms to the science chamber in the UHV side. The atomic beam loads a three-dimensional magneto-optical trap (3D MOT) with a dark-spot repumper beam (DS), which serves as the first of the cooling and trapping stages leading to condensation. The physical division helps in keeping a clean environment in the science chamber, separating the high pressure side, contaminated by hot atoms coming out from the crucible, from the low pressure environment required to cool the sample to degeneracy.

A red-detuned beam directed from top to bottom towards the atomic oven exploits the magnetic field gradient produced by the tails of the 2D MOT quadrupole to act as an integrated Zeeman slower (ZS) stage, which slows down a large velocity class of atoms below the capture velocity of the 2D MOT. The addition of the ZS beam improves the 2D MOT capture efficiency, increasing the atomic flux to the 3D MOT by more than one order of magnitude. The overall measured loading rate of the 3D MOT reaches 4×10^9 atoms/s. Beams and magnets positions are sketched in Fig. 2.1(b-c).

As shown in Fig. 2.1c, in addition to the ^{23}Na crucible the experiment hosts also a source for ^{39}K that was used for an early stage project on NaK heteronucelar molecules [106]. There is also a source for Sr atoms, which is not used at present.

The experiment is performed in an annealed quartz cell whose size is about $80 \times 60 \times 35$ mm, with 5 mm thick windows. The cell is a polyhedron with two non-parallel faces, to avoid spatial interference between the 3D MOT beams and the flange that connects it to the UHV system, traversed by the loading push beam. The outer surfaces of the four largest windows have an anti-reflection coating, with reflectivity $\sim 0.5\%$ on the spectral range 500 to 1100 nm.

2.1.2 Laser cooling and lasers system

Precise frequency tuning and control of coherent laser radiation is necessary for all stages of optical cooling and manipulation of ultracold atoms.

The main laser source is locked to the cyclic transition on the D2 line $3^2S_{1/2}|F = 2\rangle \rightarrow 3^2P_{3/2}|F' = 3\rangle$ at 589.16 nm which we use for optical cooling. Part of its light is frequency offset to the $|F = 1\rangle \rightarrow |F' = 2\rangle$ transition to serve as a repumper, both in the cooling stage in a dark-spot trapping scheme [107] and to repump the ultracold sample to $|F = 2\rangle$ before imaging it in the last stages of the experiment.

A separate source is locked to the $3^2S_{1/2}|F = 2\rangle \rightarrow 3^2P_{1/2}|F' = 2\rangle$ transition of the D1 line, which is needed for a gray molasses sub-Doppler cooling stage [108].

Both laser sources generate light at the wavelength of 1178 nm, that we amplify and then frequency-double with the use of a resonant doubling cavity. In this way we take

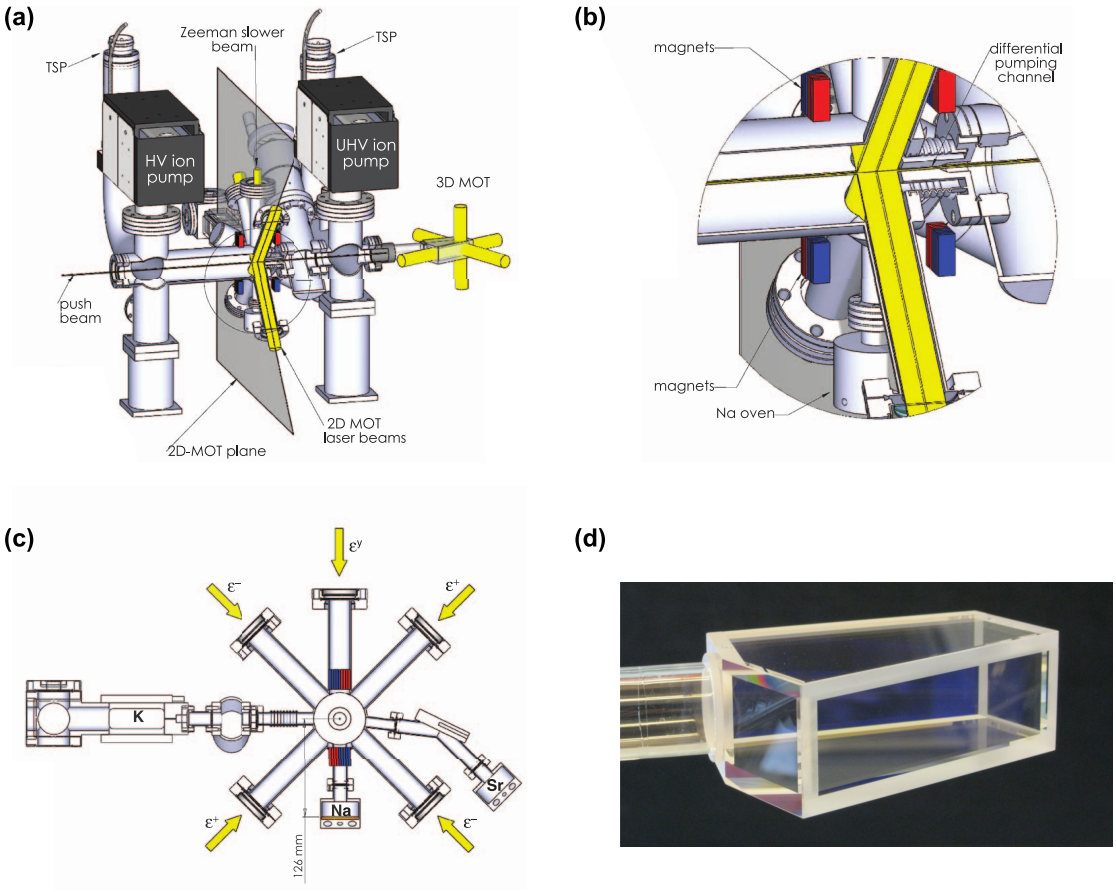

Figure 2.1: (a) 3D view of the vacuum system. HV region on the left side contains the crucibles, sourcing hot atomic vapors, and the optical access for the 2D MOT and push beams. The differential pumping channel connects this to the UHV region where the experiment is performed in a clean environment. Light beams (yellow) and magnets (red-blue) are shown. (b) Magnification of the compact slowing/cooling region. (c) 2D view of the pre-cooling plane showing atomic sources and beams configuration. (d) A picture of the quarz cell constituting the science chamber. Figure adapted from [103]

advantage of the ease of use of diode lasers, which are not directly available in the wavelength range of ^{23}Na transitions.

The two infrared sources are extended cavity diode lasers (ECDLs), where the active medium is a INNOLUME GC-1178-TO-200 gain chip with InAs quantum dots on a GaAs substrate, with anti-reflection coating on the output facet. The D1 source is built in the Littrow configuration [109]: the light of the diode is collimated using an aspheric lens (THORLABS C340TME-C) and sent onto a reflective holographic grating (THORLABS GH13-12V) fixed to a piezoelectric stage. The D2 source uses a cat-eye configuration [110] with an interference filter, which allows for a more mechanically stable configuration. In both sources the coarse wavelength tuning is done using the laser diode current and the temperature, while the piezoelectric stage is used for fine-tuning and locking with a PID. The laser frequency is stabilized by performing frequency-modulated saturated absorption spectroscopy on a Na vapor cell.

The seed light from the master laser is optically amplified with a Raman fiber amplifier (MPB RFA-SF SERIES) pumped with an Yb fiber laser. About 20 to 30 mW of light are injected to the amplifier, which outputs up to 7 W on a single transverse mode, maintaining polarization and spectral properties of the input beam. The amplified infrared radiation is then frequency-doubled by sending it through a resonant bow-tie cavity with a nonlinear LBO optical crystal [111, 112]. At the output of the doubling cavity, about 3.5 W of 589 nm light are available for the experiment.

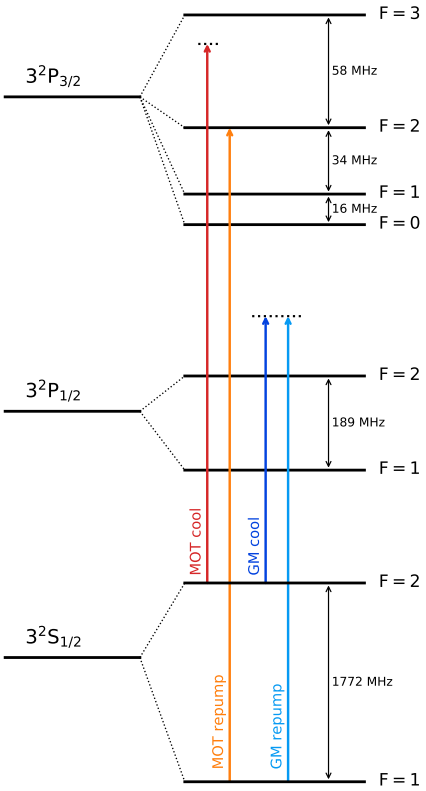

Figure 2.2: Hyperfine level structure of the D1 and D2 lines of ^{23}Na. Arrows correspond to the laser transitions used in the cooling stages: 3D MOT cooler (red) + repumper (orange); gray molasses cooler (blue) + repumper (cyan).

Both laser sources are located on a different optical table than the one of the experiment. The source outputs are split into several branches by combining half-wave plates with polarizing beam splitters (PBS), each independently controlled in terms of power and frequency using RF-driven acousto-optic modulators (AOMs) GOOCH & HOUSEGO and electro-optic modulators (EOMs) QUBIG. A complete scheme of the D2 laser source is shown in Fig. 2.3, where the secondary beams are numbered according to the following description:

(1) *the spectroscopy line*, split in two paths for pump and probe. The pump is offset relatively to the probe by a double-pass AOM which is frequency-modulated. The probe is split again in two beams, only one of which is overlapped with the counterpropagating pump. Both propagate through the Na heatpipe, and the difference in the two absorption signals is measured by a differential photodiode and sent to a lock-in demodulator to compute the error signal fed into a PID. This line locks the laser source to the $2 \rightarrow 3$ transition frequency. The frequency detunings listed below are referenced to this resonant frequency.

(2) *The 3D MOT line*. The combination of the two single-pass AOMs offsets the beam

by -23 MHz and leaves the possibility of further tuning the cooling frequency.

(3) *The atomic source line*, that provides light for the 2D MOT beams at -10 MHz and for the ZS at -300 MHz in double pass. An EOM, set at 1.713 GHz, provides a repumper sideband for both lines.

(4) *The dark spot / repumper line* produces an independent beam tuned to the repumper frequency to be used for the dark spot. This is obtained with a sequence of three double-pass AOMs, the first two driven at +228 MHz and the last one at +400 MHz. The last stage is duplicated to obtain a second beam, which we use as a dedicated repumper for the imaging.

(5) *The probe / push line* output is split in two different beams, one used for the push in the atomic source, operated at +12 MHz detuning, and the other one for resonant probing light. The frequency detuning is switched between the two modes, as they are employed in two distinct phases of the experiment.

Each beam is sent to the experiment table hosting the vacuum chamber through polarization maintaining optical fibers (SCHÄFTER + KIRCHHOFF PMC-630-4.2-NA12-3-APC). Mechanical shutters are placed in front of each fiber input, and are used together with AOMs to block laser light when not needed.

2.1.3 Magnetic fields and RF

We use a set of five water-cooled coils to generate the trapping fields. The coils geometry is sketched in Fig. 2.5, and their axes are labeled according to the reference frame in the figure.

For the 3D MOT we generate the quadrupole field using the vertical pair of coils (cyan) in anti-Helmholtz configuration, which produces a gradient of $1.4\,\mathrm{G\,cm^{-1}\,A^{-1}}$ along z. The conservative magnetic trap, in a Ioffe-Pritchard (IP) configuration, is formed with an additional set of three coils oriented along x, the *pinch* (green) and two compensation (red) coils. The pinch is set such as its gradient term cancels out the quadrupole gradient along x, while the compensation pair, in Helmholtz configuration, reduces the bias term of the pinch field to a few G leaving a shallow quadratic confinement due to the residual field curvature along the axis. We can also generate a levitating magnetic field using only the lower quadrupole coil, which is used to image the atoms after a long TOF (> 20 ms).

The coils are driven by a pair of high power supplies (DELTA ELEKTRONICA SM30-200), which are remotely controlled. Coils are water cooled through pressurized water flowing in the hollow core of the copper wire at 10 bar. All coils are connected in series, hence the current is the same for all of them, suppressing fluctuations in the trap shape due to current imbalance in paired coils. We switch between the different field configurations using high-current insulated-gate bipolar transistors (IGBT) switches (SEMIKRON SKM400GAL12E4) and mechanical relays (KILOVAC EV200). Fig. 2.4 shows the electric circuit powering the coils and the location of the switches. At maximum power we have 200 A flowing in the circuit with a setting time of the order of 10 ms, while the switch-off time for the lower currents (50 A) normally used for BEC trapping is 500 µs, limited by eddy currents.

We have an additional pair of smaller *bias coils* in Helmoltz configuration along each direction. These are used to zero the environmental magnetic field at the center of the trap, which is a required condition for the gray molasses cooling to be effective. The

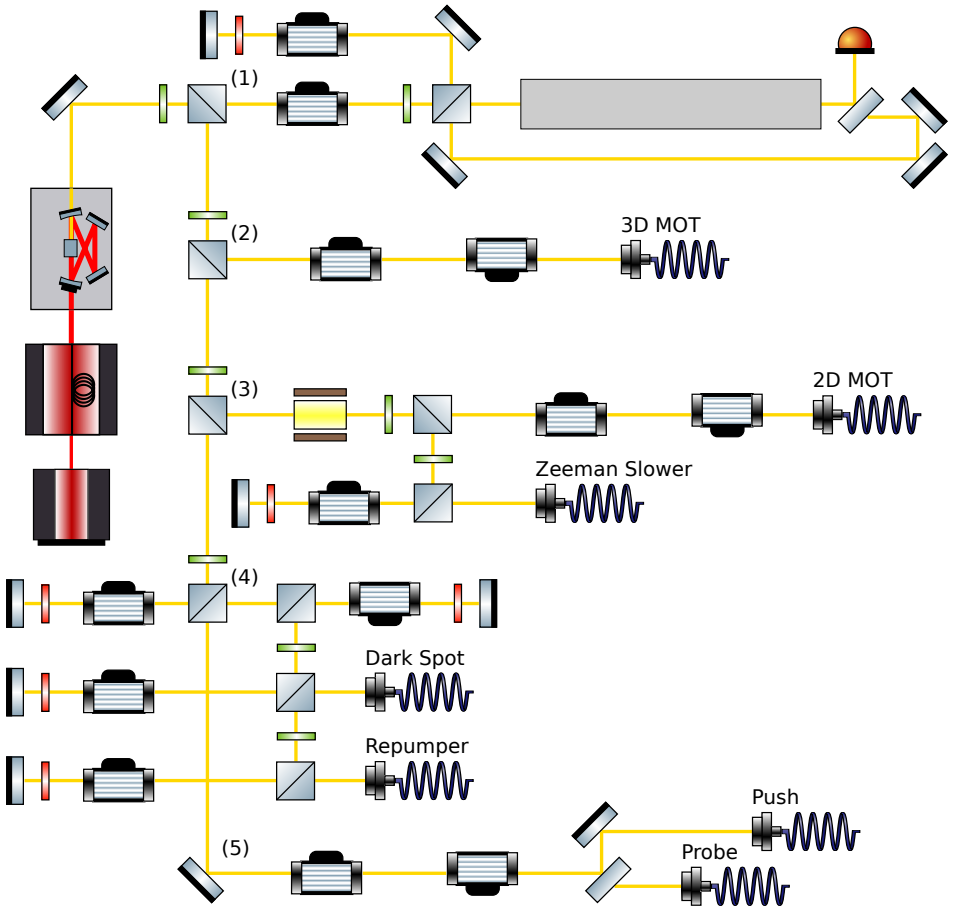

Figure 2.3: Schematic of the optical setup of the D2 laser source, illustrating the position of PBS cubes, half- (green) and quarter- (red) waveplates, AOMs, EOMs and fibers used to actively control the beams, and the spectroscopy line. Numbers list the branches in which we split the main laser line and their use: (1) spectroscopy, (2) 3D MOT, (3) 2D MOT/Zeeman slower, (4) dark spot/repumper, (5) probe/push. This figure is drawn with the use of ComponentLibrary [113], licensed under a Creative Commons Attribution-NonCommercial 3.0 Unported License.

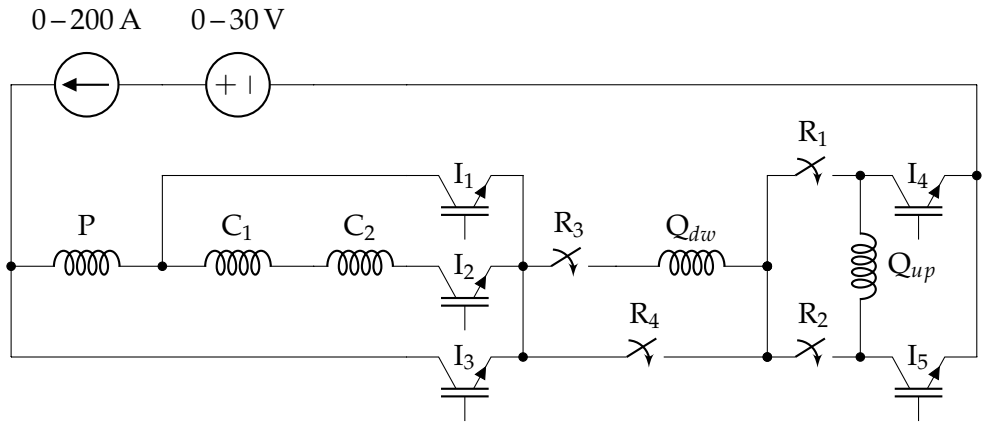

Figure 2.4: Schematic of the electric circuit powering the high-current coils used for the 3D MOT and the magnetic trap. The coils are labeled as: P (pinch), $C_{1,2}$ (compensation), $Q_{up,dw}$ (quadrupole). The switches are labeled as I (IGBTs) and R (relays).

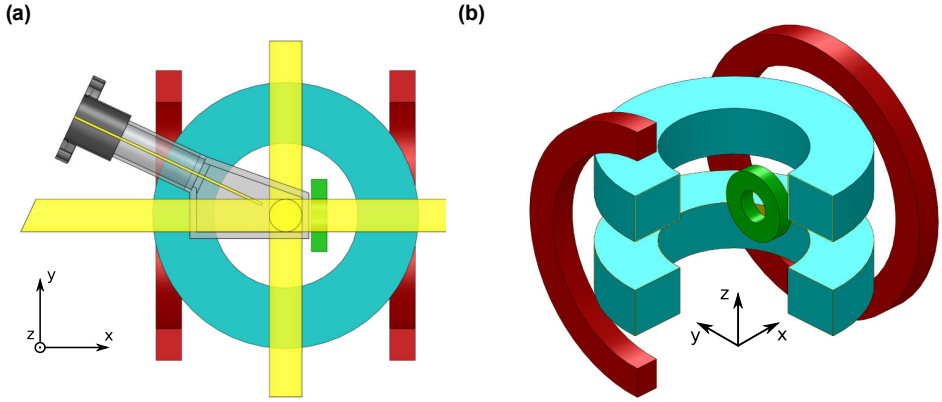

Figure 2.5: (a) Magnetic trap coils positioning around the glass cell: top view from the xy plane. The (lower) quadrupole coil is visible in cyan, the pinch coil in green and the compensations coils in red. The push and the MOT beams are shown in yellow. (b) 3D view of the coils. Figure adapted from [114]

pair along x is also used to finely tune the value of the bias field B_0 in the magnetic trap, which allows to change the trap aspect ratio.

We use wire antennas to deliver RF radiation to the atomic sample. RF signals in the range 50 to 0.5 MHz couple between the Zeeman sublevels of the $F = 1$ manifold. They are generated by DDS boards (Sect. 2.1.4), amplified using MINICIRCUITS ZHL-1-2W-S+ amplifiers, and radiated by the ring-shaped antennas shown in Fig. 2.6. The hook antennas are instead tuned in the microwave range, where we use MARCONI 2040 function generators to produce signals around the ^{23}Na hyperfine splitting frequency 1.7 GHz to couple the $F = 1$ and $F = 2$ hyperfine levels. The vertical distance between the antennas and the atoms is around 17 mm.

2.1.4 Electronics and control

We adopted a hardware control system based on field-programmable gate arrays (FPGAs), developed by Marco Prevedelli and adapted through the years. The central FPGA (XILINX SPARTAN XC3S250E), clocked at 10 MHz, receives a buffered sequence of instructions via USB. Each instruction has a target slave board identified by an address. The FPGA writes the instructions on a 24-bit parallel bus with a time resolution of 100 ns

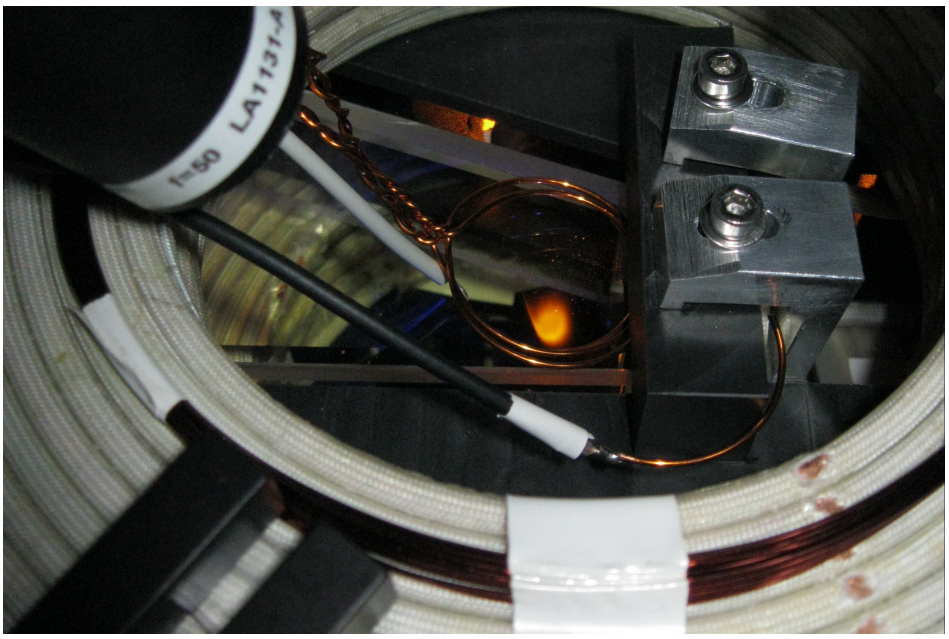

Figure 2.6: Loop and hook wire antennas placed above the quartz cell to deliver RF radiation to the atomic sample. The white windings are part of the upper quadrupole coil Q_{up}, the smaller copper ones are one of the bias coils on the z direction. The tube on the left holds optics to collect fluorescence light from the MOT. The DS-MOT is clearly visible inside the quartz cell.

and at a maximum rate of 2.5 MHz. All the slave boards are connected to the bus, and each board executes the instruction when called for by the corresponding address. The available boards are:

- TTL boards: with 16 channels digital outputs, they are used to trigger timed signals such as IGBT switch on/off, shutters, radio-frequency mixers to control RF and laser pulses, camera exposure;
- Analog boards: these boards have two 16-bit digital-to-analog converter (DAC) chips and can be switched between floating or referred to ground. They are used to control analog parameters such as magnetic field ramps during the RF evaporation;
- DDS boards: RF inputs for the AOMs and the evaporative cooling are generated with direct digital synthesizer (DDS) boards with a ANALOG DEVICES AD9958 dual channel chip. A PIC18F2550 microcontroller programs the DDS reading the parameters from a look-up-table. These devices can be directly commanded by the FPGA to output signals of frequency from 200 kHz to 150 MHz and up to 13 dBm.

Each experiment consists of a timed list of instructions that is executed by the FPGA. This list is compiled by a Python software developed in our laboratory [115] which provides the high-level user interface for the experiment design. The software also sets up other external devices that are not directly controlled by the FPGA, such as the microwave signal generators, and allows to program sequences of experimental runs scanning any of the input parameters.

Data are collected at the end of the experiment, which usually consists in image acquisitions from one or more cameras and triggered oscilloscope signals. All raw data from each experimental run are collected and stored in a single file in HDF5 format,

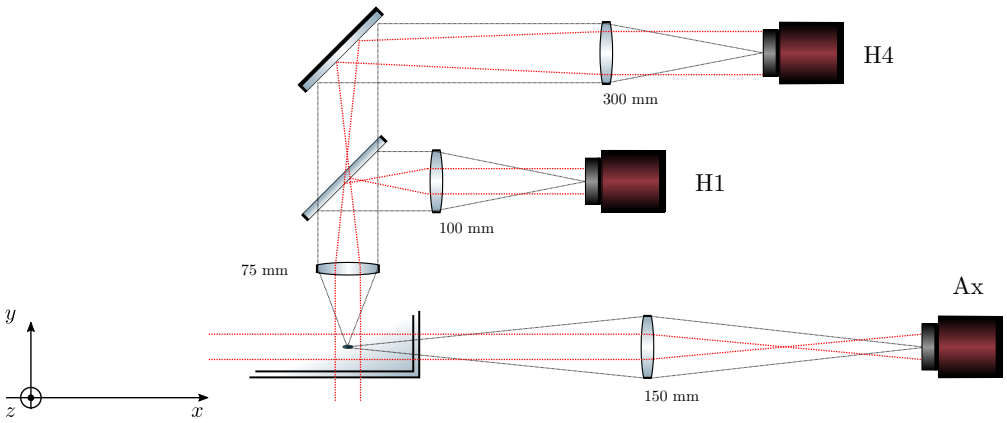

Figure 2.7: Sketch of the imaging system, showing the optical setup of the cameras on the xy plane. Two cameras (H1 and H4) image the y direction, and one (Ax) the x direction. An extra camera (V), placed along z, is not shown. Distances between the optical components are not to scale.

together with a record of the full experimental sequence. For on-line data visualization and analysis we recently adopted the `lyse` tool from the Labscript suite [116].

2.1.5 Imaging setup

The imaging setup in our experiment consists of a total of four cameras. There is one camera along each one of the laboratory axes, allowing to image the atomic sample from every direction, and an extra one is placed along the y axis for in-situ imaging. Fig. 2.7 shows the optical setup, where the cameras are labeled as following:

H1 This camera is placed on the horizontal plane, imaging the atoms along the y direction. The objective is a 75 mm achromat doublet (THORLABS AC254-075-A), placed at a distance $\sim$ 75 mm from the atoms and paired in a telescope to a 100 mm plano-convex lens (THORLABS LA1509-A). The nominal magnification of the system is of 1.33.

H4 This extra camera along y is dedicated to in-situ imaging. It shares the same objective as the H1 and it uses a 300 mm ocular (THORLABS LA1484-A) for a nominal magnification of 4.

Ax The axial camera images the atoms along the x axis of the trap with a 150 mm lens LA1433-A in a $2f$-$2f$ configuration ($M = 1$).

V This camera (not sketched on Fig. 2.7) is placed along the z axis with a 100 mm singlet lens for a demagnified ($M = 1/2$) view of the sample. It is used for characterizing the sample at the dark spot and gray molasses stages through time-of-flight imaging.

All our cameras are STINGRAY F-201, with a 1234 $\times$ 1624 CCD sensor of 4.4 $\times$ 4.4µm pixel size l_{pix}, and communicate using the Firewire IEEE 1394b serial protocol.

2.2 Steps towards condensation

2.2.1 Dark spot MOT

The dark spot MOT (DS-MOT) configuration was introduced as a method to improve the density of magneto-optically trapped atoms [107]. In a standard 3D MOT, atoms are both cooled and trapped by the combined effect of near-resonant light and a magnetic field gradient. The implementation of this mechanism in alkali atoms relies on light tuned close to the $F = 2 \rightarrow F' = 3$ transition, and requires an additional repumper beam to compensate for off-resonant scattering that leads to optical pumping to the $F = 1$ ground state. In this scheme of continuous cooling, density limiting effects are mainly caused by re-absorption of spontaneously emitted photons from within the sample, which gives rise to an effective atom-atom repulsive force. A way to limit this spurious effects is to reduce as much as possible light scattering, especially from the already trapped atoms. In the DS-MOT the 6-axis repumper used in a standard magneto-optical trap is substituted with a hollow-profile beam along one single axis. In this way hot atoms are cooled down in the outer part of the MOT, drift to the center where they are pumped in the $F = 1$ manifold, and accumulate in the central dark region where light scattering is strongly suppressed.

The atoms are loaded in a magnetic field gradient of $16.8\,\mathrm{G\,A^{-1}}$. The hollow beam is produced using an axicon (THORLABS AX252-A). This conic-shaped optical component is designed to convert a collimated beam into a ring, inverting the inner and the outer parts of the beam profile. Sending a collimated Gaussian beam through the axicon we obtain a non-diverging hollow beam with a high light intensity at the border, which is ideal for the geometry of a DS-MOT. Residual light in the central dark region is blocked using a disk-shaped obstacle before imaging such beam profile on the atoms. The radius of the dark region, determined by the optical path of the hollow beam and by the size of the disk obstacle, was experimentally optimized to maximize the number of trapped atoms.

2.2.2 Gray Molasses

Gray molasses (GM) cooling is a sub-Doppler cooling mechanism which combines the physics of polarization-gradient cooling with the presence of coherent dark states. As in ordinary sub-Doppler cooling techniques, atoms are cooled while moving in a polarization lattice and are optically pumped to a lower energy state with reduced scattering probability. In the GM scheme such a state is a coherent dark state, which is not coupled to the laser radiation due to quantum interference effects. This suppresses the coupling with light for the already cooled atoms so that they don't reheat by scattering extra photons. This method cools the atoms down to the fundamental limit of recoil temperature $T_{rec} = \hbar^2 k_L^2 / m k_B$ (where $k_L = 2\pi/\lambda$ is the wavenumber of the cooling light and m is the atomic mass), which for sodium atoms is 2.4 µK.
This mechanism requires blue-detuned light on a $F \rightarrow F' = F$ of $F \rightarrow F' = F - 1$ transition in order to provide cooling, contrary to standard laser cooling methods requiring red-detuned light on a $F =\rightarrow F' = F + 1$ transition. Given the level structure of ^{23}Na the most convenient implementation for this method is using the D1 line, with cooling light tuned to the $|F = 2\rangle \rightarrow |F' = 2\rangle$ optical transition. The advantage of this choice is the absence of higher hyperfine levels in the manifold, preventing off-resonant excitations due to the blue detuning, and the more resolved energy spectrum.

The implementation of such a cooling scheme on the D1 line was demonstrated on sodium atoms for the first time in our experiment [108], characterizing the dependency

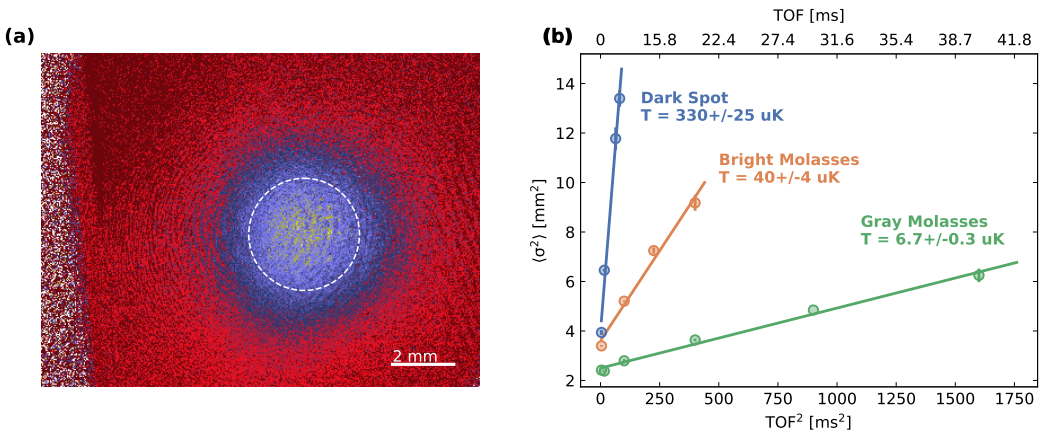

Figure 2.8: (a) TOF picture of the atomic sample after GM cooling and a free expansion of 20 ms, imaged along the vertical direction. The white dashed line marks the r.m.s. of the Gaussian fit. (b) Linear fit tot squared r.m.s. of the atomic sample versus squared TOF, comparing the different cooling schemes: right after the Dark Spot (DS), after standard bright molasses (BM), after gray molasses (GM). The fitted slope is proportional to the temperature, comparing the performance of the different cooling stages: 330(25) nK (DS), 40(4) nK (BM), 6.3(7) nK (GM).

of the final temperature from the experimentally tunable parameters (shape of the cooling pulse, frequency detuning). After installing the DS-MOT axicon setup, we characterized the performance of the GM against the ones of a bright molasses cooling method that was used before, measuring the temperature from the expansion of the r.m.s. size of the sample in TOF. Fig. 2.8 shows a picture of the GM cooled sample after 20 ms of free expansion, and a comparison of temperature measurements in the different cooling stages of the sequence.

2.2.3 Evaporative cooling

After GM cooling the sample needs to be re-captured in the magnetic trap, where RF evaporation is carried out. Loading the cold sample in the IP trap is highly inefficient because the elongated shape of the trap does not match with the one of the distribution, which is roughly spherical. To reduce heating of the sample during the transfer we devised a two-step loading. The atomic cloud is first loaded in a 3D quadrupole gradient at a relatively low current, then the trap is switched to the elongated IP configuration and compressed by ramping up the current to the final value at which evaporation starts.

The evaporation sequence takes up from 30 to 50 s, with RF sweeping from 30 MHz to 730 kHz, which in a trap bottom of about 700 kHz (1 G) corresponds to a final trap depth of $\sim$1.5 µK. The magnetic trap is decompressed at half of the evaporation to avoid three-body losses, to a final shape with trap frequencies $\omega_x = 2\pi \times 8.85(2)$ Hz, $\omega_{y,z} = 2\pi \times 86.6(2)$ Hz. Table 2.1 shows the phase space density (PSD) of the atomic sample and other characteristic parameters through the experimental sequence. With the above described procedure procedure we typically obtain almost pure condensates of 10^6 to 10^7 atoms, with temperatures in the range from 150 to 250 nK. Fig. 2.9 shows a condensed sample, imaged after a 50 ms TOF with magnetic levitation.

Table 2.1: Characterization of the atomic cloud through the experimental sequence, measured at the end of the DS-MOT loading (DS), after GM cooling (GM), after the transfer to the low-current quadrupole trap (QT 50), after the switch to the compressed magnetic trap (MTC) and at the end of the RF evaporation when condensation is reached (BEC). We record the in-situ r.m.s. radius extrapolated from TOF measurements, the temperature, the number of atoms, the capture efficiency (percentage of atoms transferred from the previous stage) and the phase space density.

	r.m.s. radius [mm]	T [µK]	N [$\times 10^9$]	capture	PSD
DS	2.16(5)	290(5)	4.4(2)	-	2.5×10^{-7}
GM	1.87(3)	6.2(5)	3.9(1)	90%	2×10^{-4}
QT 50	1.16(2)	30(2)	1.0(1)	25%	1×10^{-5}
MTC	1.30(1) $\times$ 13.0(1)	30(2)	0.85(5)	85%	8×10^{-7}
BEC	15 $\times$ 150 µm	200(10) nK	2 to 5 $\times 10^6$	–	~ 20

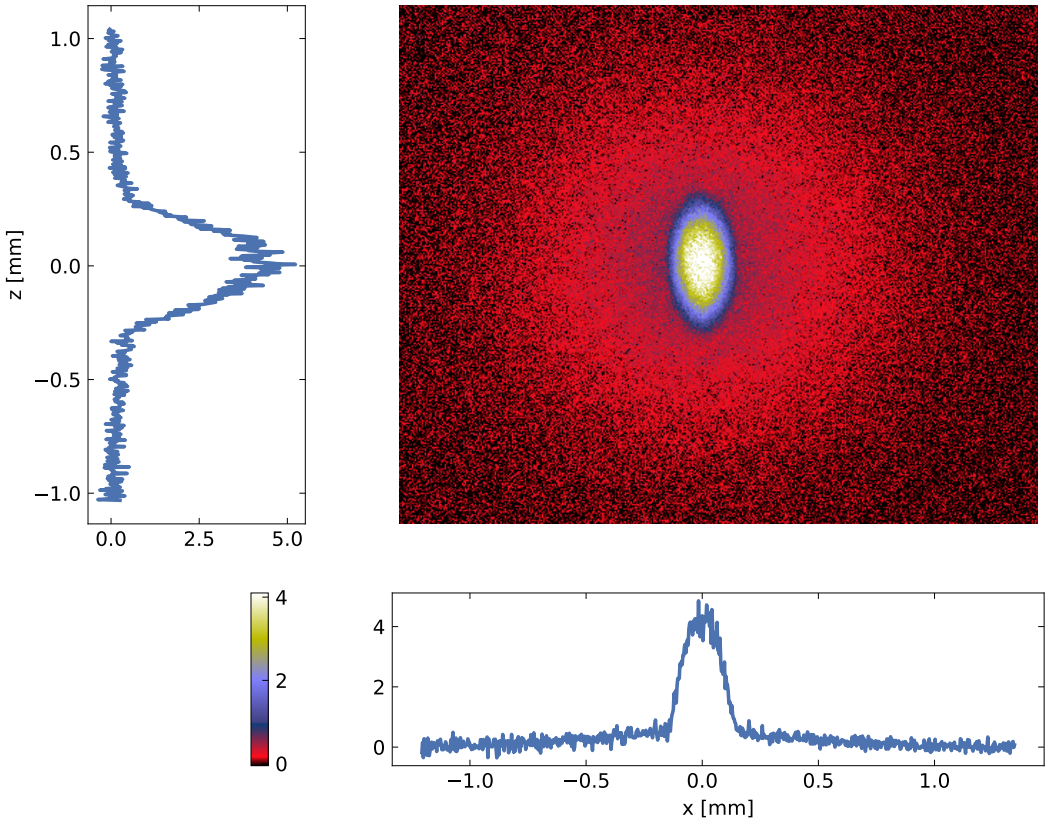

Figure 2.9: Optical density of a condesate of $\sim 5 \times 10^6$ atoms at 250 nK, observed after a 50 ms TOF with magnetic levitation.

Chapter 3

Imaging methods and calibration

Resonant absorption imaging is a common technique used to image atomic samples. It is done by illuminating the atoms with a laser beam, tuned to the frequency of an atomic optical transition, and recording the shadow casted by the atoms on a CCD camera. This measures the transmission coefficient of the atomic medium. Modeling the scattering process allows to relate this quantity to the absolute density of the sample.

In practice, this requires to measure the parameters that determine the process of light scattering in the actual experimental conditions, determined by the probe light intensity, its polarization, and the magnetic field at the position of the atoms. A precise calibration of these parameters was important in our measurements of the equation of state discussed in Chap. 5, since the result depends critically on the knowledge of the absolute density of the imaged sample.

In this chapter I will review the principles of absorption imaging, discuss our choices for the imaging conditions suited to in-situ density measurements for the EoS project, and describe the methods we used to set up and characterize the imaging system.

3.1 Absorption imaging

At the basis of absorption imaging, light is scattered off the atoms in cycles of absorption and spontaneous emission events. After absorbing one photon, each atom re-emits it in a random direction, effectively removing it from the beam. This results in a decrease of the transmitted light intensity as a function of the density of scatterers.

A semiclassical description of light-matter interaction is provided by the optical Bloch equations (OBE) [117, chap. 5], describing both the coherent dynamics of atom-light coupling and the dissipative process due to spontaneous emission. In the simple case of a two-level system interacting with monochromatic light at frequency $\omega/2\pi$, the

time evolution for the atomic density matrix ρ reads

$$\begin{aligned}
\partial_t \rho_{gg} &= \frac{i\Omega}{2}(\rho_{ge} - \rho_{eg}) + \Gamma\rho_{ee}\,, \\
\partial_t \rho_{ee} &= -\frac{i\Omega}{2}(\rho_{ge} - \rho_{eg}) - \Gamma\rho_{ee}\,, \\
\partial_t \rho_{ge} &= -\left(\frac{\Gamma}{2} + i\Delta\right)\rho_{ge} - \frac{i\Omega}{2}(\rho_{ee} - \rho_{gg})\,,
\end{aligned} \tag{3.1}$$

where $\Omega \propto d_{eg}E$ is the Rabi frequency of the coupling between the light electric field E and the electric dipole moment d_{eg} for the transition between the excited state e and ground state g. Γ is the linewidth of the excited state, $\Delta = \omega - \omega_{at}$ is the detuning with respect to the atomic transition at frequency $\omega_{at}/2\pi$, and the rotating wave approximation (RWA) has been carried out, dropping the contribution of off-resonant terms at frequencies $\omega + \omega_{at}$.

In the approximation where the probing time is much longer than $1/\Gamma$, the atoms interact with light in a steady regime, given by the steady-state solution of Eq. 3.1. The average excited state population gives the light scattering rate

$$R_{2\text{lev}} = \Gamma\rho_{ee}(t \to +\infty) = \frac{\Gamma}{2}\frac{s_0}{1 + s_0 + \left(\frac{2\Delta}{\Gamma}\right)^2}\,, \tag{3.2}$$

which depends non linearly on the saturation parameter $s_0 = I/I_{sat}$. Here I is the light intensity and $I_{sat} = \hbar\omega_{at}^3\Gamma/12\pi c^2$ is the saturation intensity for a closed two-level transition.

In the real case of a multilevel atom the OBE should be extended to include all the possible couplings, dependent on the angular momentum structure of the coupled levels and on the light polarization. Their solution describes the dynamics of optical pumping. The scattering rate is given by $R = \Gamma\sum_e \rho_{ee}$, a sum over the steady-state populations of all the excited states.

When the probe light is circularly polarized, it will transfer angular momentum to the atoms until the population is pumped to the stretched states of the ground and excited hyperfine levels, the ones with highest angular momentum. In the steady state the atoms continue to cycle only between the two stretched states, so that the dynamics is effectively the one of a two-level system, and the scattering rate is given by Eq. 3.2. In the $F = 2 \to F = 3$ ^{23}Na line this corresponds to the transition $|2, \pm 2\rangle \to |3, \pm 3\rangle$, and the corresponding value of the saturation intensity is $6.260(2)\,\text{mW/cm}^2$.

When the probe light is linearly polarized and parallel to the axis of the atomic spin (π polarization), the scattering rate takes the form

$$R = \frac{\Gamma}{2}\frac{s_0/\alpha}{1 + s_0/\alpha + \left(\frac{2\Delta}{\Gamma}\right)^2}\,, \tag{3.3}$$

analogous to Eq. 3.2 with the substitution $s_0 \to s_0/\alpha$, where α is a coefficient depending on the steady distribution of the atomic population between the hyperfine sublevels. At zero magnetic field, hence in absence of Zeeman splitting, the coefficient can be calculated analytically and for a $2 \to 3$ transition it takes the value $\alpha = 1.829$ [118].

The above calculated scattering rate is used to describe the process of absorption imaging. In the case of a dilute cloud, neglecting multiple scattering and effects related to atomic motion, the propagation of light in the atomic medium follows the Beer–Lambert law $dI/dz = -\hbar\omega n R$, which defines the rate of change of light intensity along

the propagation direction z as a function of the scattering rate R. Here n is the 3D density of scattering particles along z. Substituting Eq. 3.3, it can be recasted in the form

$$\frac{dI}{dz} = -\sigma_0 n I_{sat} \frac{s_0/\alpha}{1 + s_0/\alpha + \left(\frac{2\Delta}{\Gamma}\right)^2}, \tag{3.4}$$

where $\sigma_0 = \hbar\omega_{at}\Gamma/2I_{sat} = 3\lambda^2/2\pi$ is the resonant value of the absorption cross section for a two-level system, and $\lambda = 2\pi c/\omega_{at}$ is the wavelength at the transition.

Considering resonant light ($\Delta = 0$) we can integrate Eq. 3.4 along z and solve for the optical density

$$OD = \sigma_0 \int_{-\infty}^{+\infty} n\, dz = \alpha \ln\left(\frac{I_{in}}{I_{out}}\right) + \frac{I_{in} - I_{out}}{I_{sat}} \tag{3.5}$$

where $I_{in} = I(z = -\infty)$ is the value of the incident light intensity, before interacting with atoms, and $I_{out} = I(z = +\infty)$ is the transmitted intensity.

Experimentally, we record intensity images as arrays of pixel counts, proportional to the time integral of the light transmitted from a specific location on the object plane during the probing time. After a probing time τ, the count at the pixel (i, j) on the image can be related to the emitted light profile as

$$C_{ij} = \eta G T \int_0^\tau \frac{I(x_i, y_j, t)}{\hbar\omega} \left(\frac{l_{pix}}{M}\right)^2 dt = \chi_{sat} \frac{I(x_i, y_j)}{I_{sat}} \tau, \tag{3.6}$$

where (x_i, y_j) is the location of the object plane imaged on the (i, j) pixel of the sensor, and we considered the emitted intensity as independent on time. The image count depends on the geometry of the imaging system (magnification M, transmission coefficient of the optics T) and the characteristics of the sensor (pixel size l_{pix}, quantum efficiency η, ADC gain G). We normalize the light intensity by I_{sat} and collect all the coefficients in the calibration constant

$$\chi_{sat} = \eta G T \left(\frac{l_{pix}}{M}\right)^2 \frac{I_{sat}}{\hbar\omega}. \tag{3.7}$$

Measuring χ_{sat} allows to calibrate the imaging setup, converting pixel counts in absolute light intensity. This is necessary to compute the density of the atomic sample from Eq. 3.5. In practical absorption imaging we acquire three distinct images:

- *atoms picture*: a picture of the atoms illuminated by resonant light. This gives an image C_{out} which is a time integral of the transmitted intensity I_{out};
- *probe picture*: a picture C_{in} with the same illumination conditions of the previous one, but without atoms. This returns an image of the incident intensity I_{in};
- *background picture*: a picture in the absence of atoms or direct probe light C_{bg}, to measure residual stray light and background illumination on the camera.

For good imaging conditions, the probe picture counts should almost cover the full dynamic range given by the sensor bit depth, and the background picture counts should be almost zero. The optical density of the sample is calculated as

$$OD = \alpha \ln\left(\frac{C_{in} - C_{bg}}{C_{out} - C_{bg}}\right) + \frac{C_{in} - C_{out}}{\chi_{sat}\tau}. \tag{3.8}$$

Fig. 3.1 shows a typical set of experimental images. The top row shows the raw pictures of the atoms, the probe, and the background picture. In the bottom row, the corresponding histograms of the pixel counts.

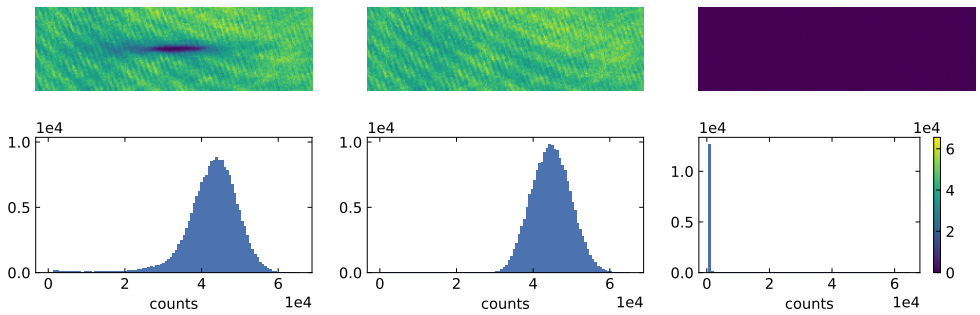

Figure 3.1: Top row, from left to right: atoms, probe, and background raw pictures. These are the direct output of the camera, with counts in the range from 0 to $2^{16} - 1$. Bottom row: histograms of the counts in each corresponding raw picture.

3.1.1 Appropriate probe conditions

As pointed out in a recent work [119], Eq. 3.5 provides a reliable value for the absolute density only neglecting a number of effects in the interaction of the atoms with the probe beam.

Multiple scattering of light can take place in a dense atomic cloud illuminated by resonant light. Corrections to the Beer–Lambert law due to multiple scattering are governed by the parameter $n^{1/3}/k_L$, comparing the length scale of the absorption cross section with interparticle distance. When this parameter is much smaller than 1, the atomic effective cross sections are not overlapping, and the atoms can be regarded as independent scatterers. In our trap geometry the transverse diameter of the (condensed) sample is about 30 µm. An imaged maximum optical density of 3 corresponds then to a peak particle density of order 10^{18} atoms/m^3, which makes $n^{1/3}/k_L = 0.09$. We can then neglect multiple scattering effects in all practical cases of absorption imaging in 3D samples, provided that the imaged optical density is not so high. The phenomenon is instead very relevant in the 2D case [120–122], where the tight transverse confinement results in a higher particle density even for moderate values of the OD.

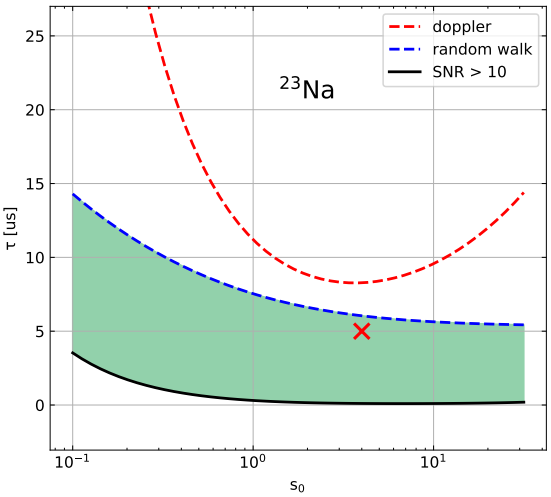

Figure 3.2: Appropriate probe conditions for ^{23}Na absorption imaging. The red cross marks the point $s_0 = 4$, $\tau = 5\,\mu s$ chosen as working conditions for the EoS measurements. Figure inspired from [119] and plotted for ^{23}Na parameters.

Other effects are related to the motion of the atoms during the scattering process, which can be described as a Brownian motion [123, 124]. Scattering cycles result in a linear acceleration along the probe beam direction, causing a Doppler shift, and in diffusion of the velocity causing a diffusion in real space, that will blur the atomic distribution once the r.m.s. displacement in the transverse plane becomes comparable to the resolution of the imaging system.

The approach described in [119] is to find appropriate conditions for the intensity and duration of the probe pulse such as to minimize the side effects listed above. To

limit the loss of resonance from the Doppler effect, we compare the total frequency shift accumulated during the probing time τ with the effective linewidth of the resonance, accounting for the power broadening at high intensities. This leads to the condition

$$2\frac{k_L v_{rec}}{\Gamma} N_{sc}(s,\tau) < \sqrt{1+s}\,, \tag{3.9}$$

where $s = s_0/\alpha$, and $N_{sc}(s,\tau) = (\tau\Gamma/2)s/(1+s)$ is the total number of photons scattered at resonance.

To control the blurring effect of Brownian motion, we want to ensure that the r.m.s. radius δr_{rms} walked by the atoms in the transverse plane during the probing time is smaller than the effective imaged pixel size l_{pix}/M, including the magnification M, so that it cannot be detected. From this consideration we derive

$$\delta r_{rms} = \int_0^\tau \sqrt{\frac{2}{3} v_{rec}^2 N_{sc}(s,t)}\, dt < l_{pix}/M\,. \tag{3.10}$$

As those two conditions alone would push towards short and weak probe pulses, a third one

$$SNR_{OD} = \frac{OD}{\sqrt{\sigma_{OD}^2}} > SNR_{min} \tag{3.11}$$

puts a limit on the signal-to-noise ratio of the measured optical density, considering that the r.m.s. noise σ_{OD} on the optical density originates from the shot noise on the photons counted in each pixel of the CCD during the acquisition of I_{in} and I_{out}.

Fig. 3.2 shows the range of probe conditions suitable for imaging ^{23}Na, that is the region of parameters (s_0, τ) where the three above inequalities are satisfied at a threshold $SNR_{min} = 10$, considering an imaging magnification of 4 and linearly polarized probe light at low magnetic field, so that α has a value close to 2.

3.2 Characterization of the imaging system

3.2.1 Fast imaging

The use of Eq. 3.8 would require measuring simultaneously both the incident and the transmitted probe light, which is not possible. In practice, the probe and the atoms picture are taken at two different times, and we assume to image in the first one the same light beam that actually hits the atomic sample in the second one. Differences in the two pictures other than absorption from the atomic sample will show up as a spurious OD signal, spoiling the measurement of the density profile.

One of the most common issues is the presence of fringes. Interference fringes arise from multiple reflections of the probe beam in the path traveled to reach the camera. Mechanical vibrations of the optical system randomly shift the phase of the interference figure, resulting in different intensity patterns in the two pictures.

It is possible to compensate for these errors with image processing techniques, such as Fourier filtering or the eigenfaces method [125], but a way to strongly suppress the presence of fringes is to reduce as much as possible the time between the two light pulses. As the typical frequency scale of mechanical vibrations is in the kHz, the time delay needs to be on the order of 100 µs to avoid variations in the optical path.

We achieved this with the imaging sequence sketched in Fig. 3.3. As our camera mounts an *interline transfer* CCD sensor, it allows to trigger a second acquisition while another frame is being read out with a minimum delay of about 20 µs, although the

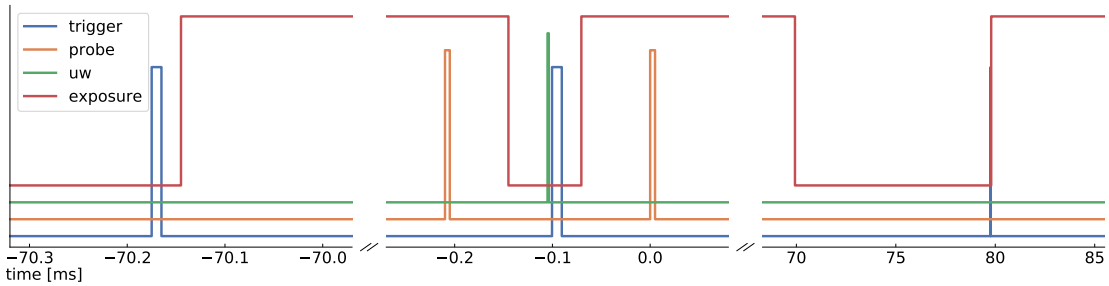

Figure 3.3: Time sequence for fast imaging. The traces are TTL signals sent (trigger, probe, uw) or acquired (exposure) during an imaging sequence. The camera exposure, whose length is set to 70 ms, starts after a trigger signal is sent to the camera. The first probe pulse is sent at the end of the first frame exposure, then a microwave pulse flips a fraction of the atoms to the $F = 2$ hyperfine levels, and they are imaged by a second probe pulse sent at the beginning of the exposure of the second frame. The background picture is acquired at the end of the sequence.

exposure time for each picture can be of 10 to 100 ms depending on the size of the imaged area [126].

At the end of the preparation, the atoms are trapped in the $|F = 1, m_F = -1\rangle$ state, and need to be transferred to $F = 2$ to be resonant with probe light. The probe picture is acquired first, while the atoms are still far out of resonance and will not scatter light from the beam, shining light at the end of the exposure. After the acquisition is finished, we pump the atoms to the resonant state with either a laser beam or microwave radiation, and then we take the atoms picture, shining light at the beginning of the second exposure. The background picture is acquired much later, at the end of the experimental sequence. In this way we were able to reduce the delay between the first and second probe pulse to 200 µs.

3.2.2 Magnification

A standard way to measure the magnification of an imaging system which looks at the atoms along a horizontal direction consists in measuring the distance the atoms travel while freely falling under the effect of gravity only.

To suppress the effect of stray magnetic field gradients we use atoms in $m_F = 0$, as they are at first order insensitive to magnetic forces. We also need to switch off the magnetic trap after transferring the atoms, as the field strength increases rapidly far away from the trap center and the second-order Zeeman shift becomes non negligible (it would exert on a $m_F = 0$ atom an acceleration of $2\,\mathrm{m/s^2}$ after a 2 mm fall).

After preparing the condensed sample in $|F = 1, m_F = -1\rangle$ we transfer 10% of it to the non-magnetic state $|F = 2, m_F = 0\rangle$ with a microwave pulse, let it fall for 2 ms to separate it from the trapped fraction, then switch off the magnetic trap and let the two clouds fall together. We measure the imaging magnification M from the trajectory of the $m_F = 0$ atoms. The measured values are 1.38(5) for the H1 camera, and 4.02(7) for the H4 camera, in good agreement with the nominal values 1.3 and 4 calculated from the geometry and the focal lengths of the optics system, reported in Fig. 2.7.

From the difference in the acceleration measured on the two clouds we can evaluate the strength of environmental magnetic field gradients, that are present even long after the magnetic trap has been switched off, estimated to $\sim 0.16\,\mathrm{G/cm}$.

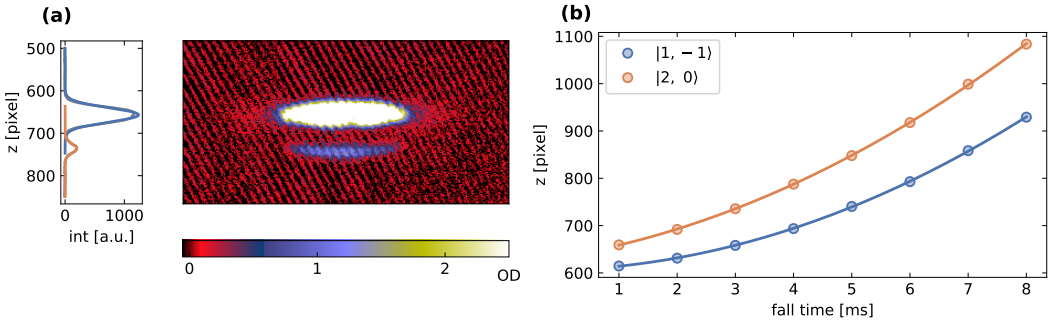

Figure 3.4: (a) Image of the two of free-falling clouds on the H4 camera. On the left, the image is integrated along the rows, and Gaussian fits are used to measure the vertical position of each cloud. (b) Parabolic fit to the position of the clouds as a function of the fall time.

3.2.3 Focusing

In the regimes of weak probe intensity ($s_0 \ll 1$) or far-detuned light ($\delta = 2\Delta/\Gamma \gg 1$) the atomic response to light is linear, and can be interpreted in terms of a refractive index dependent on the atomic density n [127, 128]

$$n_{ref} = 1 + \frac{\sigma_0 \lambda n}{4\pi} \left(\frac{i}{1+\delta^2} - \frac{\delta}{1+\delta^2} \right) . \tag{3.12}$$

In the far detuned case we can neglect the imaginary part in n_{ref} (which is responsible for the absorption), so that after passing through the cloud the probe beam acquires a phase factor $e^{i\phi}$ with argument proportional to the integrated column density,

$$\phi = \frac{2\pi}{\lambda} \int \mathrm{Re}(n_{ref} - 1)\, dz = \frac{\sigma_0}{2} \frac{\delta}{1+\delta^2} \int n\, dz\,. \tag{3.13}$$

Assuming a flat probe intensity, after propagating for a distance D the phase-shifted light produces an intensity profile

$$I_D = I_0 \left[1 - \frac{\lambda D}{2\pi} \nabla^2 \phi \right] . \tag{3.14}$$

This signal, proportional to the second derivative of the column density, can actually be used to image the atoms in a dispersive imaging technique called *shadowgraph imaging* [129]. As shown by Eq. 3.14, the contrast of the signal is proportional to the distance between the plane of the atoms and the object plane which is imaged by the optics on the camera sensor.

We used instead the diffractive signal to focus the camera, exploiting the fact that it is cancelled only when the atoms are imaged precisely on focus. Focusing the optical system is critical for in-situ imaging, as imaging out-of-focus results in a blurred picture with reduced resolution. Moreover, an optical signal from non-resonant atoms would spoil the fast imaging method, as the probe picture would display the shadowgraph image instead of the probe intensity pattern only.

Starting from a condensed sample in $|F = 1, m_F = -1\rangle$ we take four in-situ images of the BEC while scanning the camera position. First a picture of the $F = 1$ atoms, which is showing the dispersive intensity pattern; then we transfer a small fraction the sample to $F = 2$ ($\sim 1\%$), to avoid OD saturation, and take an absorption image of the resonant atoms. After releasing the atoms from the trap we take a reference picture of the probe beam only, and later on the background one.

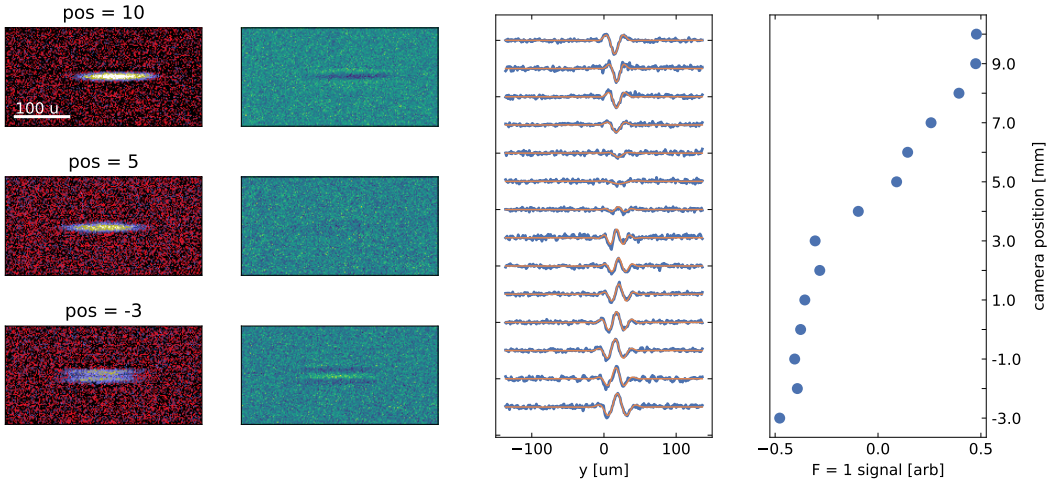

Figure 3.6: From left to right: resonant OD of $F = 2$ atoms (first column) and shadowgraph optical signal of $F = 1$ atoms (second column) at three different camera positions. Third column: integral along the rows of the shadowgraph signal, fitted with a Gaussian function. Fourth column: fitted amplitude as a function of the camera position. The camera is on focus at the point where the amplitude is zero.

We extract the dispersive signal from the first image by subtracting the probe picture and integrating along the rows to enhance the contrast, and we fit it to the function $A(x^2 - 1)e^{-x^2/2\sigma^2}$ (second derivative of a Gaussian). At each position, we also compute the OD of the $F = 2$ atoms from the second and third pictures. Fig. 3.6 shows the shadowgraph and OD images for some camera positions, the diffractive signals with Gaussian fits across the position scan, and a plot of the fitted amplitude as a function of the camera position.

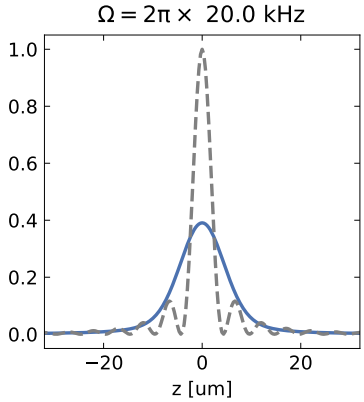

Figure 3.5: Microwave π-pulse at a Rabi frequency $\Omega = 2\pi \times 20\,\mathrm{kHz}$, in a vertical magnetic field gradient of 34 $\mathrm{G\,cm^{-1}}$. Dashed line: transition profile along z. The r.m.s. width of the resonance peak is of 1.6 µm. Solid line: the same profile is blurred by convolving it with a Gaussian of $\sigma = 4\,\mu\mathrm{m}$, resulting in a larger width of 5 µm.

As the shadowgraph signal goes from positive to negative amplitude, the optical density of the resonant $F = 2$ atoms loses the side lobes which are characteristics of out-of-focus imaging, and the point of focus is where the shadowgraph signal goes to zero. With this method we were able to put the H4 camera on focus with sub-millimeter precision and to eliminate the spurious signal from in-situ OD measurements.

3.2.4 Imaging resolution

To measure resolution we image a small slice of the atomic sample, repumping the atoms with a spatially-selective microwave transition.

We release a dilute cloud of thermal atoms in a strong vertical magnetic field gradient, produced using the lower quadrupole coil, send a microwave pulse to transfer atoms to the $F = 2$, and image the transferred atoms. Only a thin slice of the cloud lying on a horizontal plane determined by the microwave frequency will be resonant, and the width of the resonance is determined by the field gradient and the Rabi frequency of the coupling.

Scanning the microwave frequency, we find a reso-

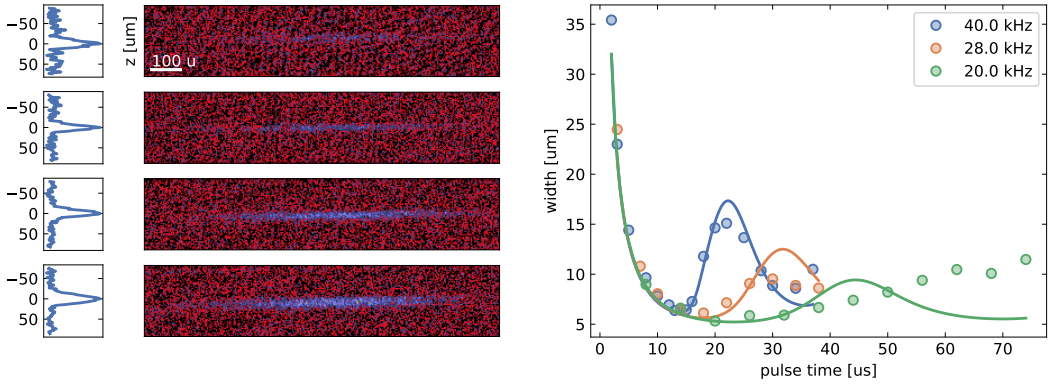

Figure 3.7: Left: images of the sliced atomic distribution, for a Rabi frequency $\Omega = 2\pi \times 20\,\mathrm{kHz}$ and pulse times of 14, 20, 38, 50 µs, with integrals along the rows. Right: The dots are the width of the atomic slice, measured with a Gaussian fit on the row-integrated image, as a function of the microwave pulse time for three different Rabi frequencies. The solid lines show the simulated width, calculated using a Gaussian PSF of 4 µm r.m.s.

nance at the position of the atomic sample at a frequency of 1371.6 MHz. Considering the second order Zeeman shift, this corresponds to a transition $|1,-1\rangle \rightarrow |2,-2\rangle$ in a field of 210 G, in agreement with the value predicted from the coil design at the given current. The same model gives a field gradient of $34\,\mathrm{G\,cm^{-1}}$ along z. We integrate the OD along the rows, fit with a Gaussian, and plot the fitted width as a function of the Rabi pulse time. The measurement is repeated lowering the microwave power, hence reducing the microwave Rabi frequency and the width of the resonance feature, until the smallest width we can observe is not varying anymore.

As the field gradient and the Rabi frequency are known, we compute the resonance profile in space, convolve it with a Gaussian modeling the optical PSF, and fit it again with a Gaussian function to measure its size, thus simulating the result of our measurements. For the dataset with the smallest Rabi frequency (20 kHz), the true width of the atomic slice would have a minimum at 1.6 µm, shown in Fig. 3.5.

We measure the width of the PSF in our optical system as the value at which the simulated curve matches with the data. We obtain a good match for all the measured datasets with a value of the PSF width of 4 µm.

3.2.5 Calibration of absorption imaging

To complete the calibration of the optical system for absorption imaging, we need to measure the two coefficients α and χ_{sat} required in Eq. 3.8. The two have a different physical origin, since the former depends on the dynamics of light scattering in the atomic cloud, while the latter depends only on technical characteristics of the imaging setup.

Calibration of the probe intensity: χ_{sat}

We measure the intensity of the probe beam at the plane of the atoms, and compare it to the pixel counts obtained imaging the same beam on the camera. We sample part of the probe beam, send it onto a photodiode, and measure the beam power just before the glass cell with a calibrated power meter THORLABS S130C (Fig. 2.7). The value read on the power meter needs to be corrected by the transmission coefficient of the first window of the glass cell, which is measured to be 0.96(1), to measure the light power P hitting

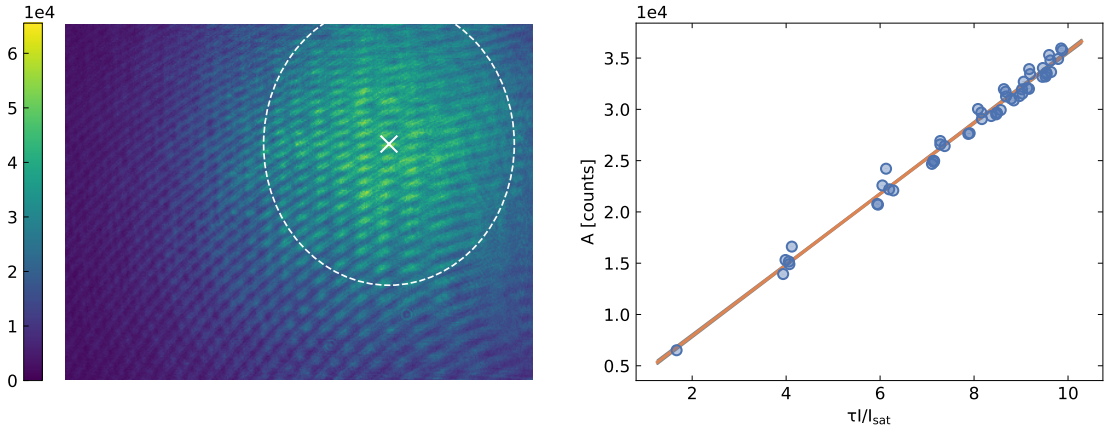

Figure 3.8: Left: a raw image of the probe beam with Gaussian fit. The dashed circle marks the beam waist. Right: peak intensity value in pixel counts A vs. $s_0\tau$. The slope of the fitted line gives the value of χ_{sat}

the atoms. We calibrate the voltage reading of the photodiode to directly measure P, then we remove it to let the beam pass through the glass cell and reach the camera.

The low-magnification camera H1 has a wide field of view, and it sees the whole Gaussian profile of the light. We take pictures of the beam using the H1 camera, scanning the probe power at fixed pulse time τ. The beam power is measured in-shot from the photodiode signal, while the picture is fitted with a Gaussian function $Ae^{-2x^2/w_x^2-2y^2/w_y^2}$ to measure the beam waists w_x, w_y. The fit amplitude A is a measure of the peak intensity of the beam at the plane of the atoms in units of pixel counts, and is related using Eq. 3.6 to the measured power by

$$A = \chi_{sat} s_0 \tau = \chi_{sat} \frac{2P}{\pi w_x w_y I_{sat}} \tau \tag{3.15}$$

A linear fit of A vs. the product $s_0\tau$ gives a value $\chi_{sat}^{H1} = 3462(38)$ counts μs^{-1}. Fig. 3.8 shows a picture of the probe beam and the fitted data.

We repeat the same procedure for the second camera H4. This time the field of view is too small to capture the Gaussian shape of the beam, but yet not small enough to consider the light profile as homogeneous on the whole sensor. Since we know already the geometry of the beam from the former calibration, we use the previously measured magnifications to fix the position and the size of the Gaussian beam on the new field of view, taking as absolute reference the in-situ position of an atomic cloud as seen by both cameras. Leaving the amplitude A as the only fitting parameter we repeat the above procedure, and obtain the coefficient $\chi_{sat}^{H4} = 1950(5)$ counts μs^{-1}.

Calibration of the absorption cross section: α

We measure α using two different methods, both based on the principle that the optical density of an imaged atomic cloud, which appears on the left-hand side of Eq. 3.8, only depends on the optical properties of the atomic sample and not on the intensity of probe light, which instead the two pictures C_{in} and C_{out} depend on.

An alternative calibration method found in the literature consists in measuring the recoil imparted on the atoms by the probe beam. This allows to calculate the light scattering rate as a function of the probe intensity, determining the product $\alpha\chi_{sat}$ [131]. As the EoS measurements required to image the atoms while still holding them in

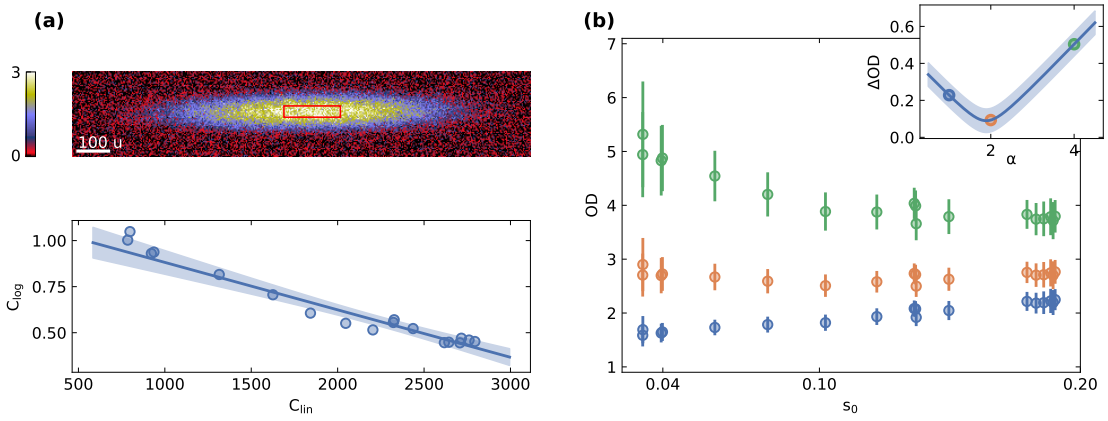

Figure 3.9: Calibration of α. (a) Method by Horikoshi et al. Top: a picture of the atomic sample, showing the location of the ROI used in the calibration. The OD in this picture is calculated using $\alpha = 2$. Bottom: Linear fit of C_{log} vs. C_{lin}, which gives $\alpha = 2.0(4)$. (b) Method by Reinaudi et al. Main: OD of the same atomic sample at different s_0, calculated for $\alpha = 1, 2, 4$. Inset: ΔOD vs. α, minimized at $\alpha = 1.9(4)$.

the magnetic trap, we could not use this calibration method, as the trapping field would interfere with the motion of the sample after the probing and spoil the recoil measurement.

We take a sequence of in-situ images of a dilute thermal cloud with the H4 camera while scanning the probe intensity over a broad range. Following the method described in Horikoshi et al. [119], we define the quantities $C_{log} = \ln((C_{in} - C_{bg})/(C_{out} - C_{bg}))$ and $C_{lin} = (C_{in} - C_{out})/\tau$. These are related to the optical density through Eq. 3.8, which can be rewritten as

$$C_{log} = \frac{OD}{\alpha} - \frac{1}{\alpha \chi_{sat}} C_{lin} \,. \tag{3.16}$$

For each image in the dataset, we consider a region of interest (ROI) in the center of the cloud, smaller than the r.m.s. of the sample such that the density can be considered as constant, and calculate C_{log} and C_{lin} averaging over the ROI. The ratio OD/α is unknown, but constant for each point. A linear fit of C_{log} vs. C_{lin} returns the product $\alpha\chi_{sat}$, which divided by χ_{sat}^{H4} that we previously measured leads to $\alpha = 2.0(4)$.

We analyzed the same dataset with another method, reported in Reinaudi et al. [130]. We compute the OD in the central ROI in each picture using Eq. 3.8 and the value of χ_{sat}^{H4}, leaving α as a free parameter. The correct value is the one that minimizes $\Delta OD(\alpha)$, the standard deviation of the OD over the dataset. Fig. 3.9b shows in the inset the quantity ΔOD vs. α, which is minimized for $\alpha = 1.9(4)$. In the main panel we plot the OD of the data at different s_0 calculated using selected values of α, showing that it becomes constant for α close to 2.

The result of Eq. 3.3 for the scattering rate, which Eq. 3.8 depends on, is demonstrated valid only for linearly polarized light and at zero magnetic field, which means that the levels are not split by the Zeeman effect [118]. This is not our case, as we are working in a magnetic trap. To estimate the influence of the finite Zeeman splitting, I calculated the scattering rate for arbitrary magnetic field and light polarization with a numerical integration of the OBE, using the Python package `qutip` [132]. The technical details are explained in Appendix A.

From the scattering rate we obtain the theoretical value of α as a function of the magnetic field B. For a linear polarization of the probe light, the results agree with Eq. 3.3 with a weak quadratic dependency of α from the magnetic field. At $B = 0$ we retrieved

the analytical result $\alpha = 1.829$. Comparing the simulations with the experimental imaging calibration, the measured α is compatible with the value calculated at $B = 1\,\mathrm{G}$ within errors.

Chapter 4

Observation of vortex filaments in expanding BECs

The physics of quantized vortices in superfluid systems is an actively investigated topic, as it represents one of their most striking and characteristic features. In atomic BECs, the Gross–Pitaevskii equation analytically describes the shape of these defects in homogeneous systems, and provides a solid and accurate background for the study of trapped samples, as the ones available in a laboratory.

There is still however no direct quantitative comparison between theory and experiment for the structure of the vortex core in three-dimensional condensates. A reason for that is that the direct in-situ observation of these defects is challenging, as their typical length scale is much smaller than the resolution of standard optical imaging methods. A possible solution is to release the condensate from the trap and observe it after a suitable time of flight, letting the vortex expand and become visible with optical imaging methods [29, 57].

In this work, we observed 3D vortex filaments after a TOF expansion with enough accuracy to allow for a direct comparison with the predictions of the GP theory. Numerical GP simulations provide results for both the in-situ shape and the expansion dynamics of such defects, and using scaling laws which are valid in the limit of large condensates we compare them with with our experimental observations, and find good agreement. In the first part of this chapter I will outline the setup and the results of GPE simulations, which have been done by our collaborators in the theoretical group. Then I will describe the experimental measurements and the analysis procedure, which I developed and applied to both the simulation results and the experimental data, and discuss the results.

4.1 Numerical simulations

A typical GPE simulation outputs snapshots of the condensate wavefunction through its time evolution, from which one can compute density profiles to compare with

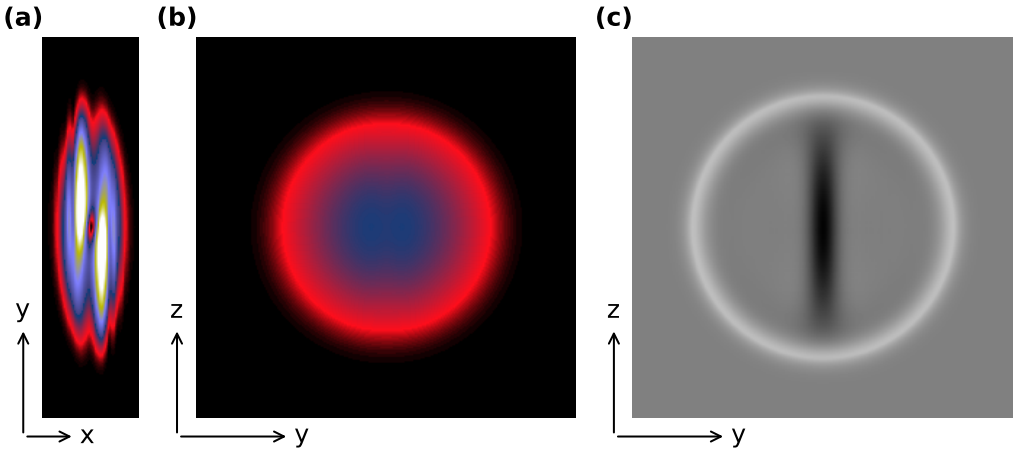

Figure 4.1: Snapshots of GPE simulations, showing the column-integrated radial (a) and axial (b) density profiles absorption images of a condensate with $\tilde{\mu} = 9.7$ atoms after a free expansion evolution time of $\tau = 73$ (120 ms). (c) Residual of the TF fit of the axial density profile, showing the vortex density dip.

experimental images. Having access to both density and phase at once, and with spatial and temporal resolution limited only by computational resources (which is by the way a rather strong constraint), simulations give a great amount of information on the physical system under investigation. The results are in any case limited to the scope of GP theory, and they still need to be checked against real-life observations. Nonetheless numerics and experiments fruitfully complement each other, leading together to a complete and better understanding of the physics behind condensed systems.

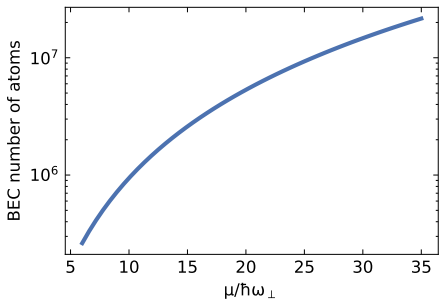

Figure 4.2: Number of condensed atoms vs. chemical potential $\mu/\hbar\omega_\perp$

In this work we used the GPE (Eq. 1.3) to study weakly-interacting trapped condensates hosting a vortex, and to and simulate the evolution of the atomic density during a free expansion of the BEC. The parameters of the simulation are the same as in the experiment: the interaction coupling constant is set by the scattering length $a = 54.54\, a_B$ (in units of the Bohr radius a_B) [133], and the trapping geometry is a cigar-shape harmonic potential of frequencies $\omega_x = 2\pi \times 9.3$ Hz and $\omega_\perp = 2\pi \times 93$ Hz. The number of atoms is adjusted by the chemical potential $\tilde{\mu} = \mu/\hbar\omega_\perp$, in units of the transverse harmonic oscillator energy (Fig. 4.2).

A vortex line is phase-imprinted in the center of the condensate along the z axis, and the in-situ density profile is computed by propagating the GPE in imaginary time. The solution is used as the starting condition for a real-time evolution with $V_{ext} = 0$, simulating the free expansion after the release from the trap. The evolution time is measured in units of the transverse trapping frequency as $\tau = \omega_\perp t$. Fig. 4.1(a-b) show integrated column densities along two orthogonal axes for a simulated BEC with $\tilde{\mu} = 9.7$ after an expansion time $\tau = 73$ (120 ms).

The requirements for such a simulation are demanding: the computational volume needs to be suitably bigger than the sample to avoid non-physical self-interference effects due to boundary conditions, and the grid must be fine enough to capture the length scale of the defect. With the above constraints the number of grid points scales with the size of the object as $\tilde{\mu}^3$, which limits the feasibility of simulating large-number condensates.

For this reason we could run simulations only for condensates with chemical potential $\tilde{\mu}$ from 7 to 12, corresponding to an atom number of 3×10^5 to 1×10^6.

4.2 Experiment

Vortices are naturally produced in the experiment while crossing the phase transition, as a result of the Kible–Zurek mechanism [47]. Due to the stochastic nature of the process, both their number and position are random at each experimental shot. The average number of vortices depends on the quench rate at the transition point, which is however limited by atom losses. Rapid quench rates introduce more vortices but reduce the atom number to the point where it is not possible to achieve condensation.

We can tune the average vortex number with the cooling rate at the transition point. By adjusting the number of atoms loaded in the 3D MOT and the RF sweeping rate of the final part of the evaporation, we obtain samples with 2×10^6 to 20×10^6 atoms ($\tilde{\mu}$ from 15 to 35), with one vortex on average, and negligible thermal component.

The elongated geometry of the trap ensures that vortices align on a radial plane, perpendicular to the weak axis of the trap. This allows to have a 3D visualization of the vortex density distribution by imaging the BEC along two orthogonal axes. We take two simultaneous absorption images after a long TOF, one along the x direction (axial image) and one along the y direction (radial image), as sketched in Fig. 4.3. The TOF is chosen in the range from 100 to 150 ms, to let the optical density decrease below a value of 2 on both images. For such a long TOF we employ magnetic levitation, otherwise the BEC would fall out of the field of view of the camera, setting a current of about 10 A in the lower quadrupole coil only.

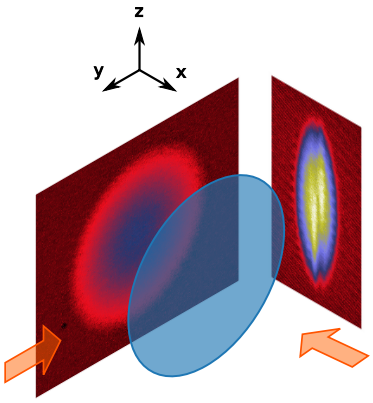

Figure 4.3: Sketch of the TOF imaging of a BEC with a vortex

The two images together reveal the three-dimensional structure of the vortex. On the radial image we can see the planar density depletion characteristic of the solitonic nature of this defect, with a central dip corresponding to the nodal line and an S-shaped twist in the cases when the vortex core is aligned with the imaging direction, as the one shown in Fig. 4.4a. In the axial image of Fig. 4.4b the planar depletion is integrated out by the imaging process, and the vortex filament structure is visible as a linear dip on top of the Thomas–Fermi density distribution.

4.3 Data analysis

The analytical results provided by Thomas–Fermi approximation for the in-situ shape of the trapped BEC (Eq. 1.7) and the by the Castin–Dum dynamical equations for the free expansion (Eq. 1.14) are the starting point of our analysis. A set of GPE simulations without vortices are fitted with TF profiles at all expansion times, checking that the inverted parabola is a very good approximation of the GP profile even for the lowest simulated atom number. The time evolution of the TF radii during expansion is found to agree very well with the analytical solution of Eq. 1.14. Motivated by these results, we use the TF profile as a fitting function to measure the peak density and radii of the expanding condensate even in presence of the vortex.

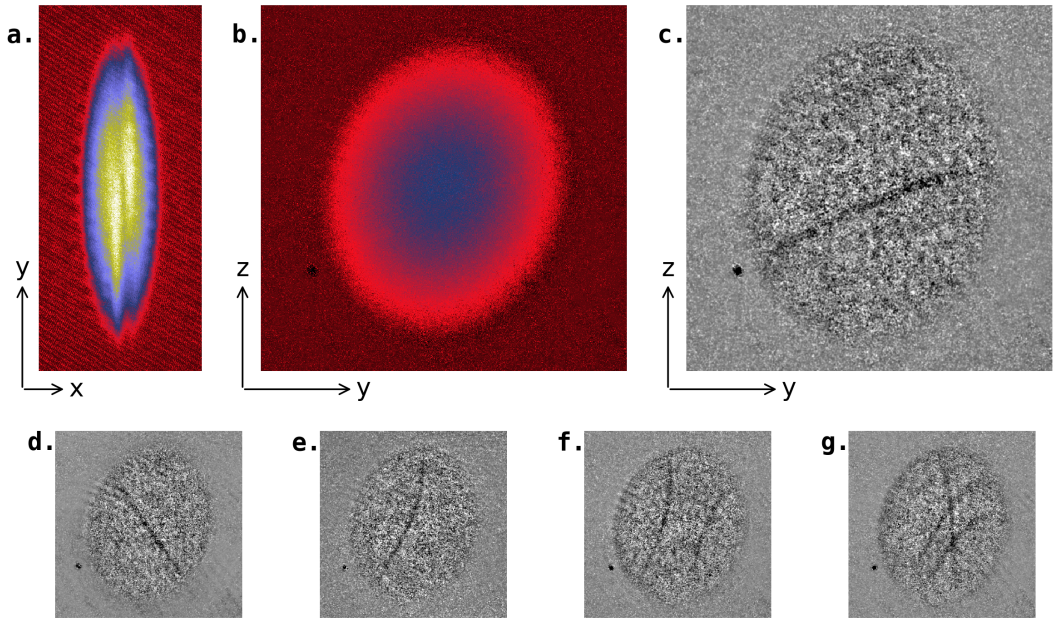

Figure 4.4: Radial (a) and axial (b) absorption images of a condensate with 7×10^6 atoms after 120 ms of free expansion, showing the twisted density depletion on the radial plane of the defect and the vortex nodal line. (c) Residual column density, obtained by cleaning the OD from optical interference fringes and subtracting the Thomas–Fermi fit. The result is an image of the residual column density which neatly reveals a vortex filament. (d)-(g) Other examples of vortex filaments shown by the residual column density for different condensates with one or more vortices. Figure adapted from [59].

The data analysis methods presented in this section will be consistently used to analyze both the simulated profiles and the experimental images. The two datasets remarkably complete each other, because while the simulations allow to follow the full time evolution of the expansion, the experiment provides single-TOF data in a range of chemical potential which is totally out of reach from the simulations due to our computational constraints.

We integrate the GPE density profile along the x direction to obtain a image of the BEC axial column density (Fig. 4.1b), which is the quantity that will be measured in the experiment. We fit it to an integrated TF profile

$$n_{TF}^{col} = n_{TF}^{col}(0)\left(1 - \frac{y^2}{R_y^2} - \frac{z^2}{R_z^2}\right)^{3/2}, \tag{4.1}$$

where we fix $R_y = R_z = R_{TF}$, as the simulated condensate expands symmetrically on the yz plane. We subtract the fit from the column density to reveal the shape of the vortex, that appears as a negative dip in the fit residuals. Fig. 4.1c shows an example of such a residual image. The fit provides the values of the transverse TF radius R_{TF} and of the peak column density $n_{TF}^{col}(0)$ at evolution time τ, that we use as normalization scales: we define the normalized coordinates $\tilde{y}$ and $\tilde{z}$ as y/R_{TF} and z/R_{TF} respectively, and rescale the residual image by the value of $n_{TF}^{col}(0)$.

We extract a 1D vortex profile by averaging the normalized residual along $\tilde{z}$ over the interval $[-1/3, 1/3]$. This averaging step will be necessary when dealing with noisy experimental data to improve the SNR of the vortex profile, so we apply it also on numerical data to compare consistent results. We fit the profile with the Gaussian

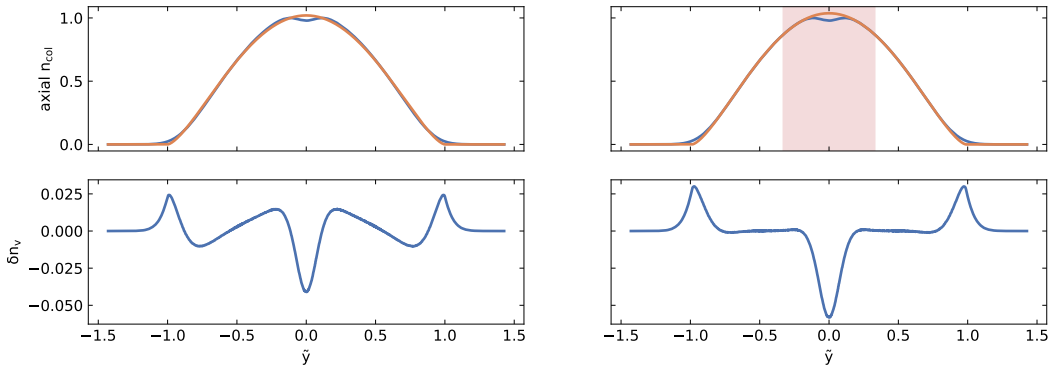

Figure 4.5: First (left) and second (right) TF fit to extract the vortex profile. Top: slice at $\tilde{z} = 0$ of the normalized axial column density from the GPE simulations plotted in Fig. 4.1b, fitted with a TF profile. The shaded area marks the region excuded from the second fit. Bottom: Fit residuals, showing a density bump around the vortex core in the first fit, which is corrected in the second one.

function $g(\tilde{y}) = -d\, e^{-\tilde{y}^2/2\sigma^2}$ to measure the vortex width σ and the depth d.

The procedure is repeated, starting from the Thomas–Fermi fit of the column density image, but this time we exclude from the fitted region a stripe of width $\pm 3\sigma$ around the vortex line. This is because letting the fit go through the vortex dip results in an underestimate of the peak density at the edges of the nodal line, and in the presence of positive bumps in the residual profile. Fig. 4.5 shows a comparison between the two fitting procedures. In the upper panels we plot a slice of the column density and of the TF fit at $\tilde{z} = 0$, zooming around the vortex core. The lower panels show the vortex profiles obtained from the fit residuals. After the second iteration we get the final values of σ and d.

Fig. 4.6a shows the evolution of the vortex profile at increasing expansion times, obtained from the GP simulation of a condensate with $\tilde{\mu} = 9.7$. As expected, since the density depletion of the vortex is very narrow, the profile depth is only a few percent of the central column density of the condensate. The depth increases during the expansion, as the solution in Eq. 1.18 for the hollow-core vortex model would suggest, while the width remains constant.

Fig. 4.6b compares the time evolution of the vortex profile parameters for condensates with different atom numbers. The black dashed line corresponds to the hollow-core model prediction Eq. 1.18, where the value of the parameter $c = 1.62$ was determined fitting to the $\tau = 0$ profile in Fig. 4.6a. This makes the rescaled width of the hollow vortex $\tilde{r}_c = c\xi_0/R_\perp = 0.08$ for the given value of $\tilde{\mu}$, in good agreement with the width σ fitted by the Gaussian model. The scaling for hydrodynamic expansion $\propto \sqrt{1+\tau^2}$ is valid only at short times, and as the mean-field interaction decreases with the density the expansion goes in the ballistic regime [29], where both the rescaled width and depth of the defect saturate to a constant value.

The analysis of experimental images follows the same procedure. We fit both the axial and the radial images with Eq. 4.1, obtaining a first estimate for the width of the sample in all three directions and of the number of atoms. The fit residuals in both directions allow us to clearly identify the presence of vortices, and to determine their number and orientation as shown in Fig. 4.4(c-g).

The condensate is slightly elongated and twisted in the axial image: we attribute this to a residual curvature in the levitating field, that introduces a weak anti-trapping potential of a few Hz along the z direction that deforms the condensate during the long

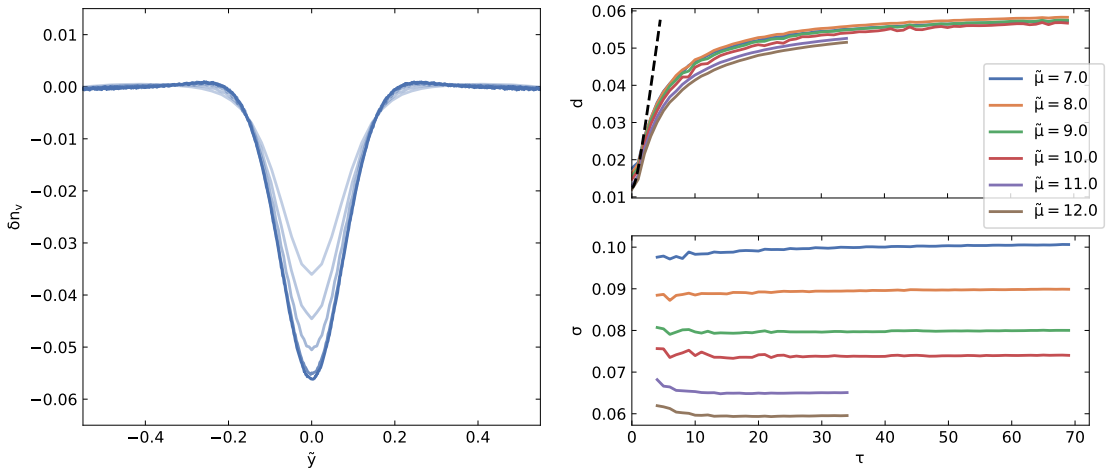

Figure 4.6: Left: Time evolution of the vortex profile for the GP simulation in Fig. 4.1 ($\tilde{\mu} = 9.7$), plotted at time $\tau = 5, 10, 20, 50, 69$. Right: Time evolution of the Gaussian depth d (top) and width σ (bottom) for different values of the chemical potential $\tilde{\mu}$. The black dashed line in the depth plot is the hydrodynamic scaling $d \propto \sqrt{1+\tau^2}$.

TOF. We leave independent fitting parameters for the Thomas–Fermi radii R_y and R_z and for the rotation angle of the ellipsoid, and define $R_{TF} = \sqrt{R_y R_z}$ as the radius we use to normalize the vortex width.

The data are postselected, retaining only the ones where the vortex line has certain characteristics. First we select only the images with one single vortex, discarding the case of multiple vortices like in Fig. 4.4(f-g) to avoid that the shape of the nodal is influenced by the velocity field of other vortices, or by vortex-vortex interaction events [65]. Then we select only the images where the vortex line is straight enough and as close as possible to the center, with a threshold distance of $R_{TF}/3$. In this way we try to match in the experimental shots the same case deterministically produced in the numerical experiments, with one single isolated vortex perfectly straight through the center. Moreover, both the bending and the distance from the center contribute to reduce the vortex visibility and would make it more complicated to analyze.

We measure the position and orientation of the vortex by manually marking two points along the nodal line in both residual images, as shown in Fig. 4.7. From the markers' coordinates we determine the angle of the line on the yz plane and its 3D position, as the geometric distance between the line and the condensate center along the three directions (x is measured on the radial image, y and z on the axial one). To compute the 1D vortex profile we define the rotated coordinates $\tilde{y}$ and $\tilde{z}$ as respectively the axis of the vortex line and the perpendicular direction, both normalized to the transverse Thomas–Fermi radius R_{TF} (Fig. 4.7b). We average the residual along $\tilde{z}$ over the interval $[-1/3, 1/3]$ to improve the SNR, then we fit it with the Gaussian profile and extract first estimates for the width σ and the depth d. Finally we repeat the analysis of the axial image excluding the stripe at $\pm 3\sigma$ around the vortex ad get the final values of the vortex parameters.

4.4 Results

Fig. 4.8 summarizes the results from both GPE simulations and experiment for the profile parameters d and σ as a function of the inverse chemical potential $1/\tilde{\mu}$, including the limiting case of an infinite condensate at $1/\tilde{\mu} = 0$. GPE data are shown in black,

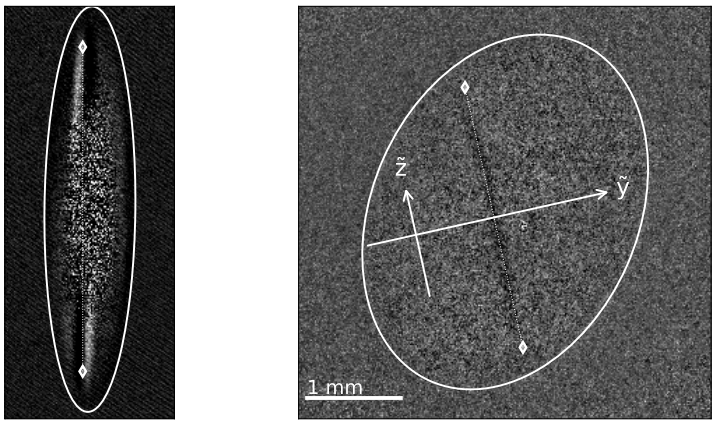

Figure 4.7: Radial (left) and axial (right) column density residuals. The vortex line is manually marked by two points, which are used in the axial image to fix the orientation of the reference frame used to compute the vorex profile.

while experimental data are colored and grouped in four distinct datasets, where the experimental routine and the image TOF were optimized for different atom numbers. The parameters of each the dataset are summarized in Table 4.1. Error bars account for statistical noise in the residual column density and for uncertainties in the fit.

The GP results in panel (a) show that the rescaled width σ is linear in $1/\tilde{\mu}$. This is in agreement with the expected scaling with the healing length $\xi/R_{TF} \propto 1/\mu$ which is maintained also during the expansion, in both the hydrodynamic and ballistic regimes (Fig. 4.6c). The dashed line is a linear fit to the GP points only. The experimental points lay on the line in good agreement with the GP predictions, especially for the data with the largest atom number that have a better SNR on the vortex profile.

Regarding the vortex depth, there are no simple scaling laws from the Thomas–Fermi theory. The numerical results in Fig. 4.6b show that the depth saturates after a long expansion, so that it is fair to compare asymptotic values for its dependency on $1/\tilde{\mu}$, which is seen on Fig. 4.8b to be smoothly decreasing to zero as the number of atoms increases ($1/\tilde{\mu} \to 0$). The experimental points confirm this trend, and they are compatible with theory in the sense that any reasonable interpolating function down to the infinite condensate limit would pass through most of the experimental points within error bars.

Finally we plot a scaled GP profile on top of an experimental one, to make a direct comparison beyond the features that can be extracted by the Gaussian fit. In Fig. 4.9, blue dots are the vortex profile from a condensate in the orange dataset, with 2×10^7 atoms ($\tilde{\mu} = 34$), measured after a TOF of 150 ms. The black line on top is extracted from a GPE simulated condensate at $\tilde{\mu} = 9.7$, where its coordinate $\tilde{y}$ has been rescaled by the ratio between the chemical potentials, while the depth (in absence of a prediction for its value as a function of μ) has been scaled to simply match the one measured on the experimental profile. Here we can see that, after a proper scaling of the profile geometry captured by the data in Fig. 4.6, the overall shape of the vortex dip in the column density is in good agreement with the prediction of the Gross–Pitaevskii equation.

Conclusions

To summarize, in this project we present a first measurement of the spatial structure of the core of a quantized vortex, imaged with standard optical methods after a time-of-flight expansion. With a TF fitting procedure we extract the density dip left by the vortex

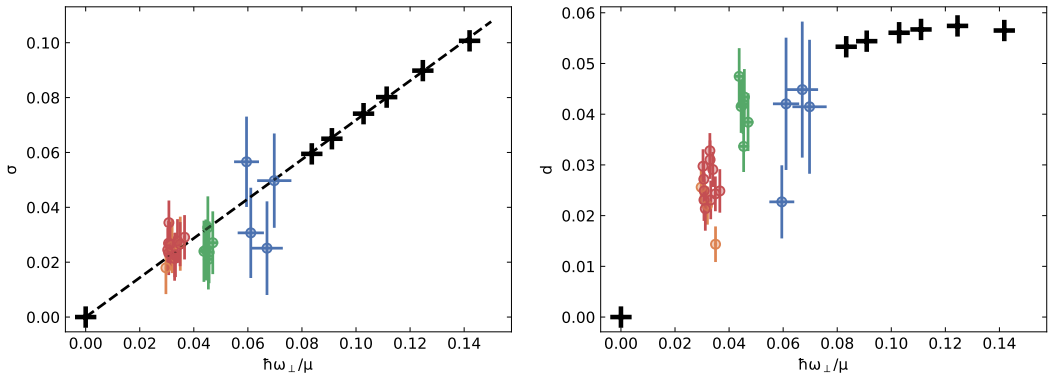

Figure 4.8: Width (left) and depth (right) of the 1D vortex profile after long expansion times as a function of $1/\tilde{\mu}$. Here the simulated and experimental data are plotted together, showing good agreement. Figure adapted from [59].

Table 4.1: Experimental parameters for data in Fig. 4.8

data	N [$\times 10^6$]	μ [$\hbar\omega_\perp$]	TOF [ms]
black (GPE)	0.3 to 1	7 to 12	120
blue	3.5(7)	17(1)	100
green	7.5(7)	23(1)	120
orange	20.1(7)	34.0(5)	120
red	19.2(5)	33.4(3)	150

in the OD profile of the condensate, whose shape is parametrized by a heuristic Gaussian fit returning the visibility of the defect and its width. We apply the same procedure to the density profiles simulated by the GPE, which first is solved in imaginary time to compute the in-situ shape of the vortex line, and then propagated in real time to simulate the expansion dynamics. In this way we obtain from the simulations a prediction for the time dependence of the vortex parameters during the free expansion: we observe that the visibility is enhanced by the TOF, due to the difference in the scaling between the axial and radial direction of the BEC, and that the width is proportional to the transverse TF radius at all times during the expansion.

We measured the dependency of the asymptotic vortex parameters on the number of atoms, parametrized by the rescaled chemical potential $\tilde{\mu}$. The experimental data and the numerical simulations provide information in different and mutually inaccessible parameter ranges, as it is computationally expensive to simulate condensates with a high atom number, while it is difficult to experimentally produce small condensates hosting a single vortex using a temperature quench.

The experimental results show good agreement with the theoretical values, which are extrapolated at higher $\tilde{\mu}$ with TF scaling arguments. The width of the vortex line follows the TF linear scaling with $1/\tilde{\mu}$. There is no expected prediction for the visibility, but the data are seen to follow a reasonable interpolation between the simulated results and the limiting case at $\tilde{\mu} \to \infty$.

We conclude this work with a quantitative comparison of the shape of the vortex density dip with GP theory, observing that the whole profile of the vortex line matches the one predicted in the simulations after rescaling their width and depth according to the above results.

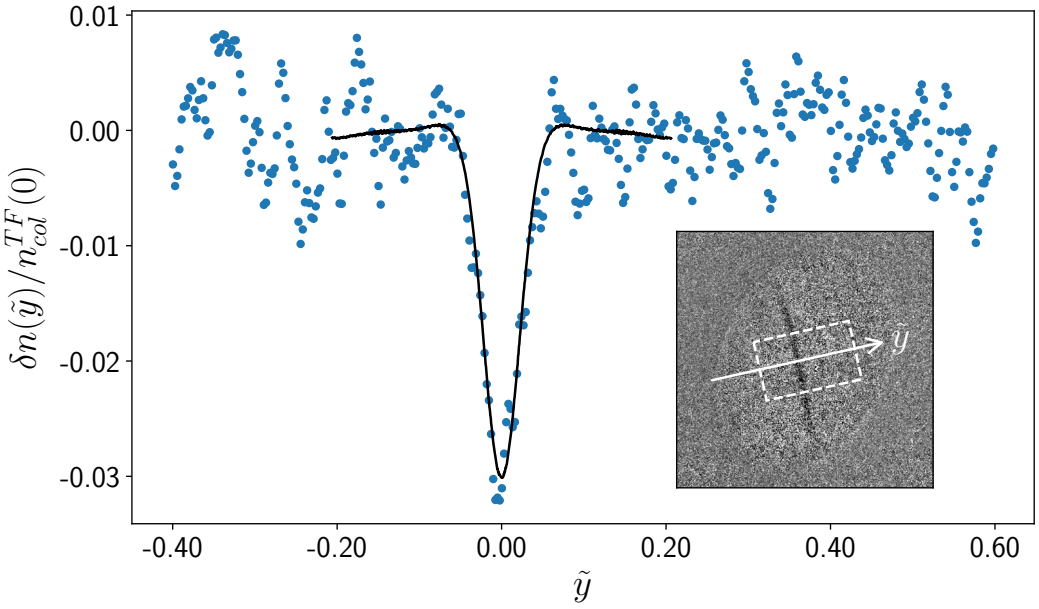

Figure 4.9: Direct comparison of the shape of a vortex. Blue dots: 1D vortex profile of a condensate with 2×10^7 ($\tilde{\mu} = 34$) after an expansion of 150 ms. The inset shows the Ax-residual image, and the rectangular box marks the area averaged along $\tilde{z}$ used to obtain the plotted profile. Solid line: vortex profile of a simulated condensate at $\tilde{\mu} = 9.7$, after scaling the width according to the fitted TF linear law and the depth to match the one measured in the experiment. Figure from [59].

Chapter 5

Equation of State

The goal of this project is to measure the EoS of a homogeneous interacting Bose gas, with a focus on the temperature dependency of the chemical potential μ. In particular, we aim to verify the presence of a non-monotonic behavior of μ, with a peak around the critical temperature. The presence of this peak is believed to be a signature of the transition to the superfluid phase, and its presence has been already experimentally verified in various kinds of superfluid systems other than the Bose gas, for which there is still no direct observation.

We reconstruct the EoS for a homogeneous system from the direct measurement of the density distribution of a trapped atomic sample, following an approach based on the Gibbs–Duhem relation and the local density approximation presented by Ho and Zhou [74]. As the gas equilibrates in the external trapping potential V_{ext}, reaching a homogeneous temperature T, the particle distribution will be determined by the EoS of the uniform system, which relates density and temperature with the local chemical potential $\mu = \mu_0 - V_{ext}$.

Measuring both the density distribution and the global variables μ_0 and T corresponds then to measuring the EoS for a homogeneous system at constant temperature, in a range of chemical potential determined by the trap. In the presence of a condensate, the points in the center of the trap have the highest condensed fraction and provide data about the condensed phase of the system. Moving towards the periphery, the local condensed fraction decreases, down to the point corresponding to the Thomas–Fermi radius where the condensate vanishes as we cross the phase transition. Farther in the tails of the distribution, the gas is in the normal phase and approaches the limit of a perfect non-interacting gas.

This method allows to explore the whole phase diagram of a uniform BEC system within a single trapped sample. It is a powerful result, that however requires to measure the absolute density of the gas everywhere, in a well-known trapping potential. This is challenging in the case of Bose gases, because in the condensed phase the density inside a trapped sample can vary by two or three orders of magnitude between the center and the tails, and standard optical imaging methods are effective only at low optical density, and only in a limited range.

We tackled this problem with the use of the partial-transfer absorption imaging technique, which allowed us to accurately measure the density of the sample in a wide range, from the high-density region in the center of the BEC to the low-density one on the thermal tails. With a sequence of images, in each of which the imaging parameters are tuned to be sensitive in a different density range, we built a complete image of the column density of the sample using an image reconstruction method I developed for this project. From the column-integrated density obtained in this way, we computed the 3D density distribution using the inverse Abel transform.

In this chapter I will describe the details of the techniques summarized above and present our results for the pressure and density profiles along the trap axis. I will discuss the method we used to extract the global thermodynamic parameters from such profiles. I will show our results for the EoS $p(n,T)$ and $\mu(n,T)$, where we observed the peak across the transition, and discuss both our experimental limits and the conditions for the validity of the LDA, which is at the basis of these results.

5.1 Partial transfer absorption imaging

Standard imaging methods are not suited observe atomic samples of high density. Resonant absorption imaging measures the transmission of the atomic medium, which scales exponentially with the column density integrated along the line of sight. Non-resonant imaging methods are affected by the atomic density due to strong refraction of the light. Moreover, working in a magnetic trap we cannot make use of Faraday imaging or other polarization-based imaging schemes, since to take advantage of the elongated geometry of the trap we need to image the BEC along a radial direction, perpendicular to the bias field of the trap.

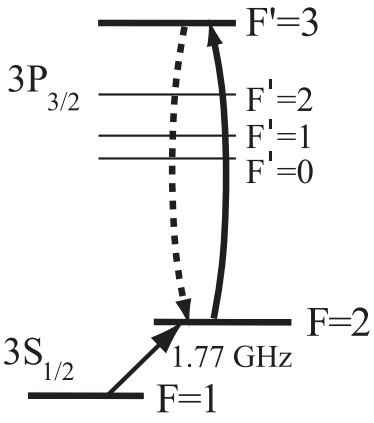

Figure 5.1: A scheme of the hyperfine ^{23}Na levels involved in the PTAI. Figure from [62]

The partial-transfer absorption imaging method (PTAI) [62] makes it possible to fulfill all our requirements. In this technique, a controlled fraction of the atoms is transferred to an auxiliary level, from where it is imaged with a resonant beam. The transferred fraction controls the optical density of the imaged sample, which can be put in the optimal range for absorption imaging. This makes it possible to image arbitrary high atomic densities retaining all the advantages of the absorption method in terms of resolution and SNR. The technique of output-coupling a small fraction of atoms out of the whole sample for studying its properties was first explored in the context of atom lasers [134]. Then it was used as an imaging method to observe the real-time dynamics of vortices [61] and was later demonstrated also for in-situ imaging of trapped atomic samples [135].

We implement PTAI by radiating the atoms with microwave radiation, which transfers them from the $|F=1, m_F=-1\rangle$ state, where they

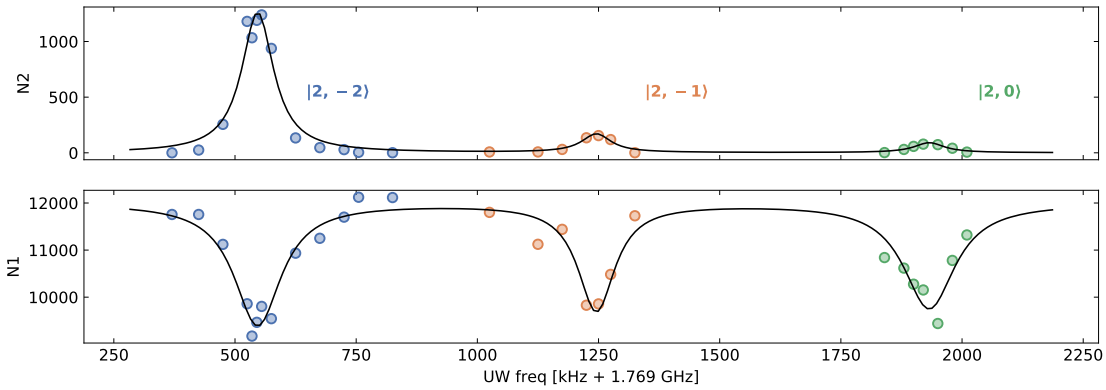

Figure 5.2: Microwave frequency scan. From left to right, the peaks correspond to the microwave transitions from $|1,-1\rangle$ to $|2,-2\rangle$ at 546(3) kHz, to $|2,-1\rangle$ at 1245(4) kHz, and to $|2,0\rangle$ at 1932(4) kHz. The frequency axis is offset by 1.769 GHz. Top row: number of atoms flipped to $F = 2$. Bottom: population remainig in $F = 1$.

are magnetically trapped, to the upper hyperfine level $F = 2$. The transferred atoms are then imaged with light resonant to the $F = 2 \rightarrow F' = 3$ cycling transition. The microwave is generated with a MARCONI 2024 signal generator, amplified with a high-power MINICIRCUITS ZHL-100W-272+ amplifier, with a maximum output of 100 W, and delivered to the atoms with a hook antenna (Fig. 2.6).

The antenna is positioned such that the oscillating magnetic field it produces at the position of the atoms is oriented orthogonal to the x axis, which is the direction of the trap bias field, driving $\sigma^{\pm}$ transitions ($m_F \rightarrow m_F \pm 1$). Nonetheless, an oscillating x component of the field is also present, driving π transitions ($m_F \rightarrow m_F$). We can then selectively address one among the $F = 2$, $m_F = (0, -1, -2)$ states by tuning the microwave frequency. The bias field in the magnetic trap is approximately 1 G, which splits the Zeeman states in both the $F = 1$ and $F = 2$ levels by 700 kHz. The choice of the auxiliary state is irrelevant for the subsequent imaging, as their separation is much smaller than the optical linewidth of 10 MHz. Fig. 5.2 shows a broad scan of the microwave frequency, where all the three hyperfine transitions are revealed by measuring in TOF the transferred and remaining populations after a microwave pulse at fixed power and pulse time.

We decided to use as auxiliary state the $|F = 2, m_F = -2\rangle$: as we are coupling two stretched levels (highest $|m_F|$), the transition has the highest Clebsh–Gordan coefficient, which means we maximize the coupling strength for the same delivered power. Moreover, spin-flipping collisions in the resulting hyperfine mixture are suppressed due to conservation of total m_F, avoiding a strong source of atom losses.

5.1.1 Effects of inhomogeneous magnetic field

The major issue of using this method in a magnetic trap is that the microwave resonance frequency depends on space. Because the Zeeman shift due to the trap field is different in the two coupled levels, the result is that the transferred fraction is not spatially homogeneous, which effectively introduces distortions in the measured density profile. We model this effect and include it in the measurement of the microwave Rabi frequency, which calibrates the PTAI method, and discuss the regime in which the inhomogeneity can be neglected for the measurement of in-situ density profiles.

The population transfer is described by Rabi oscillations in a two-level system. The microwave induces magnetic dipole transitions between the hyperfine levels, and its

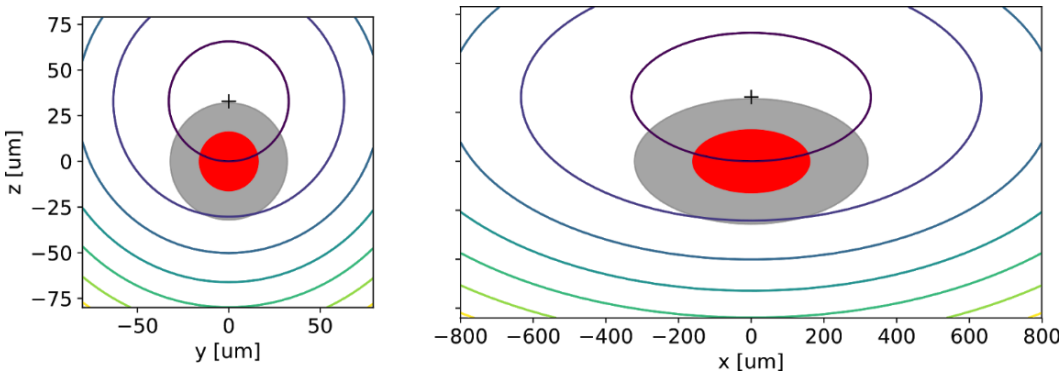

Figure 5.3: Sketch of the atomic sample in the magnetic trap, with magnetic field contour lines. Slices on the yz plane (left) and xz plane (right). In a coordinate system centered on the atomic sample, the minimum of the magnetic field is placed above the atoms at a position $z = z_{sag}$. The ellipses show the boundaries of the BEC fraction (TF radii) and of the thermal fraction (at $2.5\,\sigma$).

coupling strength is measured by a Rabi frequency Ω proportional to the amplitude of the microwave field. The fraction of atoms transferred after a pulse time t is

$$P(t,\delta) = \frac{1}{1+\delta^2} \sin\left(\frac{\Omega t}{2}\sqrt{1+\delta^2}\right)^2 , \tag{5.1}$$

where $\delta = (\omega_{\mu w} - \omega_{HF})/\Omega$ is the detuning from resonance in units of the coupling Rabi frequency, and $\omega_{\mu w}/2\pi$ is the frequency of the microwave.

The hyperfine resonance frequency $\omega_{HF}/2\pi$ depends on the energy splitting between the selected levels, $\hbar\omega_{HF} = E_{|2,-2\rangle} - E_{|1,-1\rangle}$. The energy of each level is shifted by the linear Zeeman effect as a function of the modulus of the local magnetic field $|B(x,y,z)|$. In the region occupied by the atoms, the magnetic field is of the order of 1 G, so that second order Zeeman terms can be neglected.

The total potential experienced by the trapped $|1,-1\rangle$ atoms is $V_{ext} = E_{|1,-1\rangle} + mgz$, the sum of the Zeeman energy of the level $E_{|1,-1\rangle}$ and of the gravitational potential mgz.

Substituting Eq. 1.6 for the expression of the harmonic potential, we can write $E_{|1,-1\rangle}(x,y,z) = V_{ext}(x,y,z) - mgz = E_1 + V_{ext}(x,y,z-z_{sag})$, where E_1 is a constant energy offset. The equilibrium position of the cloud where $V_{ext} = 0$ does not coincide then with the minimum of the magnetic field, which is is placed above the atoms at a position $z = z_{sag}$, where $z_{sag} = g/\omega_z^2$ is called *gravitational sag*, and g is the local acceleration of gravity.

The same applies for the upper state $|2,-2\rangle$, with the difference that Landé factor in $F = 2$ has opposite sign (which makes it an anti-trapped state), which results in $E_{|2,-2\rangle}(x,y,z) = E_2 - 2V_{ext}(x,y,z-z_{sag})$.

The frequency $\omega_{\mu w}$ is set to the value that cancels the spatially-independent detuning term, which is found experimentally as the frequency that maximizes the transfer at a fixed power. Substituting the above expressions in the definition of δ leads to

$$\delta(x,y,z) = \frac{3m}{2\hbar\Omega}\left(\omega_x^2 x^2 + \omega_y^2 y^2 + \omega_z^2(z^2 - 2z z_{sag})\right) . \tag{5.2}$$

Rabi frequency calibration

When the Rabi frequency Ω is known, we can calibrate the PTAI using Eq. 5.1 to calculate the fraction of atoms that are imaged after the pulse. I developed a simple model to measure Ω which takes into account the spatial dependency of the detuning.

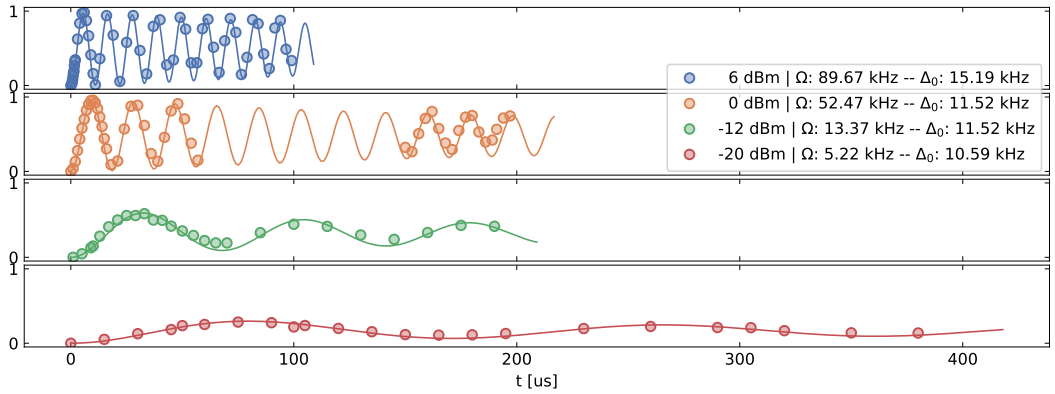

Figure 5.4: A series of Rabi flop measurements at different microwave powers. From top to bottom: 6, 0, −12, −20 dBm. The figure legend reports the values of Ω and Δ_0 resulting from a fit of Eq. 5.5.

The Rabi frequency is obtained with the standard method of measuring the time dependency of the atomic populations during a Rabi flop. We prepare a BEC trapped in $|1,-1\rangle$, pulse the microwave coupling to $|2,-2\rangle$ for a time t, and let the transferred atoms fall under the action of gravity and of the anti-trapping magnetic field, which is left on. In this way we separate the two populations, and after a limited TOF (~ 10 ms) we image the falling atoms with a resonant probe, measuring their number N_2. The remaining atoms are then released from the trap and imaged in TOF with an optical repumper to count their number N_1.

We image both populations to minimize errors in the Rabi frequency due to shot-to-shot number fluctuations in the preparation of the atomic sample. The experimental transferred fraction is

$$\tilde{P}(t) = \frac{N_2}{N_1 + N_2} = \frac{1}{N_1 + N_2} \int P(t, \delta(r))\, n(r)\, d^3r\,, \tag{5.3}$$

which is related to Eq. 5.1 by an integral over the atomic density. We expect the Rabi oscillations to have a reduced contrast, since the inhomogeneous detuning effectively introduces spatial decoherence across the atomic cloud, so that not all the atoms are flipped simultaneously.

To extract the value of Ω from the above expression, we introduce some approximations. Since the atoms are vertically displaced by the gravitational sag, if the atomic sample is small enough with respect to the spatial variation of the field, then only the term linear in z in Eq. 5.2 is important in the region occupied by the atoms, so we can neglect the quadratic terms and rewrite $\delta \propto 2 z z_{sag}$. Moreover, we approximate the atomic density distribution with a Gaussian shape, to separate and integrate out the two spatial directions where the detuning does not vary and remain with an integral along z. With a change of variables to integrate over δ, Eq. 5.3 reads

$$\tilde{P}(t) \simeq \frac{1}{\sqrt{2\pi}\Delta_0} \int P(t, \delta)\, e^{-\delta^2/2\Delta_0^2}\, d\delta\,, \tag{5.4}$$

which shows that the effect of the field gradient is to average the transferred population over the local detuning, with a weight dependent on the atomic distribution. The width Δ_0 represents the range of magnetic field spanned by the condensate in frequency units, and depends on the microwave field strength and on the size of the atomic sample. Both a high Rabi frequency or a small atomic sample reduce the inhomogeneity seen by

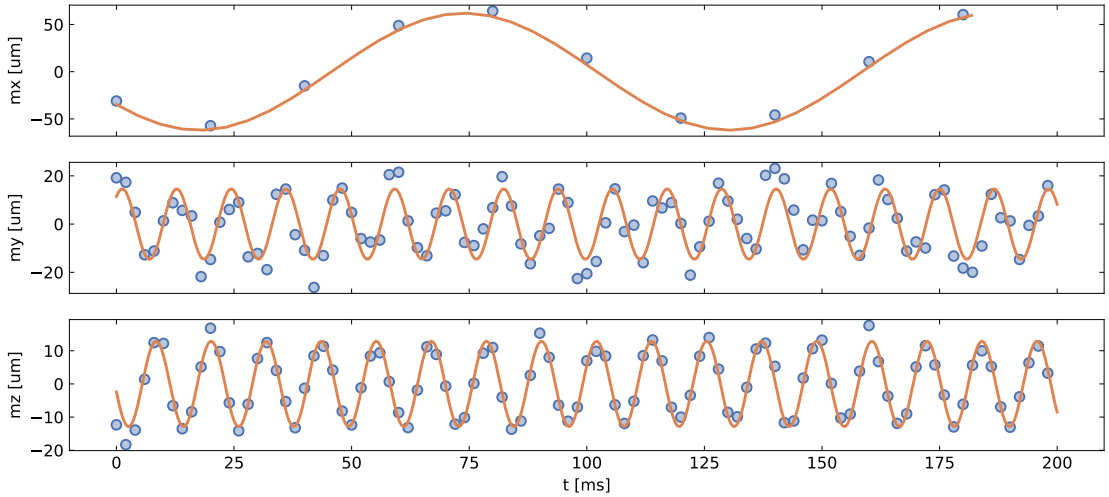

Figure 5.5: Trap frequencies measurement. From top to bottom, fit to the in-situ displacement of the BEC along the x, y and z axes.

the atoms and lead to Rabi oscillations with maximum contrast. In our trap, a BEC of 5×10^6 atoms has a transverse size of 12 µm, which corresponds to a frequency width Δ_0 of almost 20 kHz.

Within these approximations the integral in Eq. 5.4 can be solved analytically and the result is

$$\tilde{P}(t) = \frac{1}{2\sqrt{1+2D^2}} \left(1 - \frac{\cos(\tau + \arctan(b)/2)}{(1+b^2)^{1/4}} \right) , \tag{5.5}$$

where $\tau = 2\pi\Omega\, t$, $D = \Delta_0/\Omega$ and $b = \tau D^2/(1+2D^2)$. Fig. 5.4 shows a series of Rabi flop measurements at different microwave powers. The data are fitted to the expression in Eq. 5.5 with Ω and Δ_0 as free parameters. The fit results are reported in the figure legend.

To check the validity of this approximate model, we also compute the transferred fraction from a numerical integration of Eq. 5.3, computing the detuning from Eq. 5.2 using our trap parameters and the density distribution as a TF profile from the known number of atoms. We fit the data in Fig. 5.4 to the numerically computed fraction with Ω as the only free parameter, and find that the analytical approximation agrees well with the numerical model.

5.2 The experiment

5.2.1 Trap frequencies

The trap frequencies that parametrize the atomic potential in Eq. 1.6 are measured from center-of-mass oscillations of the trapped sample.

We produce a BEC in the magnetic trap, which is at rest at the end of the RF evaporation. We displace it from the equilibrium position applying a magnetic field gradient for 10 ms, using a pair of coils in anti-Helmoltz configuration placed along x. The coils produce magnetic gradients in all the three directions, inducing in-trap oscillations along all the axes. We sample the oscillation applying a sequence of microwave pulses coupling to $|2, -2\rangle$ to extract 3% of the trapped sample every 20 ms. The extracted atoms fall for 4 ms before being imaged simultaneously along the x and y directions using

the Ax and the H1 camera, respectively. We are able to make 10 extractions before the condensate is depleted too much and the visibility of the falling cloud is reduced.

The motion of the center-of-mass after TOF is mapped to the in-situ position of the cloud at the time of the extraction, measuring the frequency and amplitude of the BEC oscillation. With this real-time imaging procedure, the in-situ motion of the BEC is measured in a single experimental shot at a sampling frequency of 50 Hz, limited by the frame rate of our camera. A faster acquisition would require cropping the region imaged by the camera, which cannot be made smaller than the size of the falling cloud. This rate is sufficient to measure the axial trap frequency, but not high enough for the radial one. Since the initial conditions of the oscillation are reproducible, we repeat the experiment 10 times shifting each time the sampling start time by 2 ms, and then we interleave the data sequences obtaining a total sampling rate of 500 Hz.

Fig. 5.5 shows the in-situ displacement over time along the three axes. Data along x in (a) come from one single experiment, while the data in (b-c) for y and z are the result of 10 interleaved sequences. Fitting with a sine function we measure the trap frequencies: $\omega_x = 2\pi \times 8.89(3)$ Hz, $\omega_y = 2\pi \times 87.77(3)$ Hz, $\omega_z = 2\pi \times 86.43(6)$ Hz. We fitted the frequency along x also on the interleaved sequence, to increase the number of fitted points, and found a result compatible with the one from one single sequence.

To verify that the extraction process does not affect the motion of the trapped cloud, we repeat the measurement with a more standard method. We excite the oscillation pulsing the magnetic gradient, wait for a variable evolution time, then release the whole cloud and image it after a fixed TOF along the x and y directions. The experiment must be repeated once for each single point on the measured curve, but we ensure that the in-situ motion is not disturbed by other operations. The values of the trap frequencies we find fitting the TOF position vs. waiting time are in good agreement with the ones quoted above.

5.2.2 In-situ imaging

We now turn to the measurement of the in-situ density profiles for the EoS. Before each data run we re-calibrate the Rabi coupling, first scanning the microwave frequency to tune it to the value resonant with the center of the BEC, and then scanning the pulse time to measure the Rabi frequency with the method explained in Sect. 5.1.1. An example of such measurements is plotted in Fig. 5.6.

To sample (in the LDA picture) the full equation of state of the homogeneous gas, we need to produce a trapped condensate keeping a sizable thermal component. We tune the evaporation parameters to obtain samples with a typical number of 8×10^6 atoms and temperature of about 300 nK, corresponding to a BEC fraction of about 30%. To stabilize the number of atoms, we monitor the fluorescence of the DS-MOT during the loading stage using a photodiode, and trigger the beginning of the experiment (gray molasses and magnetic trap loading) when the fluorescence signal reaches a defined value. In this way we reduce the effect of frequency or intensity fluctuations of the cooling lasers, which can affect the loading rate of the experiment.

At the end of the RF evaporation we wait 500 ms to let the sample reach equilibrium, then we image it on the H4 camera with the PTAI technique. We combine PTAI with the fast imaging sequence described in Sect. 3.2.1. We first take the probe picture, when the atoms are still far-off-resonance. With the focusing procedure described in Sect. 3.2.3 we ensured that the probe picture is not affected by the presence of $F = 1$ atoms. Then we repump the desired fraction of the sample and image it with the second picture. The time between the two probe pulses, with the microwave one fired in the middle, is of

200 µs. The imaging conditions are set to $I/I_{sat} = 4$, $\tau = 5$ µs, as discussed in Sect. 3.1.1.

We image different regions of the condensed sample by varying the microwave pulse time. A short pulse puts on resonance only a small fraction of atoms, which we tune so that the central high-density peak reaches an optical density of ~ 2 and can be imaged in absorption without saturation. When doing so, the OD in the outer regions of the cloud is still too low to be measured with a sufficient SNR. Using a longer microwave pulse, the OD in the tails of the distribution is brought to the optimal range for imaging, while in the center the sample becomes too optically thick and the image is saturated.

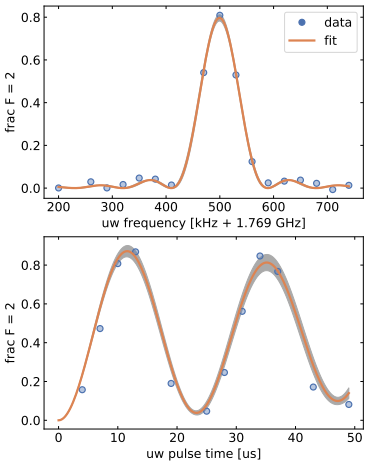

Figure 5.6: Top: microwave frequency scan. The fraction of transferred atoms is fitted with a sinc function to measure the resonance frequency of the $|1,-1\rangle \rightarrow |2,-2\rangle$ transition. Bottom: Rabi frequency measurement with the procedure discussed in Sect. 5.1.1.

In each experimental shot we calculate the repumped fraction $P(t)$ from Eq. 5.1, using the measured microwave pulse time t, the Rabi frequency Ω calibrated in the same run, and where we set $\delta = 0$ neglecting the spatial inhomogeneity of the partial transfer. Fig. 5.7a shows a stack of tree different frames, imaged with increasing microwave pulses. The Rabi frequency for this data is $\Omega = 49.3(3)$ kHz, and the pulse times (with the corresponding $P(t)$) are, from top to bottom: 0.6 µs (0.9%), 1.21 µs (3.5%), 2.41 µs (13.4%). Each image is the average of 4 to 6 experimental shots in the same conditions.

We clean the images from residual interference fringes by selectively removing high spatial frequency peaks in the FFT. To improve on the SNR, we bin and make a moving average along the rows (x axis of the BEC), which is the direction in which the gradient of the trapping potential is lower, and the features in the density profile are expected to be smoother. We do not apply any correction along the columns (z axis), as the sample is 10 times tighter in that direction and filtering would also wash out the spatial features.

5.2.3 Reconstruction of the density profile

With the PTAI method we are able to image arbitrary regions of the BEC, but a single image is not able to cover the whole range of interest. With a technique inspired to high-dynamic-range (HDR) photography, we combine the information from different shots to obtain a complete image of the column density of the trapped sample.

We remove the saturated parts in all the pictures by cropping them out above a threshold of $OD = 3$, chosen to be higher than the maximum OD in the first frame. We plot slices along x of the cropped data in Fig. 5.7b, highlighting the regions where the data from each extraction are considered valid before they are covered by the next one. In the overlap regions we consider only the highest profile, for which the SNR is maximum. The non-overlapping regions of valid data, although sketched only along the x axis, actually form concentric rings, and cover without intersections the whole area of the picture by construction.

Each frame is rescaled by the corresponding transfer fraction, cropped to the validity region, and then joined to the other ones to form a complete HDR image of the optical density of the atomic sample. Fig. 5.7c shows the HDR picture computed from the frames in (a), while in (d) we plot a slice along x indicating the contribution of the single

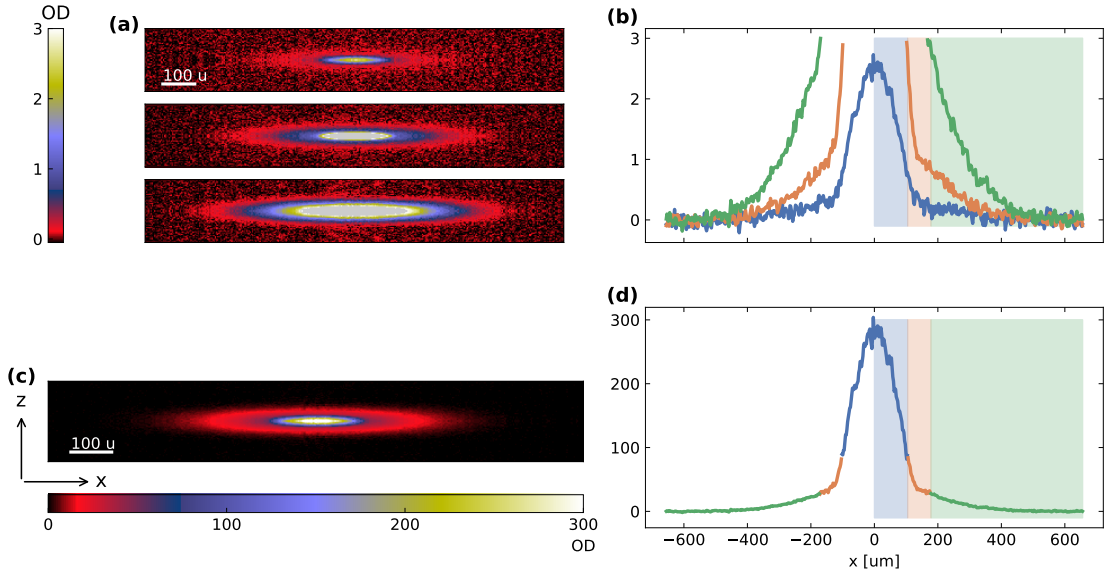

Figure 5.7: (a) Optical density images at different microwave pulse times: 0.6, 1.2, 2.4 µs. (b) Slices along the x axis, showing the validity region of each frame. (c) HDR image of the BEC and (d) slice along x, showing the contributions of each single frame.

frames. The number of atoms, obtained integrating the OD, is of $8.7(5)\times10^6$.

Uniform partial transfer

The reconstruction algorithm described above assumes a homogeneous extraction. This is not exact in the magnetic trap due to the spatially-dependent Zeeman detuning expressed by Eq. 5.2, but we can work in a range of parameters where the extraction $P(t)$ is approximately independent of the detuning and can be considered uniform.

For $\Omega t \ll 1$, we expand Eq. 5.1 in powers of Ωt and find that the transferred fraction is independent from the microwave frequency, scaling as $\Omega^2 t^2/2$. This means that the lowest extractions, which are the ones we use to image the BEC, are the less affected by the inhomogeneity. Moreover, for a given product Ωt (which is equivalent to fixing the fraction we want to extract), a high Rabi frequency helps to minimize the inhomogeneity, as the detuning therm $\delta \propto 1/\Omega$ becomes negligible due to power-broadening of the resonance.

We estimate the systematic error on the density measurement by computing the spatial dependency of $P(t,\delta)$ in our trap geometry, using Eq. 5.2. In Fig. 5.8 we plot a map of the transferred fraction in the xz plane around the atoms, for the parameters used for the data in Fig. 5.7. The area occupied by the sample is sketched by the blue and red ellipses, delimiting the condensate (at the Thomas–Fermi radii) and the thermal fraction (at $2.5\,\sigma$, where the measured density goes to zero within errors) respectively. Fixing the resonance in the center of the atomic cloud, the maps show that the inhomogeneity is stronger along the z direction, due to the gravitational sag, and the lower side of the sample is the most affected. We see that a Rabi frequency of about 50 kHz allows to extract up to 15% of the sample with a top-to-bottom difference in the extraction at the edges of the BEC of less than 1%. The inhomogeneity affects the extraction in the tails of the thermal cloud, with a top-to-bottom difference of up to 25%. However, the atomic density in those regions is 10^2 times smaller than in the BEC fraction, so that they have a negligible contribution to the integrated column density.

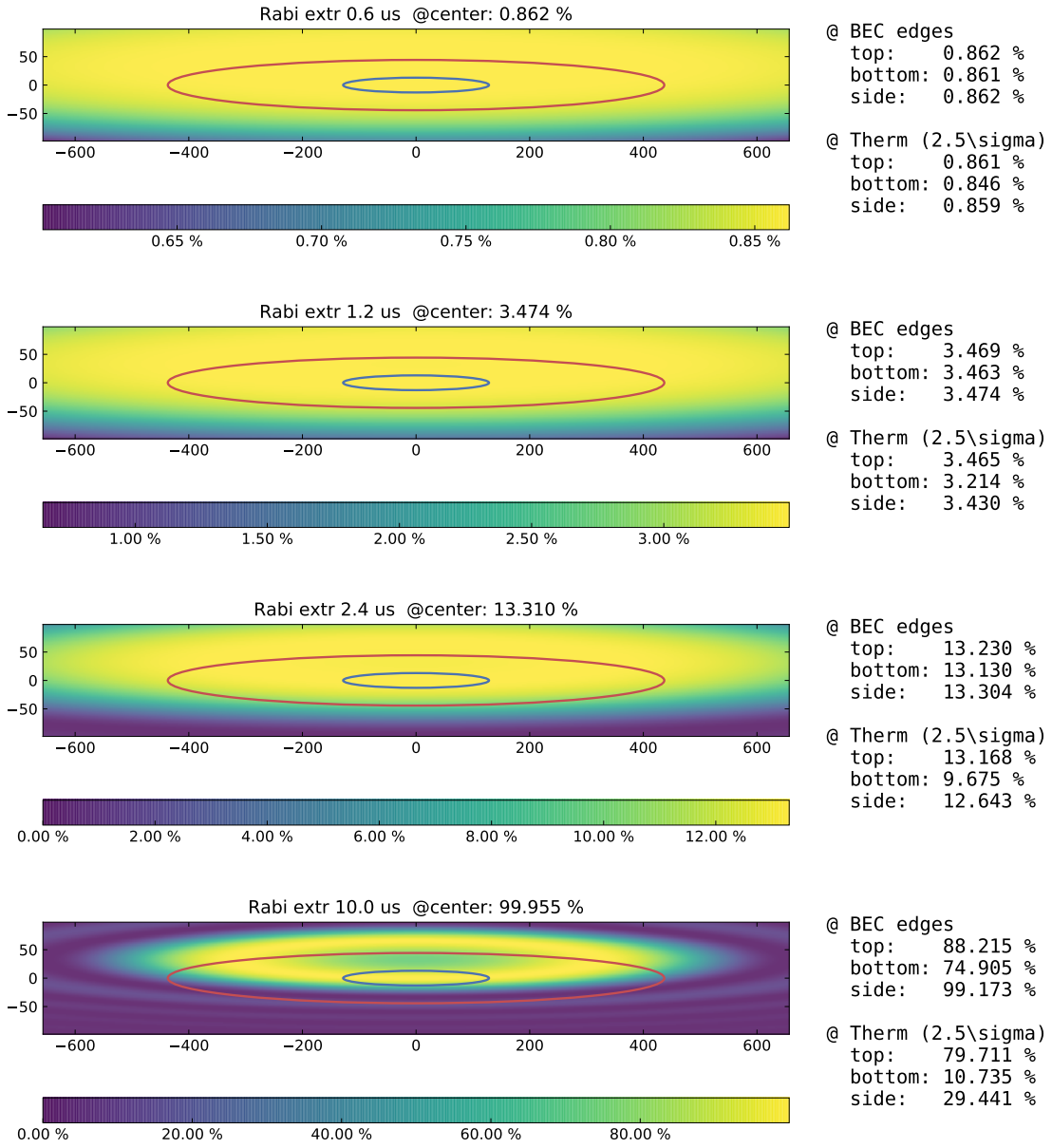

Figure 5.8: Map of the transferred fraction $P(t, \delta(r))$ for a Rabi frequency $\Omega = 2\pi \times 49.3\,\mathrm{kHz}$, calculated on the xz plane using Eq. 5.1 and Eq. 5.2 for four different values of the microwave pulse time (top to bottom): 0.6, 1.2, 2.4 and 10 µs.

5.3 Results

5.3.1 Pressure and density profiles

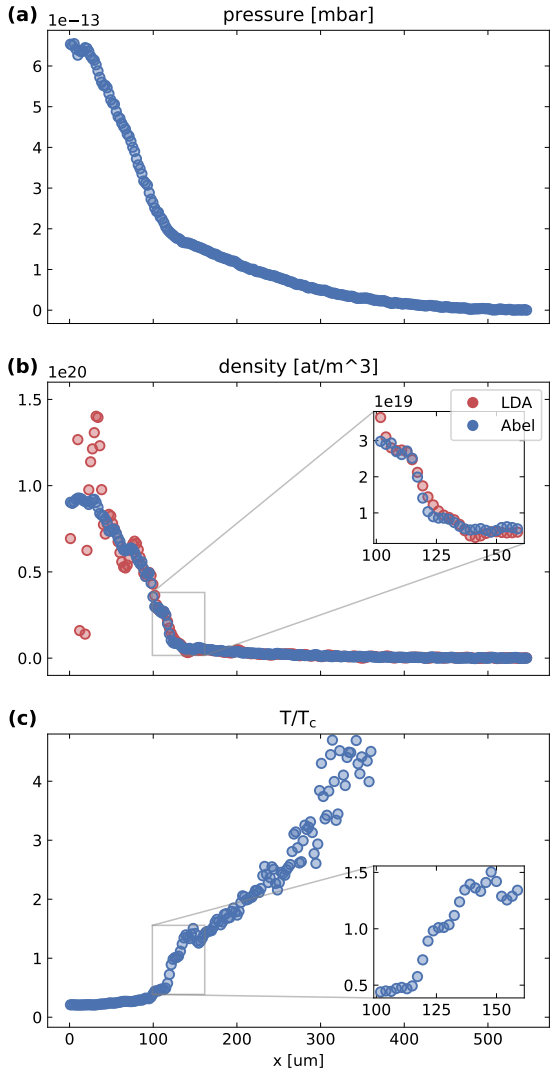

Figure 5.9: (a) Pressure profile $p(x)$ along the trap axis. (b) Density profiles, computed with the LDA method (red) and with inverse Abel transform (blue). The inset shows a zoom on the transition region. (c) Local reduced temperature $T/T_c(n)$ computed from the Abel density data with Eq. 1.28. The inset shows a zoom on the transition region, in the same spatial range as in (b).

We compute the pressure along the x axis using Eq. 1.47, following the LDA method [74]. The doubly-integrated density n_1 is obtained by integrating the optical density along z, as $n_1 = \int OD\, dz/\sigma_0$, and the left ($x < 0$) and right ($x > 0$) side of the image are averaged to exploit the sample symmetry. The resulting pressure profile is plotted in Fig. 5.9a.

We compare the results of two different methods to obtain the density along the axis. The first one uses Eq. 1.48, following from the same LDA approach used for the pressure, and requires to calculate $(1/x)dn_1/dx$. This method is sensitive to experimental noise, because differentiation naturally amplifies high-frequency noise components. To compute the numerical derivative we use a smooth high-order central difference scheme [136], which limits the noise by suppressing the amplification of high spatial frequencies. The density profile obtained with this method, plotted in Fig. 5.9b (red dots), is affected by strong ripples close to $x = 0$, where the $1/x$ factor enhances the oscillations that are not filtered out by the smoothing differentiation method. Trying to suppress them by reducing the frequency cutoff of the filter results in an excessive smoothing of the curve, losing the knee corresponding to the BEC transition point.

Alternatively, we compute the 3D density from the inverse Abel transform of the OD [137]. The Abel transform is an integral transform mapping a slice of a 3D cylindrically symmetric object to the image of its projection on a plane parallel to the symmetry axis. Conversely, the inverse transform allows to retrieve information on the density structure of the object starting from its projection. As a data analysis method, it gained primary importance in the field of photoelectron imaging [138], and was recently proven to be useful also in the cold atoms community [96, 97, 139].

The use of the Abel inversion is possible due to the symmetry of the harmonic

trapping potential. It actually turns out that the requirement for Abel inversion is that the imaged object is elliptically symmetric, meaning that its density distribution depends on a generalized radial coordinate $\sqrt{\lambda^2 x^2 + y^2}$ on planes parallel to the projection direction. This is the same as requiring that the object can be made circularly symmetric with a proper scaling of coordinates. In our trap geometry this is evident around the x axis, because it is the axis around which the Ioffe trap is designed to be symmetric, but the elliptical symmetry is present around any of the principal axes as long as the approximation of harmonic potential is valid.

We choose to consider the rotational symmetry around z and reconstruct the density profile from slices along horizontal planes. This is done computing the inverse Abel transform along the rows of the image, rescaling the x coordinate by the ratio ω_y/ω_x. This allows to take advantage of the noise-reducing operations that was possible to perform only along the rows. If we considered the obvious symmetry around the x axis, this would have required to compute the inverse Abel transform along z, where the noise could not be removed and where the details in the density are less resolved.

As the direct transform is an integration process, implicit in the imaging method, the inverse transform involves differentiation of the data and so it is subject to the same considerations about the noise as in the LDA method. In this case we can take advantage of the variety of numerical implementations for the computation of the Abel transform, which include strategies to suppress the effect of noise. I choose to focus on the Hansen–Law method [140], starting from its implementation in the Python package `PyAbel` [141]. In this method, the transformed function is computed recursively as the solution of a linear set of differential equations, where the derivative of the input function serves as the driving therm. I implemented a version of the Hansen–Law algorithm which uses the high-order differentiation scheme presented above to compute the driving term, and used it for the calculation of the 3D density profile. The result is plotted in Fig. 5.9b. The Abel method performs better than the LDA one in handling the noise: even thought some oscillations are still present, it does not show the strong ripples close to the top of the distribution.

5.3.2 Global thermodynamic variables

We compare the measurements with Hartree–Fock theory, which describes the non-monotonic behavior of the chemical potential in terms of the mean-field interactions between the condensate and the thermal fraction. Within LDA, the density distribution of the trapped gas $n_{HF}(r)$ is described by Eq. 1.32 with the substitution $\mu \to \mu_0 - V_{ext}(r)$, leading to the expression

$$n_{HF}(r) = n_0(r) + n_T(r)\,, \tag{5.6a}$$

$$n_0(r) = \max\left(\frac{\mu_0 - V_{ext}(r) - 2g n_T(r)}{g}, 0\right)\,, \tag{5.6b}$$

$$n_T(r) = \frac{1}{\lambda_T^3} g_{3/2}\left(e^{(\mu_0 - V_{ext}(r) - 2g n_{HF}(r))/k_B T}\right)\,. \tag{5.6c}$$

Likewise, the pressure inside the cloud $p_{HF}(r)$ can be derived from Eq. 1.33 with the LDA substitution.

This means that, within LDA, the shape of the atomic sample is completely determined by the global thermodynamic quantities μ_0 and T, the chemical potential in the center of the atomic cloud and the temperature. We need a method to measure those parameters from the density distribution, as they are necessary to determine the EoS of

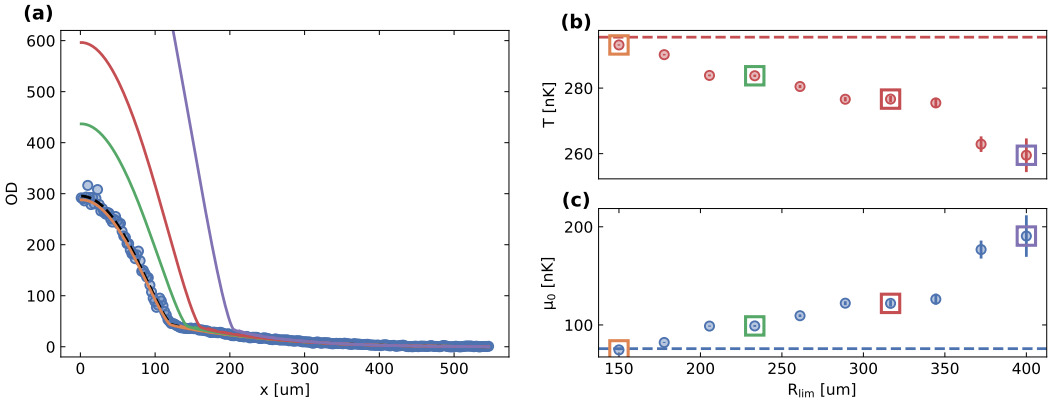

Figure 5.10: Fit of the ideal gas model on the tails of the optical density with two free parameters. Left (a): A slice along x of the OD, the fitted OD_{HF} (black dashed line) and the HF profiles computed from the result of ideal model fits at selected R_{lim}. Right: Fit results for T (b) and μ_0 (c) as a function of R_{lim}. In (b) and (c) the dashed lines mark the best-fit values from the full HF model.

the homogeneous phase. We notice here that the expression 5.6c coincides with Eq. 1.42 for the HF distribution of the thermal fraction in a trapped gas computed in the semi-classical approximation, which states the equivalence of semiclassical approximation and LDA for the distribution of a non-condensed trapped gas.

As a first step, we compute the optical density $OD_{HF} = \sigma_0 \int n_{HF}\, dy$ integrating the HF density along y, which is the imaging direction in our experiment, and make a 2D fit to the reconstructed in-situ image. The values we obtain, $\mu_0 = k_B \times 76.1(1)$ nK and $T = 295.2(1)$ nK, are the ones that best parametrize the measured density distribution according to HF theory.

We also try to measure these parameters in a way that does not directly involve the theory that we are comparing the data with. A common approach is to assume that the tails of the density profile can be approximated using the equation of state of an ideal Bose gas [98], and fit the approximate model only in a limited region of the data. The atomic density of an ideal gas $n_{IBG}(r)$ is calculated by setting $g = 0$ in Eq. 5.6c. Integrating it along y we obtain an expression for the optical density

$$OD_{IBG}(x,z) = \sigma_0 \frac{k_B T}{\hbar \omega_y \lambda_T^2} g_2\left(e^{(\mu_0 - V_{ext}(x,0,z))/k_B T}\right), \tag{5.7}$$

where σ_0 is the resonant cross-section for absorption imaging as in Eq. 3.5.

We select the tails in the OD image (Fig. 5.7c) by considering the region where $x^2 + (\omega_z/\omega_x)^2 z^2 > R_{lim}^2$ and fit it with Eq. 5.7 with both μ_0 and T as free parameters.

Fig. 5.10 shows the results of this method as a function of the threshold radius R_{lim}. On the left (a) we plot a slice along $x > 0$ of the measured optical density, the fitted OD_{HF} (black dashed line), and some OD_{HF} curves calculated using the result of the ideal gas fit at selected values of R_{lim}. On the right (b), the dots show best-fit values from the ideal gas fit in a range of R_{lim}, marking with colors the ones used to plot the profiles in (a). The dashed lines mark the HF fit result. All the fits are two-dimensional, but we only plot a slice of the resulting images for a better visualization.

The ideal model gives results in agreement with the HF predictions, but only when the OD is fitted including regions close to the BEC, where in principle the approximation to ideal gas is less exact. On the other hand we should consider that we are fitting an integrated column density, where the values on the axis even close to R_{lim} are determined

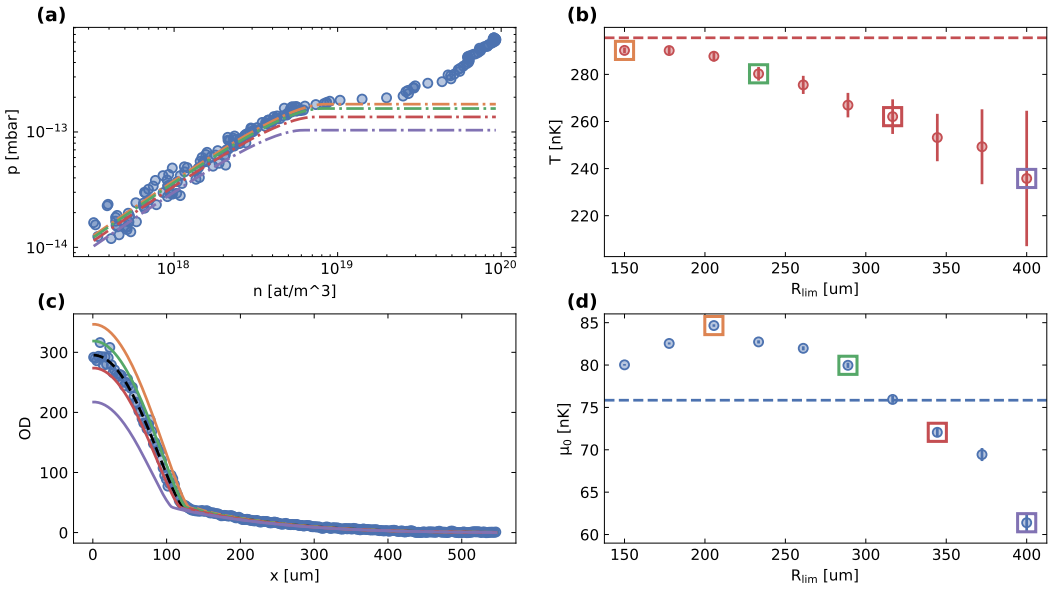

Figure 5.11: Experimental data fit to the ideal gas model, one parameter at a time. (a) Fit to $p(n)$ with T as the only free parameter. (b) Fitted temperature vs. R_{lim}. (c) Slice along $x > 0$ of the measured OD, with HF curves resulting from a 2D fit of OD_{HF} where μ_0 is the only free parameter, while T is fixed to 290 nK fitted on the data in (a). (d) Fitted chemical potential vs. R_{lim}. In (b) and (d) the dashed lines mark the best-fit values from the full HF model.

integrating points whose distance from the center of the cloud is always greater then R_{lim}, such that the ideal model approximation is better suited.

Anyway this fitting procedure is difficult to trust: as the shape of the distribution in the tails is relatively insensitive to variations in μ_0, leaving it as a free parameter results in too high values which are inadequate to describe the distribution in the condensed region, as we can see by computing the corresponding HF profiles.

The use of two fitting parameters is due to our choice to compare the distribution to the EoS $n(\mu, T)$, where in LDA the spatial coordinate takes the place of the chemical potential through the introduction of the parameter μ_0. Since having measured both the pressure and the density profile is equivalent to having measured the EoS $p(\mu, T)$ and $n(\mu, T)$ in the same range of μ, we eliminate the chemical potential by plotting the pressure as a function of the density, and fit it with the EoS $p(n, T)$, where now T is the only unknown parameter. Considering the data in the tails for $x \geq R_{lim}$, we fit using the ideal Bose gas result

$$p_{IBG}(n, T) = \frac{k_B T}{\lambda_T^3} g_{5/2}\left[g_{3/2}^{-1}\left(n\lambda_T^3\right)\right], \tag{5.8}$$

derived from Eq. 1.27 and Eq. 1.33 with $g = 0$.

Fig. 5.11b shows the fitted temperature as a function of R_{lim}, where in (a) we plot in log-scale the experimental pressure vs. density, and the fitted p_{IBG} for selected values of R_{lim}, marked with colors. We see that the temperature has in practice the same behavior as in the previous two-parameters fit (Fig. 5.10), confirming that μ_0 plays a negligible role in the ideal gas model, and is rather a potential cause of overfitting. The temperature that best fits the data in the whole range of the non-condensed phase is $T = 290(10)$ nK.

We fix the temperature in the OD_{HF} function to this value, and repeat the 2D fit on the optical density leaving μ_0 as the only free parameter. The results are plotted in Fig. 5.11(c-d), where the meaning of the displayed curves is the same as in Fig. 5.10. Now the fitted values of μ_0 do not drift away like in the previous case, and are more

Table 5.1: Fitted values of μ_0 and T for different fitting schemes.

fit	μ_0 [$k_B \times$ nK]	T [nK]
OD_{HF}	76.1(1)	295.2(1)
OD_{IBG} ($R_{lim} = 150\,\mu$m)	78.0(4)	292.1(2)
$p_{IBG}(n)$ (T only)	—	290(10)
OD_{IBG} (μ_0 only)	76(3)	—

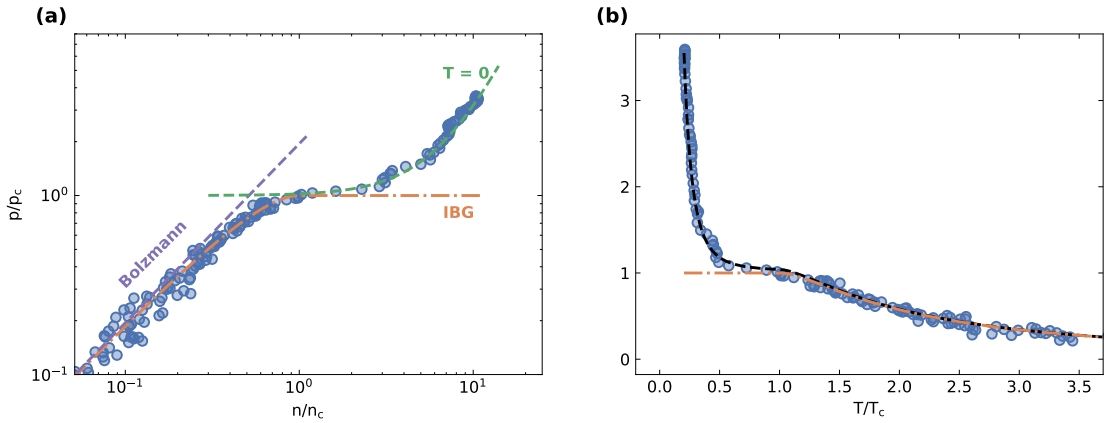

Figure 5.12: (a) $p(n)$ experimental EoS in reduced variables. The data smoothly interpolate between two extreme regimes across the phase transition, the ideal gas model for $n/n_c < 1$ and a simplified zero-temperature model for $n/n_c > 1$, showing that the condensate gives the dominant contribution to the pressure in the condensed phase. On the left, the data approach the perfect gas law $p = nk_BT$. (b) Experimental curve $p(t)$, compared to the HF (black) and the ideal gas model (orange). The data show a clear deviation from the non-interacting regime in the condensed phase.

distributed around the value found by fitting the full HF model. Comparing the different HF profiles computed using the values of μ_0 and T obtained from the combination of the two fits described above, we fix the value of the chemical potential to $\mu_0 = k_B \times 76(3)$ nK. Table 5.1 summarizes the results of the different fitting schemes.

We conclude that fitting an approximate model to a selected region of the data to measure global thermodynamic parameters is in principle a correct procedure, but that can lead to incorrect results when used to describe the data on a global level. Using the pair of values quoted above we compute the HF predictions for the pressure $p_{HF}(x)$ and for the density $n_{HF}(x)$ along the trap axis, which we compare to the measured profiles, and we also use them to compute the EoS for the chemical potential.

5.3.3 Equation of state

Using pressure, density and temperature along the trap axis, we study the equation of state of the interacting Bose gas through the BEC phase transition. A parameter that indicates the crossing of the transition is the reduced temperature $t = T/T_c$, where the (local) critical temperature is a function only of the density through Eq. 1.28. Fig. 5.9c shows the variation of t along the trap axis. An equivalent parameter is the reduced density $n/n_c = t^{-2/3}$, where the atomic density is normalized to the critical density $n_c = \zeta(3/2)/\lambda_T^3$, which is a function of temperature only.

We first discuss the pressure EoS $p(n, T)$ by plotting in Fig. 5.12a the reduced pressure

p/p_c, normalized to the value in the condensed phase for an ideal gas at the same temperature $p_c = k_B T \zeta(5/2)/\lambda_T^3$, versus the reduced density. We see how the data smoothly interpolate between two distinct regimes across the BEC phase transition.

In the normal phase at $n/n_c < 1$ the gas follows the EoS of the ideal Bose gas. In the low density side, corresponding to low values of the chemical potential, one can neglect higher orders in the power series of the polylogarithm functions, thus neglecting the quantum statistics of the particles, and the gas pressure becomes simply proportional to the density, following the ideal gas law $p = nk_B T$.

On the other side of the plot, at $n/n_c > 1$, the pressure is dominated by the contribution of the condensed phase. The data are seen to agree well with a simplified zero-temperature model, $p = p_c + gn^2/2$: neglecting the small thermal fraction, we approximate the pressure as the one of an interacting gas at the same density and zero temperature $gn^2/2$, to which we sum the partial pressure p_c of the thermal component, which is independent of the density.

In Fig. 5.12b we plot the same curve as a function of t, to compare it with the homogeneous gas result shown in Fig. 1.4a. The pressure profile agrees with the same quantity computed from the HF theory (black dashed line), and in both plots it deviates from the ideal gas prediction due to the strong effect of interactions in the condensed phase. The agreement with the simplified $T = 0$ model, where we have completely neglected interaction terms in the thermal fraction, indicates that the pressure of a condensed gas is insensitive to finite-temperature interaction effects, as it is dominated by the much bigger contribution of the condensate.

The fitted value of μ_0 allows to obtain the chemical potential EoS. In Fig. 5.13 we plot the local reduced chemical potential $u = (\mu_0 - V_{ext})/gn$ vs. the reduced temperature t. The data are compared, as in Fig. 1.4b, to the ideal Bose gas theory and to HF theory.

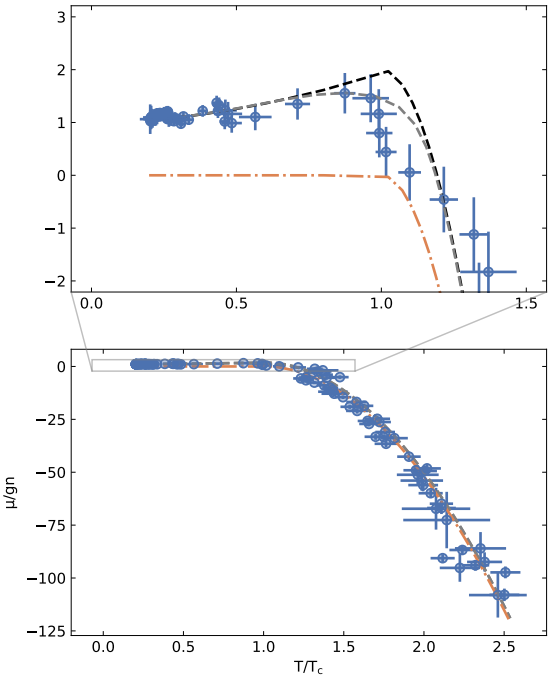

Figure 5.13: Reduced chemical potential $u = \mu/gn$ across the phase transition, as a function of t. Blue dots are experimental data, while the black and orange lines are the HF and ideal gas predctions, respectively. The two plots show the same data on different zoom scales, highlighting the correction due to mean-field interactions. In the condensed region, for $t < 1$, the data follow the non-monotonic HF curve with a smoothed peak close to $t = 1$.

On the bigger scale of the lower plot, the data follow a curve which essentially coincides with the ideal gas EoS, as the mean-field correction becomes negligible when compared to the values of μ in the normal phase. The distinction is evident in the zoomed region of $t < 1$, where the data show that the chemical potential is non-zero and follows the non-monotonic behavior predicted by HF theory, confirming the presence of a peak at the transition. Only the points in a narrow window close to the edge of the condensate (inset in Fig. 5.9b) contribute to the region of the EoS curve where t is close to 1. There the condensate fraction goes to zero, and the mean-field shift in the chemical potential

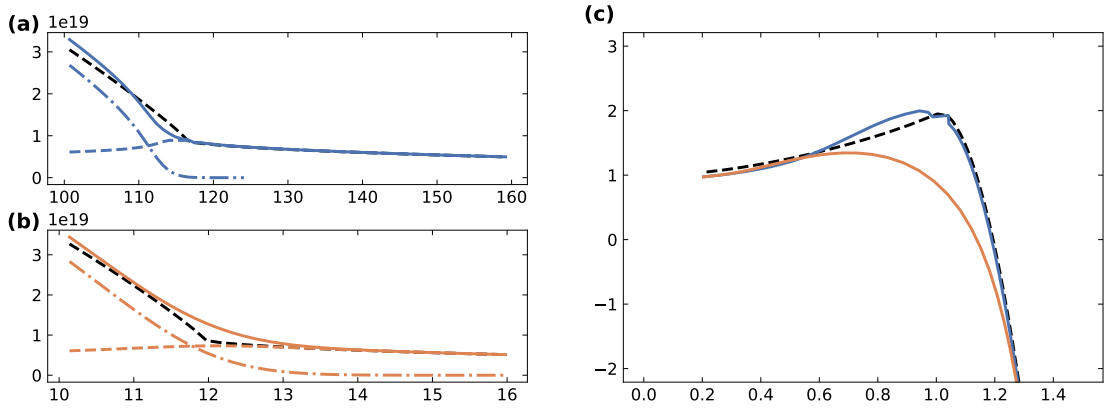

Figure 5.14: Solution of the 3D trapped HF model, for a sample of 8.6×10^6 ^{23}Na atoms at 290 nK with the same trap parameters as in the experiment. (a) and (b) show slices along x and z respectively of the condensate (dot-dashed), thermal (dashed) and total density (solid line), showing that the relative surface width of the condensate, where LDA fails, is negligible along the weak axis x but is instead very relevant along z, breaking the LDA assumption. (c) Plots of the chemical potential EoS measured with the LDA method along x (blue) and z (orange), showing how beyond-LDA effects completely wash out the peak feature predicted in a homogeneous system. The colors correspond to the curves in (a-b). In all the panels, the black dashed line is the HF profile calculated using the LDA.

starts to be dominated by the contribution of the thermal fraction, which is twice as big, resulting in the shifted value $u = 2$. In the inner region of the sample the thermal fraction becomes quickly negligible with respect to the condensate, and the data accumulate close to the $T = 0$ limit value of $u = 1$.

The agreement between the data and the HF curve is still not complete, and it can be affected by a number of factors. Oscillations in the curve are the result of oscillations in the density profile, which are visible also in Fig. 5.9b. These are attributed to the cleaning steps in the data analysis, such as moving averages or high-order differentiation. Any noise-cancelling operation has the effect of low-pass filtering the data in the spatial frequency domain, and as discrete filters cannot be made smooth by definition, this leads to the creation of ringing artifacts in the signal.

Imaging resolution contributes to change the shape of the measured curve, as the peak shape in μ comes from the sharp density change predicted by HF theory at the boundary of the condensate. The width of the transition region along the x axis can be estimated as the range where $0.5 \leq t \leq 1.2$ (the region where, in the EoS plot, $u \geq 1.5$), whose extent is of about 30 µm as shown in the inset of Fig. 5.9c. The limited resolution of our imaging system should smear the peak feature, but still allow us to see the non-monotonic trend. We check this by convolving the fitted OD_{HF} with a 2D Gaussian of 4 µm r.m.s. width (the value measured in Sect. 3.2.4), compute the density from the smoothed image with the same Abel inversion routine we used on real data, and plot the resulting EoS (gray dashed line) on top of our measurement, finding a better agreement on the values close to the peak.

The use of HF theory to predict the properties of the system at the critical point could be questioned, as mean-field theories are notoriously incorrect close to a phase transition, where fluctuations are enhanced. In the case of homogeneous systems, the peak shape of the chemical potential is confirmed by a thermodynamic description based on beyond-mean-field universal relations [72].

From an experimental point of view, the possibility of observing it in a trapped

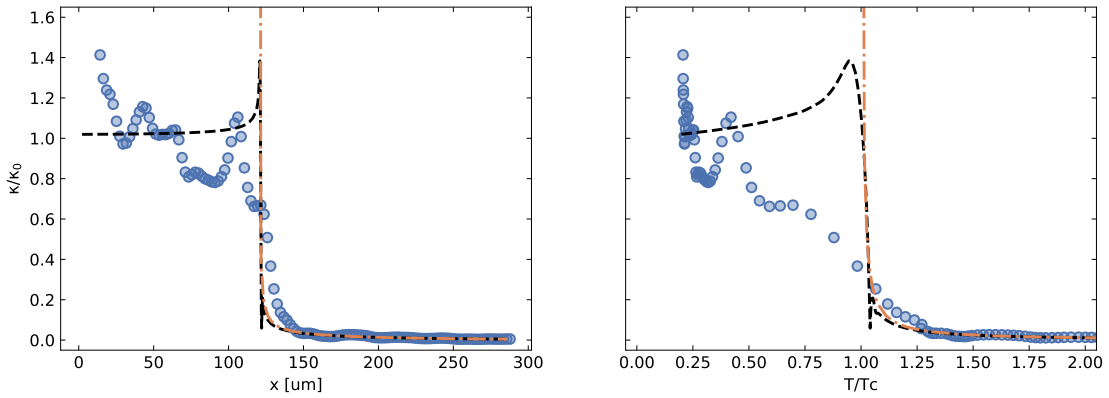

Figure 5.15: Reduced compressibility, plotted versus the axial coordinate (left) and versus T/T_c (right). The black line and the orange line are the prediction from the HF and the ideal gas model, respectively.

sample is based on the validity of the local density approximation, which itself breaks up at the edge of the condensate. The extent of the region where LDA fails can be estimated by the thickness of the surface region of the condensate, calculated with Eq. 1.52. Using the parameters of our experiment, the depth along the x axis is of about 1 µm, which is negligible compared to the transition region of 40 µm as estimated in Fig. 5.9c. Along the tightly-confined direction z instead, where the potential gradient is stronger by a factor of 10, the surface depth is of about 2 µm and covers almost the whole transition region, whose length is reduced to 4 µm.

A step beyond LDA is the inclusion of quantum pressure in the calculation of the condensate density, which is done in the HF theory developed in a harmonic trap, leading to Eq. 1.39. I computed the solution to HF equations in a 3D geometry with our trap parameters for the measured number of atoms and temperature, using the iterative method reported in [70] (technical details in Appendix B). In Fig. 5.14 we plot slices of the solution along the x (a) and z directions (b), compared with the LDA profile at the same values of μ_0 and T (black dashed line). The calculation shows that beyond-LDA terms have a strong effect on the shape of the density distribution where the potential gradients are high, smoothing the corresponding LDA EoS profiles plotted in (c).

Last, we compute the compressibility κ from n and p using Eq. 1.34. In Fig. 5.15 we plot the reduced quantity κ/κ_0, normalized to the zero-temperature value $\kappa_0 = 1/gn^2$, both as a function of the axial coordinate and of T/T_c. The divergence at the transition is still present in HF theory, even thought it is not visible in the plot due to finite numerical resolution. The data qualitatively follow the interacting gas curve, going from $\kappa \sim 0$ to $\kappa = \kappa_0$ across the phase transition, but noise and oscillations in the density profile prevent any quantitative comparison. If we try to reduce the strength of the filtering data operations to gain a steeper profile, the SNR in the plateau region below T_c goes easily below 1, and the signal is completely masked.

The width of the peak, almost 2 µm in the left plot, falls closely below the resolution of a standard imaging setup. Moreover, the feature falls completely within the region where LDA is known to fail, so that it is not even guaranteed that such a sharp feature exists in a trapped condensate, as quantum pressure effects could be responsible for washing out the transition in the compressibility.

Conclusions

Using the PTAI method and the HDR reconstruction technique I developed for this project, we were able to measure the in-situ absolute density of a trapped BEC in the full range, from the center to the thermal wings. A complete image of the optical density allowed to measure the pressure and the density along the trap axis, using respectively the LDA method [142] and the inverse Abel transform.

We fit the obtained profiles to determine the global thermodynamic parameters μ_0 and T. We discussed the feasibility of a fitting scheme which does not rely on the HF model, and found that approximating the tail of the atomic sample with the ideal Bose gas model leads to results consistent with HF theory, provided that the selected data range is sufficiently close tho the edges of the BEC. Also, we took advantage of the combination of the axial pressure and density to fit the two parameters independently.

The pressure and density profiles do not depend on a particular thermodynamic model for the Bose gas, as their calculation is based either on general thermodynamic principles (Gibbs–Duhem relation) or on the symmetries of the system (Abel inversion). Therefore, the $p(n)$ plots in Fig. 5.11a and Fig. 5.12a represent a model-free EoS for the homogeneous interacting Bose gas. On the other hand, since the values of μ_0 and T must be obtained by a fitting procedure, they are dependent on the particular model that we choose to fit with. It is necessary to fit at least the temperature to identify the transition point on the pressure curve, since the pressure is a relatively smooth quantity at the transition, with a discontinuity only in the second derivative (corresponding to the compressibility peak) which is very hard to distinguish measuring the $p(n, T)$ EoS.

We extracted the $\mu(T)$ EoS by plotting the reduced chemical potential $(\mu_0 - V_{ext})/gn$ vs. $T/T_c(n)$. This measurement is a first direct observation of the non-monotonic shape of the chemical potential curve across the BEC phase transition, and contributes to sustain the hypothesis that a peak in the chemical potential is associated with the general normal-to-superfluid phase transition, of which the weakly-interacting Bose gas is one of the many examples.

The comparison of the data with HF theory suffers from a number of limitations, the main one being imaging resolution. The effect of low resolution on the chemical potential plot is to smooth the peak feature and lower its height. As the potential gradient is weaker along the x axis of our trap, the transition region is wide enough to allow us to observe the non-monotonic behavior applying the LDA scheme on the axial density profile. We found agreement between our data and theory including resolution effects on the LDA HF prediction for the EoS curve. Another good aspect of the weak trapping potential along x is that it mitigates the corrections to LDA, which in principle breaks up in the edge regions of the BEC preventing the applicability of our measurement scheme. We evaluated the extent of the corrections by solving the HF equations in harmonic trap, which include beyond-LDA quantum pressure terms in the calculation of the condensate density, and found that such corrections are small along the x axis, while they are very relevant along the tight axis z.

Finally, we calculated the compressibility EoS $\kappa(T)$, but the experimental data are too noisy to be able to observe the presence of a peak at the transition. The above considerations apply even stronger in this case, as the compressibility is seen to recover the constant value κ_0 as soon as one enters the condensed phase, as shown by the LDA HF curves. The peak is narrow and completely contained in the spatial region where LDA cannot be applied. Even if cleaner measurements could help identifying the transition point and determine the value of the compressibility in the BEC phase, we question the possibility of observing the sharp peak across the transition with an

LDA-based measurement in a trapped sample like the one discussed in this work.

Appendix A

Numerical solution of the optical Bloch equations

Writing Eq. 3.3, we assume that the scattering rate R in a multilevel atom has the same dependency on s_0 and Δ as in the two-levels case (Eq. 3.2), and that the effect of light polarization can be summarized, under certain conditions, in a single coefficient α. This coefficient represents then a weighted average of the oscillator strengths of the single $m_F \to m_{F'}$ transitions that contribute to the scattering process.

The calculation of the scattering rate in the general case requires to solve the full system of the OBE, which includes all the atomic levels, all the couplings introduced by laser light, and the decay channels of the excited states. It is convenient to rewrite the OBE in the form of a master equation for the time evolution of the atomic density matrix ρ:

$$\partial_t \rho = -i\left[H_0 + H_{int}, \rho\right] + \frac{\Gamma}{2}\sum_q 2\Sigma_q \rho \Sigma_q^\dagger - \rho\Sigma_q^\dagger\Sigma_q - \Sigma_q^\dagger\Sigma_q\rho\,. \tag{A.1}$$

The atomic states are grouped in the two separate subsets of ground $g = -F, \ldots, F$ and excited $e = -F', \ldots, F'$ states, and the index $q = -1, 0, 1$ labels the light polarizations (corresponding to σ_-, π, σ_+). We notice that this formalism applies to the case of weak magnetic fields, where the hyperfine levels $|F, m_F\rangle$ are well defined. The free atom hamiltonian

$$H_0 = \sum_g \delta\omega_g |g\rangle\langle g| + \sum_e (\delta\omega_e - \Delta)|e\rangle\langle e| \tag{A.2}$$

includes the linear Zeeman frequency shift $\delta\omega_{g,e} = g_F m_F \mu_B B/\hbar$ and the laser detuning Δ, which is defined with respect to the non-shifted transition $|F, m_g = 0\rangle \to |F', m_e = 0\rangle$. Both the RWA interaction hamiltonian H_{int} and the Lindblad term can be expressed in terms of lowering operators

$$\Sigma_q = \sum_{g,e} \langle F, m_g; 1, q | F', m_e\rangle |g\rangle\langle e|\,, \tag{A.3}$$

which express the transition between all the pairs of ground and excited levels coupled by light with polarization q. In the interaction term

$$H_{int} = \frac{1}{2}\sum_q \Omega_q^* \Sigma_q + \Omega_q \Sigma_q^\dagger \tag{A.4}$$

the Rabi frequencies Ω_q are specified for each polarization by

$$\Omega_q = \frac{\langle J||er||J'\rangle E_q}{\hbar} \tag{A.5}$$

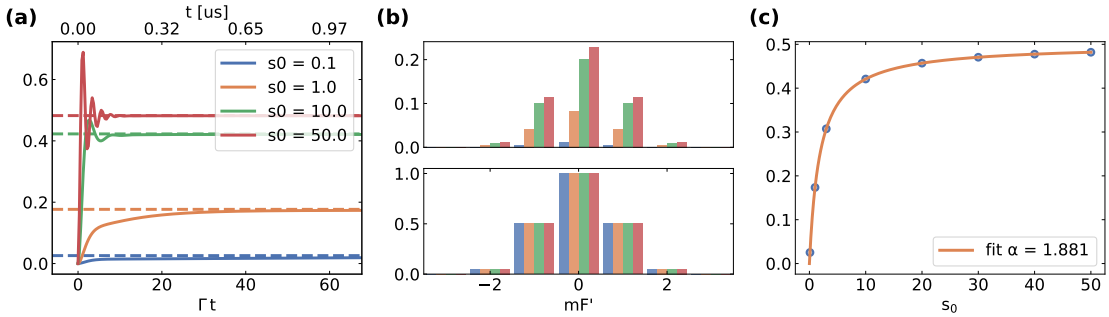

Figure A.1: Solution of the OBE with π polarized light and $B = 4\,\mathrm{G}$, scanning s_0. (a) Total steady-state population vs. time, showing a shorter transient time for higher intensity. (b) Top: histograms of the populations in the excited states. Bottom: Excited populations, normalized to the one in $m_{F'} = 0$. This shows that the relative distribution of the atomic populations is independent of the light intensity. (c) Scattering rate R/Γ, fitted with Eq. 3.3.

where $\langle J||er||J'\rangle$ is the reduced dipole matrix element of the optical transition, and E_q is the amplitude of the q-polarized component of the light electric field. They are related to the total light intensity I by

$$2\sum_q \frac{|\Omega_q|^2}{\Gamma^2} = \frac{I}{I_{sat}}\,. \tag{A.6}$$

Given the definition of $s_0 = I/I_{sat}$, we can specify the light polarization by a vector λ_q (such as $\sum|\lambda_q|^2 = 1$) and rewrite the Rabi frequencies as $\Omega_q = \sqrt{s_0/2}\,\lambda_q\Gamma$.

I numerically computed the time evolution of the system using the Python package `qutip` [132] for the ^{23}Na D2 transitions $F = 2 \longrightarrow F' = 3$, with arbitrary light polarization and in a range of magnetic fields.

For a given polarization, a fixed magnetic field B and $\Delta = 0$, I run simulations scanning the total light intensity s_0. Each simulation returns the time evolution of the atomic density matrix $\rho(t)$, from which the scattering rate at steady state is calculated as $R = \Gamma\sum_e \rho_{ee}$. The result is fitted as a function of s_0 with Eq. 3.3, with α as the fitting parameter. As the OBE do not include atomic motion, the resulting scattering rate does not account for the Doppler shift effect due to probe recoil. Fig. A.1a shows an example of time evolution, plotting the total excited population $\sum\rho_{ee}(t)$ as a functon of time, at a finite magnetic field of 4 G. Fig. A.1c shows the scattering rate R/Γ and the value of α resulting from its fit.

The results do not depend on the initial state of the atomic system, since optical pumping will bring the atoms to the steady distribution with no memory of the initial state. However, the transient time evolution is influenced by the initial conditions and by the probe intensity, and it can take up to several µs to reach the steady state if $s_0 \lesssim 0.1$. To reproduce our experimental case of PTAI imaging, all the simulations are initialized with all the atoms in $|2,-2\rangle$.

When the light is circularly polarized, the system is pumped to cycle between the stretched states $|2,\pm2\rangle$ and $|3,\pm3\rangle$ becoming effectively a closed two-level system. Eq. 3.2 holds at all magnetic fields, and α has a constant value of 1.

For linear polarization, in the steady state the population ends up symmetrically distributed around $m_F = 0$. This symmetry is preserved even at finite magnetic field, since the Zeeman detuning is opposite for states with opposite m_F, but it appears squared in the expression for the excited state populatons. Scanning the probe intensity one varies the total population in the excited states, but not their distribution among the

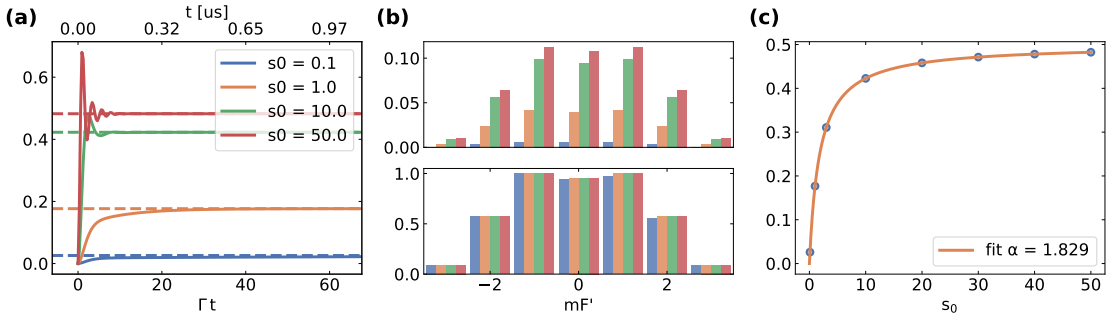

Figure A.2: Same plots as in Fig. A.1, but for $\theta = \pi/6$. The total light intensity is still indicated by s_0, but it is divided in a 75% ($\cos^2\theta$) on π polarization, and 25% on $\sigma_\pm$ (equally distributed). The presence of circularly polarized light produces a non-zero population in the $m_{F'} = \pm 3$ states.

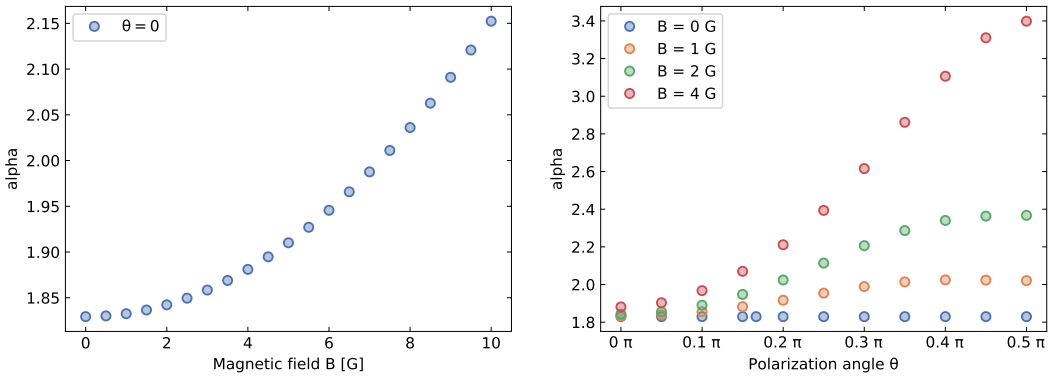

Figure A.3: Left: α as a function of magnetic field B, for π polarized light. Right: α as a function of the polarization angle θ, for different values of magnetic field.

Zeeman sublevels. This can be visualized by plotting a histogram of the ρ_{ee} normalized by the population in $m_{F'} = 0$, as done in Fig. A.1b (bottom).

Fig. A.3a shows the fitted value of α vs. B, where we recover the analytical result 1.829 at zero field [118]. The plot shows that the effect of the magnetic field is a weak quadratic correction, as α remains close to 2 within 5% even at moderate fields.

I also checked the effects of a possible error in the setting of the light polarization, simulating the case where light is sent perpendicular to the magnetic field and linearly polarized, but the polarization is tilted by an angle θ with respect to the field direction. For $\theta = 0$ the light is totally π polarized, while for $\theta = \pi/2$ the light oscillates perpendicular to the field, so it is equally distributed between σ_- and σ_+.

Fig. A.2 shows the same quantities plotted in Fig. A.1, but for $B = 0$ and $\theta = \pi/6$. The presence of circularly polarized components of light produces a non-zero population in the $m_{F'} = \pm 3$ states. The dependency of α on the polarization angle θ is shown in Fig. A.3b. There is no effect from the tilt at zero magnetic field, where α maintains the constant value 1.829, which is physically correct since at zero field the quantization axis of the atomic spin is undefined, and all light polarizations are equivalent. The effect of the misalignment becomes relevant at finite magnetic field.

Appendix B

Solution of HF equations in the harmonic trap

The Hartree–Fock theory for a harmonically trapped gas determines the effective single-particle eigenstates of the system from the (infinite) set of equations in Eq. 1.39. With a semiclassical approximation, the density of thermal particles can be self-consistently calculated, reducing the set of equations to

$$\left[-\frac{\hbar^2}{2m}\nabla^2 + V_{ext}(r) + g(|\psi_0|^2 + 2n_T)\right]\psi_0 = \mu\psi_0\,, \tag{B.1a}$$

$$n_T = \frac{1}{\lambda_T^3} g_{3/2}\left(e^{(\mu - V_{ext}(r) - 2gn/k_BT}\right)\,, \tag{B.1b}$$

$$N = \int (|\psi_0|^2 + n_T)\, d^3r\,, \tag{B.1c}$$

with $n = |\psi_0|^2 + n_T$. These have been already derived in Chap. 1 respectively as Eq. 1.39a, Eq. 1.42 and Eq. 1.40, and I rewrite them here for clarity.

Fixing the values of the number of atoms N and the temperature T, the system can be solved for ψ_0, n_T and μ, which are the condensate wavefunction, the density of thermal atoms, and the chemical potential. The density of condensed atoms is then $n_0 = |\psi_0|^2$.

I set $N = 8.6 \times 10^6$ and $T = 290\,\text{nK}$, measured from the data discussed in Sect. 5.3, and the trap frequencies in V_{ext} to the experimental values (Sect. 5.2.1), and solve the HF equations with the iterative approach described by Giorgini, Pitaevskii, and Stringari [70]:

(i) given n_T, the number of condensed atoms N_0 is calculated as $N_0 = N - \int d^3r\, n_T$. This value is used to fix the normalization of the GPE Eq. B.1a, which is solved for ψ_0 and μ;

(ii) the total density n is updated with the new $|\psi_0|^2$, and used in Eq. B.1b with the temperature T and the updated μ to compute a new thermal density n_T;

(iii) the two steps above are repeated until we reach convergence.

The loop is initialized using the LDA HF profile in Eq. 5.6c for the thermal fraction. The 3D stationary GPE is solved with imaginary time propagation, renormalizing the wavefunction to N_0 at each step. To run the calculation I used the `xmds2` package [143], using a spectral method for the spatial derivatives and a fourth-order Runge–Kutta method for the time propagation, with fixed timestep Δt. The problem is reduced to two dimensions by setting $\omega_y = \omega_z$ and working in cylindrical coordinates, and solved only in the $x > 0$ half space by enforcing the wavefunction to be even in x. At each timestep,

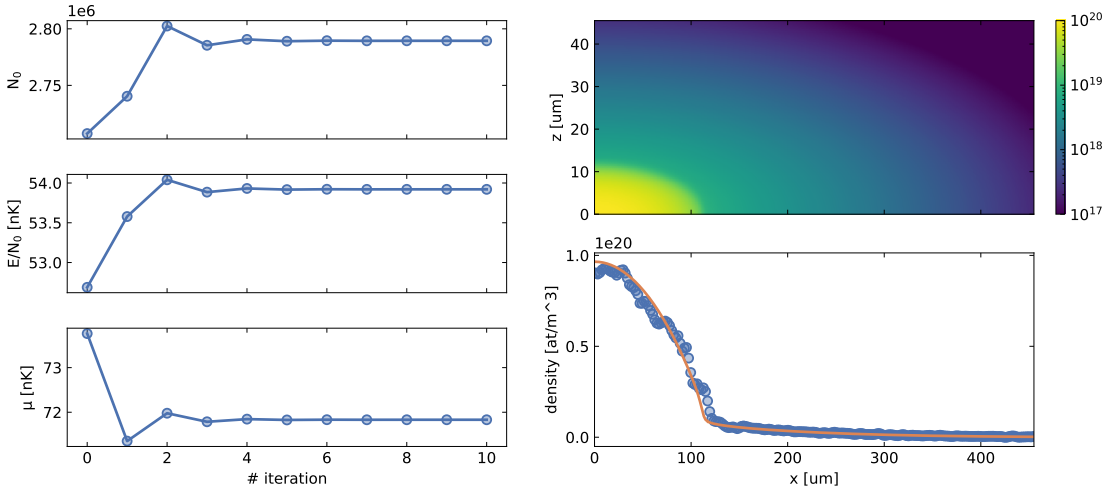

Figure B.1: Left: convergence of the HF solution. From top to bottom: number of condensed atoms N_0, energy per BEC particle E/N_0, chemical potential μ. Top right: a 2D plot of the final density distribution. The colormap is logarithmic, to highlight the different density between the condensed and the thermal fraction. Bottom right: a slice along the x axis of the calculated distribution on top of the experimental density data.

the wavefunction is evolved from $\psi_0^{(n)}$ to $\psi_0^{(n+1)}$, and the chemical potential is calculated as

$$\mu^{(n+1)} = \frac{1}{\Delta t}\left(1 - \frac{\int \psi_0^{(n)}\psi_0^{(n+1)}\, d^3r}{\int |\psi_0^{(n)}|^2\, d^3r}\right) \tag{B.2}$$

before renormalizing $\psi_0^{(n+1)}$ to integrate the next step.

The convergence of the GPE to the stationary solution is monitored reading both the values of μ and of the total energy E, calculated with Eq. 1.2. The asymptotic values approximately agree with the relation $E = (5/7)\mu N_0$, which is valid in the Thomas–Fermi limit, and to which we expect corrections due to both the finite surface of the BEC and the extra potential energy of the thermal fraction. The convergence of the total calculation is checked by monitoring μ and N_0, which become stable in a small number of iterations.

Fig. B.1 shows the parameters E/N_0, N_0 and μ at each iteration step. The final value of the chemical potential is 71.83 nK, slightly different than the value obtained by fitting the data (listed in Table 5.1). The calculated density distribution agrees very well with the measured density profile.

Bibliography

[1] S. N. Bose. "Plancks Gesetz und Lichtquantenhypothese". *Zeitschrift für Phys.* 26.1 (1924). DOI: 10.1007/BF01327326 (Cited on page 1).

[2] A. Einstein. "Quantentheorie des einatomigen idealen Gases". *Albert Einstein Akad.* Vol. V. Weinheim, FRG: Wiley-VCH Verlag GmbH & Co. KGaA, 2006. DOI: 10.1002/3527608958.ch27 (Cited on page 1).

[3] P. Kapitza. "Viscosity of Liquid Helium below the λ-Point". *Nature* 141.3558 (1938). DOI: 10.1038/141074a0 (Cited on page 1).

[4] J. F. Allen and A. D. Misener. "Flow Phenomena in Liquid Helium II". *Nature* 142.3597 (1938). DOI: 10.1038/142643a0 (Cited on page 1).

[5] M. H. Anderson et al. "Observation of Bose-Einstein Condensation in a Dilute Atomic Vapor". *Science (80-.).* 269.5221 (1995). DOI: 10.1126/science.269.5221.198 (Cited on pages 1, 21).

[6] K. B. Davis et al. "Bose-Einstein Condensation in a Gas of Sodium Atoms". *Phys. Rev. Lett.* 75.22 (1995). DOI: 10.1103/PhysRevLett.75.3969 (Cited on pages 1, 21).

[7] T. Hänsch and A. Schawlow. "Cooling of gases by laser radiation". *Opt. Commun.* 13.1 (1975). DOI: 10.1016/0030-4018(75)90159-5 (Cited on pages 1, 21).

[8] D. E. Pritchard. "Cooling Neutral Atoms in a Magnetic Trap for Precision Spectroscopy". *Phys. Rev. Lett.* 51.15 (1983). DOI: 10.1103/PhysRevLett.51.1336 (Cited on page 1).

[9] E. L. Raab et al. "Trapping of Neutral Sodium Atoms with Radiation Pressure". *Phys. Rev. Lett.* 59.23 (1987). DOI: 10.1103/PhysRevLett.59.2631 (Cited on page 1).

[10] L. P. Pitaevskii. "Vortex lines in an imperfect Bose gas". *Sov. Phys. JETP* 13.2 (1961) (Cited on pages 2, 5).

[11] E. P. Gross. "Structure of a quantized vortex in boson systems". *Nuovo Cim.* 20.3 (1961). DOI: 10.1007/BF02731494 (Cited on page 2).

[12] N. N. Bogolyubov. "On the theory of superfluidity". *J. Phys. USSR* 11 (1947) (Cited on pages 2, 4).

[13] V. L. Ginzburg and L. P. Pitaevskii. "On the theory of superfluidity". *Sov. Phys. JETP* 7.5 (1958) (Cited on page 2).

[14] F. Dalfovo et al. "Theory of Bose-Einstein condensation in trapped gases". *Rev. Mod. Phys.* 71.3 (1999). DOI: 10.1103/RevModPhys.71.463 (Cited on pages 3, 17).

[15] L. D. Landau. "The Theory of Superfluidity of Helium II". *J. Phys. USSR* 5 (1941) (Cited on page 4).

[16] P. G. Saffman. *Vortex Dynamics*. Cambridge Monographs on Mechanics. Cambridge University Press, 1992. ISBN: 9780521420587. URL: https://books.google.it/books?id=ksktDE0yVzcC (Cited on page 5).

[17] C. J. Pethick and H. Smith. *Bose–Einstein Condensation in Dilute Gases*. 2nd ed. Cambridge University Press, 2008. ISBN: 9780511802850. DOI: 10.1017/CBO9780511802850 (Cited on pages 5, 14).

[18] V. L. Berezinsky. "Destruction of Long-range Order in One-dimensional and Two-dimensional Systems Possessing a Continuous Symmetry Group. II. Quantum Systems." *Sov. Phys. JETP* 34.3 (1972) (Cited on page 6).

[19] J. M. Kosterlitz and D. J. Thouless. "Ordering, metastability and phase transitions in two-dimensional systems". *J. Phys. C Solid State Phys.* 6.7 (1973). DOI: 10.1088/0022-3719/6/7/010 (Cited on page 6).

[20] P. C. Hohenberg. "Existence of Long-Range Order in One and Two Dimensions". *Phys. Rev.* 158.2 (1967). DOI: 10.1103/PhysRev.158.383 (Cited on page 6).

[21] A. Aftalion and T. Riviere. "Vortex energy and vortex bending for a rotating Bose-Einstein condensate". *Phys. Rev. A* 64.4 (2001). DOI: 10.1103/PhysRevA.64.043611 (Cited on page 6).

[22] C. Raman et al. "Vortex Nucleation in a Stirred Bose-Einstein Condensate". *Phys. Rev. Lett.* 87.21 (2001). DOI: 10.1103/PhysRevLett.87.210402 (Cited on page 6).

[23] S. Donadello et al. "Observation of Solitonic Vortices in Bose-Einstein Condensates". *Phys. Rev. Lett.* 113.6 (2014). DOI: 10.1103/PhysRevLett.113.065302 (Cited on pages 6, 9).

[24] M. C. Tsatsos et al. "Quantum turbulence in trapped atomic Bose–Einstein condensates". *Phys. Rep.* 622.3-4 (2016). DOI: 10.1016/j.physrep.2016.02.003 (Cited on page 6).

[25] N. G. Parker et al. "Quantum turbulence in atomic Bose-Einstein condensates". *Univers. Themes Bose-Einstein Condens.* (2017). DOI: 10.1017/9781316084366.019 (Cited on page 6).

[26] A. Muñoz Mateo and J. Brand. "Chladni solitons and the onset of the snaking instability for dark solitons in confined superfluids". *Phys. Rev. Lett.* 113.25 (2014). DOI: 10.1103/PhysRevLett.113.255302 (Cited on page 6).

[27] J. Brand and W. P. Reinhardt. "Solitonic vortices and the fundamental modes of the "snake instability": Possibility of observation in the gaseous Bose-Einstein condensate". *Phys. Rev. A* 65.4 (2002). DOI: 10.1103/PhysRevA.65.043612 (Cited on page 6).

[28] M. Tylutki et al. "Solitonic vortices in Bose–Einstein condensates". *Eur. Phys. J. Spec. Top.* 224.3 (2015). DOI: 10.1140/epjst/e2015-02389-7 (Cited on pages 6, 7).

[29] E. Lundh, C. J. Pethick, and H. Smith. "Vortices in Bose-Einstein-condensed atomic clouds". *Phys. Rev. A* 58.6 (1998). DOI: 10.1103/PhysRevA.58.4816 (Cited on pages 7, 9, 45, 49).

[30] R. J. Donnelly. *Quantized vortices in helium II*. Vol. 2. Cambridge University Press, 1991. ISBN: 9780521324007. URL: https://books.google.it/books?id=Qg-%7B%5C%7D5C%7B%5C_%7Dv%7B%5C%7D5C%7B%5C_%7DdzhicC (Cited on page 8).

[31] H. E. Hall and W. F. Vinen. "The rotation of liquid helium II II. The theory of mutual friction in uniformly rotating helium II". *Proc. R. Soc. London. Ser. A. Math. Phys. Sci.* 238.1213 (1956). DOI: 10.1098/rspa.1956.0215 (Cited on page 8).

[32] E. J. Yarmchuk, M. J. V. Gordon, and R. E. Packard. "Observation of Stationary Vortex Arrays in Rotating Superfluid Helium". *Phys. Rev. Lett.* 43.3 (1979). DOI: 10.1103/PhysRevLett.43.214 (Cited on page 8).

[33] G. P. Bewley, D. P. Lathrop, and K. R. Sreenivasan. "Visualization of quantized vortices". *Nature* 441.7093 (2006). DOI: 10.1038/441588a (Cited on page 8).

[34] D. E. Zmeev et al. "Excimers He2 as Tracers of Quantum Turbulence in 4He in the T = 0 Limit". *Phys. Rev. Lett.* 110.17 (2013). DOI: 10.1103/PhysRevLett.110.175303 (Cited on page 8).

[35] A. L. Fetter. "Rotating trapped Bose-Einstein condensates". *Rev. Mod. Phys.* 81.2 (2009). DOI: 10.1103/RevModPhys.81.647 (Cited on page 8).

[36] K. W. Madison et al. "Vortex formation in a stirred bose-einstein condensate". *Phys. Rev. Lett.* 84.5 (2000). DOI: 10.1103/PhysRevLett.84.806 (Cited on page 8).

[37] J. R. Abo-Shaeer et al. "Observation of Vortex Lattices in Bose-Einstein Condensates". *Science (80-.).* 292.5516 (2001). DOI: 10.1126/science.1060182 (Cited on page 8).

[38] E. Hodby et al. "Vortex Nucleation in Bose-Einstein Condensates in an Oblate, Purely Magnetic Potential". *Phys. Rev. Lett.* 88.1 (2001). DOI: 10.1103/PhysRevLett.88.010405 (Cited on page 8).

[39] A. Rakonjac et al. "Measuring the disorder of vortex lattices in a Bose-Einstein condensate". *Phys. Rev. A* 93.1 (2016). DOI: 10.1103/PhysRevA.93.013607 (Cited on page 8).

[40] S. Tung, V. Schweikhard, and E. A. Cornell. "Observation of vortex pinning in Bose-Einstein condensates". *Phys. Rev. Lett.* 97.24 (2006). DOI: 10.1103/PhysRevLett.97.240402 (Cited on page 8).

[41] E. C. Samson et al. "Deterministic creation, pinning, and manipulation of quantized vortices in a Bose-Einstein condensate". *Phys. Rev. A* 93.2 (2016). DOI: 10.1103/PhysRevA.93.023603 (Cited on page 8).

[42] W. J. Kwon et al. "Critical Velocity for Vortex Shedding in a Bose-Einstein Condensate". 053615.May (2015). DOI: 10.1103/PhysRevA.91.053615 (Cited on page 8).

[43] M. R. Matthews et al. "Vortices in a Bose-Einstein Condensate". *Phys. Rev. Lett.* 83.13 (1999). DOI: 10.1103/PhysRevLett.83.2498 (Cited on page 8).

[44] B. P. Anderson et al. "Watching Dark Solitons Decay into Vortex Rings in a Bose-Einstein Condensate". *Phys. Rev. Lett.* 86.14 (2001). DOI: 10.1103/PhysRevLett.86.2926 (Cited on page 9).

[45] M. Andersen et al. "Quantized Rotation of Atoms from Photons with Orbital Angular Momentum". *Phys. Rev. Lett.* 97.17 (2006). DOI: 10.1103/PhysRevLett.97.170406 (Cited on page 9).

[46] W. Zurek. "Cosmological experiments in condensed matter systems". *Phys. Rep.* 276.4 (1996). DOI: 10.1016/S0370-1573(96)00009-9 (Cited on page 9).

[47] A. del Campo, T. W. B. Kibble, and W. H. Zurek. "Causality and non-equilibrium second-order phase transitions in inhomogeneous systems". *J. Phys. Condens. Matter* 25.40 (2013). DOI: 10.1088/0953-8984/25/40/404210 (Cited on pages 9, 47).

[48] C. N. Weiler et al. "Spontaneous vortices in the formation of Bose–Einstein condensates". *Nature* 455.7215 (2008). DOI: 10.1038/nature07334 (Cited on page 9).

[49] S. Donadello et al. "Creation and counting of defects in a temperature-quenched Bose-Einstein condensate". *Phys. Rev. A* 94.2 (2016). DOI: 10.1103/PhysRevA.94.023628 (Cited on page 9).

[50] L. Chomaz et al. "Emergence of coherence via transverse condensation in a uniform quasi-two-dimensional Bose gas". *Nat. Commun.* 6.1 (2015). DOI: 10.1038/ncomms7162 (Cited on page 9).

[51] D. R. Scherer et al. "Vortex Formation by Merging of Multiple Trapped Bose-Einstein Condensates". *Phys. Rev. Lett.* 98.11 (2007). DOI: 10.1103/PhysRevLett.98.110402 (Cited on page 9).

[52] M. Aidelsburger et al. "Relaxation Dynamics in the Merging of N Independent Condensates". *Phys. Rev. Lett.* 119.19 (2017). DOI: 10.1103/PhysRevLett.119.190403 (Cited on page 9).

[53] V. Schweikhard, S. Tung, and E. A. Cornell. "Vortex Proliferation in the Berezinskii-Kosterlitz-Thouless Regime on a Two-Dimensional Lattice of Bose-Einstein Condensates". *Phys. Rev. Lett.* 99.3 (2007). DOI: 10.1103/PhysRevLett.99.030401 (Cited on page 9).

[54] I.-K. Liu et al. "Dynamical equilibration across a quenched phase transition in a trapped quantum gas". *Commun. Phys.* 1.1 (2018). DOI: 10.1038/s42005-018-0023-6 (Cited on page 9).

[55] G. Lamporesi et al. "Spontaneous creation of Kibble–Zurek solitons in a Bose–Einstein condensate". *Nat. Phys.* 9.10 (2013). DOI: 10.1038/nphys2734 (Cited on page 9).

[56] K. E. Wilson et al. "In situ imaging of vortices in Bose-Einstein condensates". *Phys. Rev. A - At. Mol. Opt. Phys.* 91.2 (2015). DOI: 10.1103/PhysRevA.91.023621 (Cited on page 9).

[57] F. Dalfovo and M. Modugno. "Free expansion of Bose-Einstein condensates with quantized vortices". *Phys. Rev. A* 61.2 (2000). DOI: 10.1103/PhysRevA.61.023605 (Cited on pages 9, 45).

[58] S. W. Seo, J.-y. Choi, and Y. Shin. "Free expansion of quasi-2D Bose-Einstein condensates with quantized vortices". *J. Korean Phys. Soc.* 64.1 (2014). DOI: 10.3938/jkps.64.53 (Cited on page 9).

[59] F. Dalfovo et al. "Optical Visibility and Core Structure of Vortex Filaments in a Bosonic Superfluid". *J. Exp. Theor. Phys.* 127.5 (2018). DOI: 10.1134/S1063776118110018 (Cited on pages 9, 48, 52, 53).

[60] R. J. Ballagh, K. Burnett, and T. F. Scott. "Theory of an output coupler for bose-einstein condensed atoms". *Phys. Rev. Lett.* 78.9 (1997). DOI: 10.1103/PhysRevLett.78.1607 (Cited on page 9).

[61] D. V. Freilich et al. "Real-Time Dynamics of Single Vortex Lines and Vortex Dipoles in a Bose-Einstein Condensate". *Science (80-.).* 329.5996 (2010). DOI: 10.1126/science.1191224 (Cited on pages 9, 56).

[62] A. Ramanathan et al. "Partial-transfer absorption imaging: A versatile technique for optimal imaging of ultracold gases". *Rev. Sci. Instrum.* 83.8 (2012). DOI: 10.1063/1.4747163 (Cited on pages 9, 56).

[63] S. Serafini et al. "Dynamics and Interaction of Vortex Lines in an Elongated Bose-Einstein Condensate". *Phys. Rev. Lett.* 115.17 (2015). DOI: 10.1103/PhysRevLett.115.170402 (Cited on page 9).

[64] R. N. Bisset et al. "Observation of a spinning top in a Bose-Einstein condensate". *Phys. Rev. A* 96.5 (2017). DOI: 10.1103/PhysRevA.96.053605 (Cited on page 9).

[65] S. Serafini et al. "Vortex Reconnections and Rebounds in Trapped Atomic Bose-Einstein Condensates". *Phys. Rev. X* 7.2 (2017). DOI: 10.1103/PhysRevX.7.021031 (Cited on pages 9, 50).

[66] G. Jaeger. "The Ehrenfest Classification of Phase Transitions: Introduction and Evolution". *Arch. Hist. Exact Sci.* 53.1 (1998). DOI: 10.1007/s004070050021 (Cited on page 10).

[67] D. J. Papoular et al. "Increasing Quantum Degeneracy by Heating a Superfluid". *Phys. Rev. Lett.* 109.8 (2012). DOI: 10.1103/PhysRevLett.109.084501 (Cited on pages 10, 17).

[68] L. Lewin. *Polylogarithms and associated functions*. North Holland, 1981. ISBN: 9780444005502. URL: https://books.google.it/books?id=yETvAAAAMAAJ (Cited on page 11).

[69] D. A. Huse and E. D. Siggia. "The density distribution of a weakly interacting bose gas in an external potential". *J. Low Temp. Phys.* 46.1-2 (1982). DOI: 10.1007/BF00655448 (Cited on page 14).

[70] S. Giorgini, L. P. Pitaevskii, and S. Stringari. "Condensate fraction and critical temperature of a trapped interacting Bose gas". *Phys. Rev. A* 54.6 (1996). DOI: 10.1103/PhysRevA.54.R4633 (Cited on pages 14, 72, 79).

[71] M. Holzmann, W. Krauth, and M. Naraschewski. "Precision Monte Carlo test of the Hartree-Fock approximation for a trapped Bose gas". *Phys. Rev. A* 59.4 (1999). DOI: 10.1103/PhysRevA.59.2956 (Cited on page 14).

[72] N. Prokof'ev, O. Ruebenacker, and B. Svistunov. "Weakly interacting Bose gas in the vicinity of the normal-fluid–superfluid transition". *Phys. Rev. A* 69.5 (2004). DOI: 10.1103/PhysRevA.69.053625 (Cited on pages 14, 71).

[73] C.-H. Cheng and S.-K. Yip. "Trapped resonant fermions above the superfluid transition temperature". *Phys. Rev. B* 75.1 (2007). DOI: 10.1103/PhysRevB.75.014526 (Cited on page 15).

[74] T.-L. Ho and Q. Zhou. "Obtaining the phase diagram and thermodynamic quantities of bulk systems from the densities of trapped gases". *Nat. Phys.* 6.2 (2010). DOI: 10.1038/nphys1477 (Cited on pages 15, 55, 65).

[75] F. Dalfovo, L. P. Pitaevskii, and S. Stringari. "Order parameter at the boundary of a trapped Bose gas". *Phys. Rev. A* 54.5 (1996). DOI: 10.1103/PhysRevA.54.4213 (Cited on page 16).

[76] E. Lundh, C. J. Pethick, and H. Smith. "Zero-temperature properties of a trapped Bose-condensed gas: Beyond the Thomas-Fermi approximation". *Phys. Rev. A* 55.3 (1997). DOI: 10.1103/PhysRevA.55.2126 (Cited on page 16).

[77] L. Pitaevskii and S. Stringari. *Bose-Einstein Condensation and Superfluidity*. Oxford University Press, 2016. ISBN: 9780198758884. DOI: 10.1093/acprof:oso/9780198758884.001.0001 (Cited on page 16).

[78] V. Arp. "He4 State Equation Below 0.8 K". *Int. J. Thermophys.* 26.5 (2005). DOI: 10.1007/s10765-005-8098-1 (Cited on page 17).

[79] A. Griffin. "Conserving and gapless approximations for an inhomogeneous Bose gas at finite temperatures". *Phys. Rev. B* 53.14 (1996). DOI: 10.1103/PhysRevB.53.9341 (Cited on page 17).

[80] S. Giorgini, L. P. Pitaevskii, and S. Stringari. "Thermodynamics of a Trapped Bose-Condensed Gas". *J. Low Temp. Phys.* 109.1-2 (1997). DOI: 10.1007/s10909-005-0089-x (Cited on page 17).

[81] V. Romero-Rochín and V. S. Bagnato. "Thermodynamics of an ideal gas of bosons harmonically trapped: equation of state and susceptibilities". *Brazilian J. Phys.* 35.3a (2005). DOI: 10.1590/S0103-97332005000400004 (Cited on page 17).

[82] V. Romero-Rochìn. "Equation of State of an Interacting Bose Gas Confined by a Harmonic Trap: The Role of the "Harmonic" Pressure". *Phys. Rev. Lett.* 94.13 (2005). DOI: 10.1103/PhysRevLett.94.130601 (Cited on page 17).

[83] F. Gerbier et al. "Experimental study of the thermodynamics of an interacting trapped Bose-Einstein condensed gas". *Phys. Rev. A* 70.1 (2004). DOI: 10.1103/PhysRevA.70.013607 (Cited on page 17).

[84] R. P. Smith et al. "Effects of Interactions on the Critical Temperature of a Trapped Bose Gas". *Phys. Rev. Lett.* 106.25 (2011). DOI: 10.1103/PhysRevLett.106.250403 (Cited on page 17).

[85] V. Romero-Rochìn et al. "Observation of Bose-Einstein condensation in an atomic trap in terms of macroscopic thermodynamic parameters". *Phys. Rev. A* 85.2 (2012). DOI: 10.1103/PhysRevA.85.023632 (Cited on page 17).

[86] M. A. Kristensen et al. "Observation of Atom Number Fluctuations in a Bose-Einstein Condensate". *Phys. Rev. Lett.* 122.16 (2019). DOI: 10.1103/PhysRevLett.122.163601 (Cited on page 17).

[87] A. L. Gaunt et al. "Bose-Einstein Condensation of Atoms in a Uniform Potential". *Phys. Rev. Lett.* 110.20 (2013). DOI: 10.1103/PhysRevLett.110.200406 (Cited on page 17).

[88] I. Gotlibovych et al. "Observing properties of an interacting homogeneous Bose-Einstein condensate: Heisenberg-limited momentum spread, interaction energy, and free-expansion dynamics". *Phys. Rev. A* 89.6 (2014). DOI: 10.1103/PhysRevA.89.061604 (Cited on page 17).

[89] C.-L. Hung et al. "Observation of scale invariance and universality in two-dimensional Bose gases". *Nature* 470.7333 (2011). DOI: 10.1038/nature09722 (Cited on page 17).

[90] R. Desbuquois et al. "Determination of Scale-Invariant Equations of State without Fitting Parameters: Application to the Two-Dimensional Bose Gas Across the Berezinskii-Kosterlitz-Thouless Transition". *Phys. Rev. Lett.* 113.2 (2014). DOI: 10.1103/PhysRevLett.113.020404 (Cited on page 17).

[91] R. J. Fletcher et al. "Connecting Berezinskii-Kosterlitz-Thouless and BEC Phase Transitions by Tuning Interactions in a Trapped Gas". *Phys. Rev. Lett.* 114.25 (2015). DOI: 10.1103/PhysRevLett.114.255302 (Cited on page 17).

[92] Y. Ohashi and A. Griffin. "BCS-BEC Crossover in a Gas of Fermi Atoms with a Feshbach Resonance". *Phys. Rev. Lett.* 89.13 (2002). DOI: 10.1103/PhysRevLett.89.130402 (Cited on page 17).

[93] M. Horikoshi et al. "Measurement of Universal Thermodynamic Functions for a Unitary Fermi Gas". *Science (80-.).* 327.5964 (2010). DOI: 10.1126/science.1183012 (Cited on page 17).

[94] S. Nascimbène et al. "Exploring the thermodynamics of a universal Fermi gas". *Nature* 463.7284 (2010). DOI: 10.1038/nature08814 (Cited on page 17).

[95] H. Hu, X.-J. Liu, and P. D. Drummond. "Comparison between theory and experiment for universal thermodynamics of a homogeneous, strongly correlated Fermi gas". *Phys. Rev. A* 83.6 (2011). DOI: 10.1103/PhysRevA.83.063610 (Cited on page 17).

[96] A. Amico. "Measurement of the Equation of State of superfluid Fermi gases of 6Li atoms". MA thesis. University of Florence, 2015 (Cited on pages 17, 65).

[97] M. J. H. Ku et al. "Revealing the Superfluid Lambda Transition in the Universal Thermodynamics of a Unitary Fermi Gas". *Science (80-.).* 335.6068 (2012). DOI: 10.1126/science.1214987 (Cited on pages 17, 65).

[98] S. Nascimbène et al. "The equation of state of ultracold Bose and Fermi gases: a few examples". *New J. Phys.* 12.10 (2010). DOI: 10.1088/1367-2630/12/10/103026 (Cited on pages 17, 67).

[99] N. Navon et al. "Dynamics and Thermodynamics of the Low-Temperature Strongly Interacting Bose Gas". *Phys. Rev. Lett.* 107.13 (2011). DOI: 10.1103/PhysRevLett.107.135301 (Cited on page 17).

[100] M. Horikoshi and M. Kuwata-Gonokami. "Cold atom quantum simulator for dilute neutron matter". *Int. J. Mod. Phys. E* (2019). DOI: 10.1142/S0218301319300017 (Cited on page 17).

[101] T. Nicholson et al. "Systematic evaluation of an atomic clock at $2 \times 10-18$ total uncertainty". *Nat. Commun.* 6.1 (2015). DOI: 10.1038/ncomms7896 (Cited on page 21).

[102] K. Wright et al. "Benchmarking an 11-qubit quantum computer". *Arxiv Prepr.* (2019). arXiv: 1903.08181 (Cited on page 21).

[103] G. Lamporesi et al. "Compact high-flux source of cold sodium atoms". *Rev. Sci. Instrum.* 84.6 (2013). DOI: 10.1063/1.4808375 (Cited on pages 21, 23).

[104] D. A. Steck. *Sodium D Line Data*. Revision 2.1.4. 2010. URL: http://steck.us/alkalidata (Cited on page 22).

[105] T. G. Tiecke et al. "High-flux two-dimensional magneto-optical-trap source for cold lithium atoms". *Phys. Rev. A* 80.1 (2009). DOI: 10.1103/PhysRevA.80.013409 (Cited on page 22).

[106] A. Toffali. "Production of ultracold Sodium and Potassium atomic mixture in an optical dipole trap". PhD thesis. University of Trento, 2013 (Cited on page 22).

[107] W. Ketterle et al. "High densities of cold atoms in a dark spontaneous-force optical trap". *Phys. Rev. Lett.* 70.15 (1993). DOI: 10.1103/PhysRevLett.70.2253 (Cited on pages 22, 30).

[108] G. Colzi et al. "Sub-Doppler cooling of sodium atoms in gray molasses". *Phys. Rev. A* 93.2 (2016). DOI: 10.1103/PhysRevA.93.023421 (Cited on pages 22, 30).

[109] L. Ricci et al. "A compact grating-stabilized diode laser system for atomic physics". *Opt. Commun.* 117.5-6 (1995). DOI: 10.1016/0030-4018(95)00146-Y (Cited on page 24).

[110] D. J. Thompson and R. E. Scholten. "Narrow linewidth tunable external cavity diode laser using wide bandwidth filter". *Rev. Sci. Instrum.* 83.2 (2012). DOI: 10.1063/1.3687441 (Cited on page 24).

[111] E. S. Polzik and H. J. Kimble. "Frequency doubling with KNbO_3 in an external cavity". *Opt. Lett.* 16.18 (1991). DOI: 10.1364/OL.16.001400 (Cited on page 24).

[112] Y. Feng et al. "39 W Narrow Linewidth Raman Fiber Amplifier with Frequency Doubling to 26.5 W at 589 nm". *Front. Opt. 2009/Laser Sci. XXV/Fall 2009 OSA Opt. Photonics Tech. Dig.* Washington, D.C.: OSA, 2009. DOI: 10.1364/FIO.2009.PDPA4 (Cited on page 24).

[113] A. Franzen. *ComponentLibrary: a free vector graphics library for optics*. 2006. URL: http://www.gwoptics.org/ComponentLibrary/. License: Creative Commons BY-NC 3.0 (Cited on page 26).

[114] S. Serafini. "Dynamics of Vortices and their Interactions in Bose-Einstein Condensates". PhD thesis. University of Trento, 2016 (Cited on page 27).

[115] S. Donadello. "Observation of the Kibble–Zurek mechanism in a bosonic gas". PhD thesis. University of Trento, 2016 (Cited on page 28).

[116] P. T. Starkey et al. "A scripted control system for autonomous hardware-timed experiments". *Rev. Sci. Instrum.* 84.8 (2013). DOI: 10.1063/1.4817213 (Cited on page 29).

[117] C. Cohen-Tannoudji, J. Dupont-Roc, and G. Grynberg. *Atom-photon interactions: basic processes and applications*. Wiley-Interscience publication. J. Wiley, 1992. ISBN: 9780471293361. URL: https://books.google.it/books?id=m7gPAQAAMAAJ (Cited on page 33).

[118] B. Gao. "Effects of Zeeman degeneracy on the steady-state properties of an atom interacting with a near-resonant laser field: Analytic results". *Phys. Rev. A* 48.3 (1993). DOI: 10.1103/PhysRevA.48.2443 (Cited on pages 34, 43, 77).

[119] M. Horikoshi et al. "Appropriate Probe Condition for Absorption Imaging of Ultracold 6 Li Atoms". *J. Phys. Soc. Japan* 86.10 (2017). DOI: 10.7566/JPSJ.86.104301 (Cited on pages 36, 43).

[120] S. P. Rath et al. "Equilibrium state of a trapped two-dimensional Bose gas". *Phys. Rev. A* 82.1 (2010). DOI: 10.1103/PhysRevA.82.013609 (Cited on page 36).

[121] L. Chomaz et al. "Absorption imaging of a quasi-two-dimensional gas: a multiple scattering analysis". *New J. Phys.* 14.5 (2012). DOI: 10.1088/1367-2630/14/5/055001 (Cited on page 36).

[122] L. Corman et al. "Transmission of near-resonant light through a dense slab of cold atoms". *Phys. Rev. A* 96.5 (2017). DOI: 10.1103/PhysRevA.96.053629 (Cited on page 36).

[123] J. Dalibard and C. Cohen-Tannoudji. "Atomic motion in laser light: connection between semiclassical and quantum descriptions". *J. Phys. B At. Mol. Phys.* 18.8 (1985). DOI: 10.1088/0022-3700/18/8/019 (Cited on page 36).

[124] J. Dalibard. "Atomic Brownian Motion in a Light Wave". *Phys. Scr.* T12.T12 (1986). DOI: 10.1088/0031-8949/1986/T12/004 (Cited on page 36).

[125] C. F. Ockeloen et al. "Detection of small atom numbers through image processing". *Phys. Rev. A* 82.6 (2010). DOI: 10.1103/PhysRevA.82.061606 (Cited on page 37).

[126] *Stingray Technical Manual*. English. Version 4.6.6. Allied Vision Technologies GmbH. URL: https://www.alliedvision.com/fileadmin/content/documents/products/cameras/Stingray/techman/Stingray_TechMan_en.pdf (Cited on page 38).

[127] O. Morice, Y. Castin, and J. Dalibard. "Refractive index of a dilute Bose gas". *Phys. Rev. A* 51.5 (1995). DOI: 10.1103/PhysRevA.51.3896 (Cited on page 39).

[128] W. Ketterle, D. S. Durfee, and D. M. Stamper-Kurn. "Making, probing and understanding Bose-Einstein condensates". *Proc. Int. Sch. Phys. "Enrico Fermi"*. Ed. by C. W. M. Inguscio, S. Stringari. 1999. DOI: 10.3254/978-1-61499-225-7-67 (Cited on page 39).

[129] P. B. Wigley et al. "Non-destructive shadowgraph imaging of ultra-cold atoms". *Opt. Lett.* 41.20 (2016). DOI: 10.1364/OL.41.004795 (Cited on page 39).

[130] G. Reinaudi et al. "Strong saturation absorption imaging of dense clouds of ultracold atoms". *Opt. Lett.* 32.21 (2007). DOI: 10.1364/OL.32.003143 (Cited on page 43).

[131] K. Hueck et al. "Calibrating high intensity absorption imaging of ultracold atoms". *Opt. Express* 25.8 (2017). DOI: 10.1364/OE.25.008670 (Cited on page 42).

[132] J. Johansson, P. Nation, and F. Nori. "QuTiP 2: A Python framework for the dynamics of open quantum systems". *Comput. Phys. Commun.* 184.4 (2013). DOI: 10.1016/j.cpc.2012.11.019 (Cited on pages 43, 76).

[133] S. Knoop et al. "Feshbach spectroscopy and analysis of the interaction potentials of ultracold sodium". *Phys. Rev. A* 83.4 (2011). DOI: 10.1103/PhysRevA.83.042704 (Cited on page 46).

[134] M.-O. Mewes et al. "Output Coupler for Bose-Einstein Condensed Atoms". *Phys. Rev. Lett.* 78.4 (1997). DOI: 10.1103/PhysRevLett.78.582 (Cited on page 56).

[135] A. Ramanathan et al. "Superflow in a Toroidal Bose-Einstein Condensate: An Atom Circuit with a Tunable Weak Link". *Phys. Rev. Lett.* 106.13 (2011). DOI: 10.1103/PhysRevLett.106.130401 (Cited on page 56).

[136] P. Holoborodko. *Smooth Noise Robust Differentiators*. 2008. URL: http://www.holoborodko.com/pavel/numerical-methods/numerical-derivative/smooth-low-noise-differentiators/ (Cited on page 65).

[137] N. H. Abel. "Auflösung einer mechanischen Aufgabe". *J. für die reine und Angew. Math.* 1 (1826). URL: http://eudml.org/doc/183021 (Cited on page 65).

[138] J. R. Gascooke. "Energy Transfer in Polyatomic-Rare Gas Collisions and Van Der Waals Molecule Dissociation". PhD thesis. Flinders University, 2000. URL: https://github.com/PyAbel/abel%7B%5C_%7Dinfo (Cited on page 65).

[139] A. Vogler et al. "Thermodynamics of strongly correlated one-dimensional Bose gases". *Phys. Rev. A* 88.3 (2013). DOI: 10.1103/PhysRevA.88.031603 (Cited on page 65).

[140] E. W. Hansen and P.-L. Law. "Recursive methods for computing the Abel transform and its inverse". *J. Opt. Soc. Am. A* 2.4 (1985). DOI: 10.1364/JOSAA.2.000510 (Cited on page 66).

[141] D. D. Hickstein et al. "PyAbel (v0.7): A Python Package for Abel Transforms" (2016). DOI: 10.5281/zenodo.47423 (Cited on page 66).

[142] T.-l. Ho. "Universal Thermodynamics of Degenerate Quantum Gases in the Unitarity Limit". *Phys. Rev. Lett.* 92.9 (2004). DOI: 10.1103/PhysRevLett.92.090402 (Cited on page 73).

[143] G. R. Dennis, J. J. Hope, and M. T. Johnsson. "XMDS2: Fast, scalable simulation of coupled stochastic partial differential equations". *Comput. Phys. Commun.* 184.1 (2013). DOI: 10.1016/j.cpc.2012.08.016 (Cited on page 79).